**ISSN** 1949-8470 (online)

# World Journal of *Radiology*

*World J Radiol* 2011 January 28; 3(1): 1-40

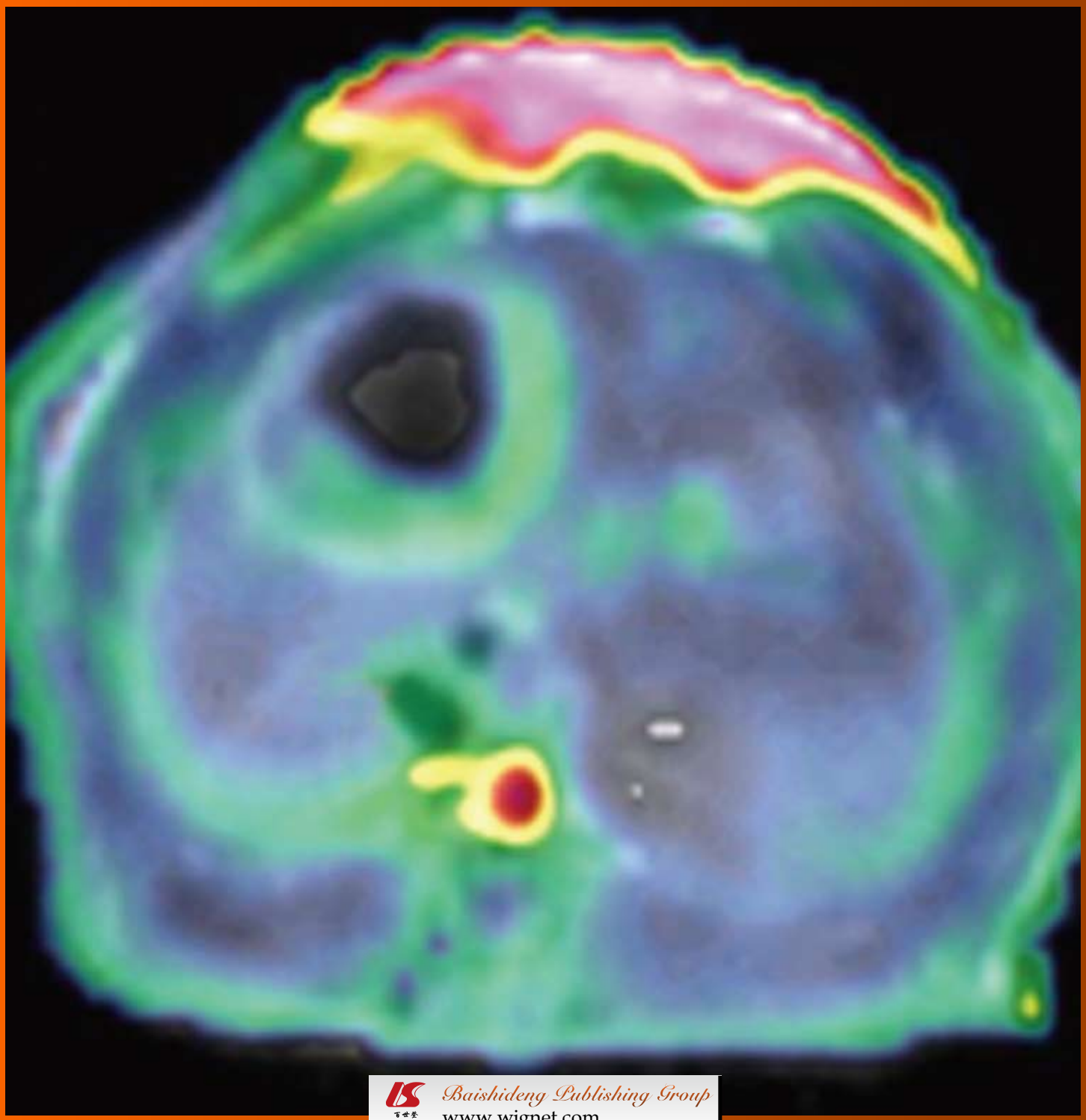

Baishideng Publishing Group
www.wjgnet.com

WJR World Journal of Radiology

A peer-reviewed, online, open-access journal of Radiology

# Editorial Board

2009-2013

The *World Journal of Radiology* Editorial Board consists of 319 members, representing a team of worldwide experts in radiology. They are from 40 countries, including Australia (3), Austria (4), Belgium (5), Brazil (3), Canada (9), Chile (1), China (25), Czech (1), Denmark (1), Egypt (4), Estonia (1), Finland (1), France (6), Germany (17), Greece (8), Hungary (1), India (9), Iran (5), Ireland (1), Israel (4), Italy (28), Japan (14), Lebanon (1), Libya (1), Malaysia (2), Mexico (1), Netherlands (4), New Zealand (1), Norway (1), Saudi Arabia (3), Serbia (1), Singapore (2), Slovakia (1), South Korea (16), Spain (8), Switzerland (5), Thailand (1), Turkey (20), United Kingdom (16), and United States (82).

**PRESIDENT AND EDITOR-IN-CHIEF**
Lian-Sheng Ma, *Beijing*

**STRATEGY ASSOCIATE EDITORS-IN-CHIEF**
Ritesh Agarwal, *Chandigarh*
Kenneth Coenegrachts, *Bruges*
Mannudeep K Kalra, *Boston*
Meng Law, *Lost Angeles*
Ewald Moser, *Vienna*
Aytekin Oto, *Chicago*
AAK Abdel Razek, *Mansoura*
Àlex Rovira, *Barcelona*
Yi-Xiang Wang, *Hong Kong*
Hui-Xiong Xu, *Guangzhou*

**GUEST EDITORIAL BOARD MEMBERS**
Wing P Chan, *Taipei*
Wen-Chen Huang, *Taipei*
Shi-Long Lian, *Kaohsiung*
Chao-Bao Luo, *Taipei*
Shu-Hang Ng, *Taoyuan*
Pao-Sheng Yen, *Haulien*

**MEMBERS OF THE EDITORIAL BOARD**

**Australia**
Karol Miller, *Perth*
Tomas Kron, *Melbourne*
Zhonghua Sun, *Perth*

**Austria**
Herwig R Cerwenka, *Graz*
Daniela Prayer, *Vienna*
Siegfried Trattnig, *Vienna*

**Belgium**
Piet R Dirix, *Leuven*
Yicheng Ni, *Leuven*
Piet Vanhoenacker, *Aalst*
Jean-Louis Vincent, *Brussels*

**Brazil**
Emerson L Gasparetto, *Rio de Janeiro*
Edson Marchiori, *Petrópolis*
Wellington P Martins, *São Paulo*

**Canada**
Sriharsha Athreya, *Hamilton*
Mark Otto Baerlocher, *Toronto*
Martin Charron, *Toronto*
James Chow, *Toronto*
John Martin Kirby, *Hamilton*
Piyush Kumar, *Edmonton*
Catherine Limperpoulos, *Quebec*
Ernest K Osei, *Kitchener*
Weiguang Yao, *Sudbury*

**Chile**
Masami Yamamoto, *Santiago*

**China**
Feng Chen, *Nanjing*
Ying-Sheng Cheng, *Shanghai*
Woei-Chyn Chu, *Taipei*
Guo-Guang Fan, *Shenyang*
Shen Fu, *Shanghai*
Gang Jin, *Beijing*
Tak Yeung Leung, *Hong Kong*
Wen-Bin Li, *Shanghai*
Rico Liu, *Hong Kong*
Yi-Yao Liu, *Chengdu*
Wei Lu, *Guangdong*
Fu-Hua Peng, *Guangzhou*
Li-Jun Wu, *Hefei*
Zhi-Gang Yang, *Chengdu*
Xiao-Ming Zhang, *Nanchong*
Chun-Jiu Zhong, *Shanghai*

**Czech**
Vlastimil Válek, *Brno*

**Denmark**
Poul Erik Andersen, *Odense*

**Egypt**
Mohamed Abou El-Ghar, *Mansoura*
Mohamed Ragab Nouh, *Alexandria*
Ahmed A Shokeir, *Mansoura*

**Estonia**
Tiina Talvik, *Tartu*

**Finland**
Tove J Grönroos, *Turku*

**France**

Alain Chapel, *Fontenay-Aux-Roses*
Nathalie Lassau, *Villejuif*
Youlia M Kirova, *Paris*
Géraldine Le Duc, *Grenoble Cedex*
Laurent Pierot, *Reims*
Frank Pilleul, *Lyon*
Pascal Pommier, *Lyon*

**Germany**

Ambros J Beer, *München*
Thomas Deserno, *Aachen*
Frederik L Giesel, *Heidelberg*
Ulf Jensen, *Kiel*
Markus Sebastian Juchems, *Ulm*
Kai U Juergens, *Bremen*
Melanie Kettering, *Jena*
Jennifer Linn, *Munich*
Christian Lohrmann, *Freiburg*
David Maintz, *Münster*
Henrik J Michaely, *Mannheim*
Oliver Micke, *Bielefeld*
Thoralf Niendorf, *Berlin-Buch*
Silvia Obenauer, *Duesseldorf*
Steffen Rickes, *Halberstadt*
Lars V Baron von Engelhardt, *Bochum*
Goetz H Welsch, *Erlangen*

**Greece**

Panagiotis Antoniou, *Alexandroupolis*
George C Kagadis, *Rion*
Dimitris Karacostas, *Thessaloniki*
George Panayiotakis, *Patras*
Alexander D Rapidis, *Athens*
C Triantopoulou, *Athens*
Ioannis Tsalafoutas, *Athens*
Virginia Tsapaki, *Anixi*
Ioannis Valais, *Athens*

**Hungary**

Peter Laszlo Lakatos, *Budapest*

**India**

Anil Kumar Anand, *New Delhi*
Surendra Babu, *Tamilnadu*
Sandip Basu, *Bombay*
Kundan Singh Chufal, *New Delhi*
Shivanand Gamanagatti, *New Delhi*
Vimoj J Nair, *Haryana*
R Prabhakar, *New Delhi*
Sanjeeb Kumar Sahoo, *Orissa*

**Iran**

Vahid Reza Dabbagh Kakhki, *Mashhad*
Mehran Karimi, *Shiraz*
Farideh Nejat, *Tehran*
Alireza Shirazi, *Tehran*
Hadi Rokni Yazdi, *Tehran*

**Ireland**

Joseph Simon Butler, *Dublin*

**Israel**

Amit Gefen, *Tel Aviv*
Eyal Sheiner, *Be'er-Sheva*
Jacob Sosna, *Jerusalem*
Simcha Yagel, *Jerusalem*

**Italy**

Mohssen Ansarin, *Milan*
Stefano Arcangeli, *Rome*
Tommaso Bartalena, *Imola*
Filippo Cademartiri, *Parma*
Sergio Casciaro, *Lecce*
Laura Crocetti, *Pisa*
Alberto Cuocolo, *Napoli*
Mirko D'Onofrio, *Verona*
Massimo Filippi, *Milan*
Claudio Fiorino, *Milano*
Alessandro Franchello, *Turin*
Roberto Grassi, *Naples*
Stefano Guerriero, *Cagliari*
Francesco Lassandro, *Napoli*
Nicola Limbucci, *L'Aquila*
Raffaele Lodi, *Bologna*
Francesca Maccioni, *Rome*
Laura Martincich, *Candiolo*
Mario Mascalchi, *Florence*
Roberto Miraglia, *Palermo*
Eugenio Picano, *Pisa*
Antonio Pinto, *Naples*
Stefania Romano, *Naples*
Luca Saba, *Cagliari*
Sergio Sartori, *Ferrara*
Mariano Scaglione, *Castel Volturno*
Lidia Strigari, *Rome*
Vincenzo Valentini, *Rome*

**Japan**

Shigeru Ehara, *Morioka*
Nobuyuki Hamada, *Chiba*
Takao Hiraki, *Okayama*
Akio Hiwatashi, *Fukuoka*
Masahiro Jinzaki, *Tokyo*
Hiroshi Matsuda, *Saitama*
Yasunori Minami, *Osaka*
Jun-Ichi Nishizawa, *Tokyo*
Tetsu Niwa, *Yokohama*
Kazushi Numata, *Kanagawa*
Kazuhiko Ogawa, *Okinawa*
Hitoshi Shibuya, *Tokyo*
Akira Uchino, *Saitama*
Haiquan Yang, *Kanagawa*

**Lebanon**

Aghiad Al-Kutoubi, *Beirut*

**Libya**

Anuj Mishra, *Tripoli*

**Malaysia**

R Logeswaran, *Cyberjaya*
Kwan-Hoong Ng, *Kuala Lumpur*

**Mexico**

Heriberto Medina-Franco, *Mexico City*

**Netherlands**

Jurgen J Fütterer, *Nijmegen*
Raffaella Rossin, *Eindhoven*
Paul E Sijens, *Groningen*
Willem Jan van Rooij, *Tilburg*

**New Zealand**

W Howell Round, *Hamilton*

**Norway**

Arne Sigmund Borthne, *Lørenskog*

**Saudi Arabia**

Mohammed Al-Omran, *Riyadh*
Ragab Hani Donkol, *Abha*
Volker Rudat, *Al Khobar*

**Serbia**

Djordjije Saranovic, *Belgrade*

**Singapore**

Uei Pua, *Singapore*
Lim CC Tchoyoson, *Singapore*

**Slovakia**

František Dubecký, *Bratislava*

**South Korea**

Bo-Young Choe, *Seoul*
Joon Koo Han, *Seoul*
Seung Jae Huh, *Seoul*
Chan Kyo Kim, *Seoul*
Myeong-Jin Kim, *Seoul*
Seung Hyup Kim, *Seoul*
Kyoung Ho Lee, *Gyeonggi-do*
Won-Jin Moon, *Seoul*
Wazir Muhammad, *Daegu*
Jai Soung Park, *Bucheon*
Noh Hyuck Park, *Kyunggi*
Sang-Hyun Park, *Daejeon*
Joon Beom Seo, *Seoul*
Ji-Hoon Shin, *Seoul*
Jin-Suck Suh, *Seoul*
Hong-Gyun Wu, *Seoul*

**Spain**

Eduardo J Aguilar, *Valencia*
Miguel Alcaraz, *Murcia*
Juan Luis Alcazar, *Pamplona*
Gorka Bastarrika, *Pamplona*
Rafael Martínez-Monge, *Pamplona*
Alberto Muñoz, *Madrid*
Joan C Vilanova, *Girona*

**Switzerland**

Nicolau Beckmann, *Basel*
Silke Grabherr, *Lausanne*
Karl-Olof Lövblad, *Geneva*
Tilo Niemann, *Basel*
Martin A Walter, *Basel*

**Thailand**

Sudsriluk Sampatchalit, *Bangkok*

**Turkey**

Olus Api, *Istanbul*
Kubilay Aydin, *İstanbul*
Işıl Bilgen, *Izmir*
Zulkif Bozgeyik, *Elazig*
Barbaros E Çil, *Ankara*
Gulgun Engin, *Istanbul*
M Fatih Evcimik, *Malatya*
Ahmet Kaan Gündüz, *Ankara*
Tayfun Hakan, *Istanbul*
Adnan Kabaalioglu, *Antalya*
Fehmi Kaçmaz, *Ankara*
Musturay Karcaaltincaba, *Ankara*
Osman Kizilkilic, *Istanbul*
Zafer Koc, *Adana*
Cem Onal, *Adana*
Yahya Paksoy, *Konya*
Bunyamin Sahin, *Samsun*
Ercument Unlu, *Edirne*
Ahmet Tuncay Turgut, *Ankara*
Ender Uysal, *Istanbul*

**United Kingdom**

K Faulkner, *Wallsend*
Peter Gaines, *Sheffield*
Balaji Ganeshan, *Brighton*
Nagy Habib, *London*
Alan Jackson, *Manchester*
Pradesh Kumar, *Portsmouth*
Tarik F Massoud, *Cambridge*
Igor Meglinski, *Bedfordshire*
Robert Morgan, *London*
Ian Negus, *Bristol*
Georgios A Plataniotis, *Aberdeen*
N J Raine-Fenning, *Nottingham*
Manuchehr Soleimani, *Bath*
MY Tseng, *Nottingham*
Edwin JR van Beek, *Edinburgh*
Feng Wu, *Oxford*

**United States**

Athanassios Argiris, *Pittsburgh*
Stephen R Baker, *Newark*
Lia Bartella, *New York*
Charles Bellows, *New Orleans*
Walter L Biffl, *Denver*
Homer S Black, *Houston*
Wessam Bou-Assaly, *Ann Arbor*
Owen Carmichael, *Davis*
Shelton D Caruthers, *St Louis*
Yuhchyau Chen, *Rochester*
Melvin E Clouse, *Boston*
Ezra Eddy Wyssam Cohen, *Chicago*
Aaron Cohen-Gadol, *Indianapolis*
Patrick M Colletti, *Los Angeles*
Kassa Darge, *Philadelphia*
Abhijit P Datir, *Miami*
Delia C DeBuc, *Miami*
Russell L Deter, *Houston*
Adam P Dicker, *Phil*
Khaled M Elsayes, *Ann Arbor*
Steven Feigenberg, *Baltimore*
Christopher G Filippi, *Burlington*
Victor Frenkel, *Bethesda*
Thomas J George Jr, *Gainesville*
Patrick K Ha, *Baltimore*
Robert I Haddad, *Boston*
Walter A Hall, *Syracuse*
Mary S Hammes, *Chicago*
John Hart Jr, *Dallas*
Randall T Higashida, *San Francisco*
Juebin Huang, *Jackson*
Andrei Iagaru, *Stanford*
Craig Johnson, *Milwaukee*
Ella F Jones, *San Francisco*
Csaba Juhasz, *Detroit*
Riyad Karmy-Jones, *Vancouver*
Daniel J Kelley, *Madison*
Amir Khan, *Longview*
Euishin Edmund Kim, *Houston*
Vikas Kundra, *Houston*
Kennith F Layton, *Dallas*
Rui Liao, *Princeton*
CM Charlie Ma, *Philadelphia*
Nina A Mayr, *Columbus*
Thomas J Meade, *Evanston*
Steven R Messé, *Philadelphia*
Nathan Olivier Mewton, *Baltimore*
Feroze B Mohamed, *Philadelphia*
Koenraad J Mortele, *Boston*
Mohan Natarajan, *San Antonio*
John L Nosher, *New Brunswick*
Chong-Xian Pan, *Sacramento*
Dipanjan Pan, *St Louis*
Martin R Prince, *New York*
Reza Rahbar, *Boston*
Carlos S Restrepo, *San Antonio*
Veronica Rooks, *Honolulu*
Maythem Saeed, *San Francisco*
Edgar A Samaniego, *Palo Alto*
Kohkan Shamsi, *Doylestown*
Jason P Sheehan, *Charlottesville*
William P Sheehan, *Willmar*
Charles Jeffrey Smith, *Columbia*
Monvadi B Srichai-Parsia, *New York*
Dan Stoianovici, *Baltimore*
Janio Szklaruk, *Houston*
Dian Wang, *Milwaukee*
Jian Z Wang, *Columbus*
Liang Wang, *New York*
Shougang Wang, *Santa Clara*
Wenbao Wang, *New York*
Aaron H Wolfson, *Miami*
Gayle E Woloschak, *Chicago*
Ying Xiao, *Philadelphia*
Juan Xu, *Pittsburgh*
Benjamin M Yeh, *San Francisco*
Terry T Yoshizumi, *Durham*
Jinxing Yu, *Richmond*
Jianhui Zhong, *Rochester*

WJR

World Journal of Radiology

Contents

Monthly Volume 3 Number 1 January 28, 2011

*World Journal of Radiology*
Volume 3 Number 1 January 28, 2011

## Contents



**EDITORS FOR THIS ISSUE**

**Responsible Assistant Editor:** *Na Liu*
**Responsible Electronic Editor:** *Xiao-Mei Zheng*
**Proofing Editor-in-Chief:** *Lian-Sheng Ma*
**Responsible Science Editor:** *Jian-Xia Cheng*

NAME OF JOURNAL
*World Journal of Radiology*

LAUNCH DATE
December 31, 2009

SPONSOR
Beijing Baishideng BioMed Scientific Co., Ltd.,
Room 903, Building D, Ocean International Center,
No. 62 Dongsihuan Zhonglu, Chaoyang District,
Beijing 100025, China
Telephone: 0086-10-8538-1892
Fax: 0086-10-8538-1893
E-mail: baishideng@wjgnet.com
http://www.wjgnet.com

EDITING
Editorial Board of *World Journal of Radiology*,
Room 903, Building D, Ocean International Center,
No. 62 Dongsihuan Zhonglu, Chaoyang District,
Beijing 100025, China
Telephone: 0086-10-8538-1892
Fax: 0086-10-8538-1893
E-mail: wjr@wjgnet.com
http://www.wjgnet.com

PUBLISHING
Baishideng Publishing Group Co., Limited,
Room 1701, 17/F, Henan Building,
No.90 Jaffe Road, Wanchai, Hong Kong, China
Fax: 00852-3115-8812
Telephone: 00852-5804-2046
E-mail: baishideng@wjgnet.com
http://www.wjgnet.com

SUBSCRIPTION
Beijing Baishideng BioMed Scientific Co., Ltd.,
Room 903, Building D, Ocean International Center,
No. 62 Dongsihuan Zhonglu, Chaoyang District,
Beijing 100025, China
Telephone: 0086-10-8538-1892
Fax: 0086-10-8538-1893
E-mail: baishideng@wjgnet.com
http://www.wjgnet.com

ONLINE SUBSCRIPTION
One-Year Price 216.00 USD

PUBLICATION DATE
January 28, 2011

CSSN
ISSN 1949-8470 (online)

PRESIDENT AND EDITOR-IN-CHIEF
Lian-Sheng Ma, *Beijing*

STRATEGY ASSOCIATE EDITORS-IN-CHIEF
Ritesh Agarwal, *Chandigarh*
Kenneth Coenegrachts, *Bruges*
Adnan Kabaalioglu, *Antalya*
Meng Law, *Lost Angeles*
Ewald Moser, *Vienna*
Aytekin Oto, *Chicago*
AAK Abdel Razek, *Mansoura*
Àlex Rovira, *Barcelona*
Yi-Xiang Wang, *Hong Kong*
Hui-Xiong Xu, *Guangzhou*

EDITORIAL OFFICE
Na Ma, Director
*World Journal of Radiology*
Room 903, Building D, Ocean International Center,
No. 62 Dongsihuan Zhonglu, Chaoyang District,
Beijing 100025, China
Telephone: 0086-10-8538-1892
Fax: 0086-10-8538-1893
E-mail: wjr@wjgnet.com
http://www.wjgnet.com

COPYRIGHT
© 2011 Baishideng. All rights reserved; no part of this publication may be reproduced, stored in a retrieval system, or transmitted in any form or by any means, electronic, mechanical, photocopying, recording, or otherwise without the prior permission of Baishideng. Authors are required to grant *World Journal of Radiology* an exclusive license to publish.

SPECIAL STATEMENT
All articles published in this journal represent the viewpoints of the authors except where indicated otherwise.

INSTRUCTIONS TO AUTHORS
Full instructions are available online at http://www.wjgnet.com/1949-8470/g_info_20100316162358.htm. If you do not have web access please contact the editorial office.

ONLINE SUBMISSION
http://www.wjgnet.com/1949-8470office

World Journal of Radiology

Online Submissions: http://www.wjgnet.com/1949-8470office
wjr@wjgnet.com
doi:10.4329/wjr.v3.i1.1

*World J Radiol* 2011 January 28; 3(1): 1-16
ISSN 1949-8470 (online)
© 2011 Baishideng. All rights reserved.

EDITORIAL

# Multiparametric MRI biomarkers for measuring vascular disrupting effect on cancer

Huaijun Wang, Guy Marchal, Yicheng Ni

Huaijun Wang, Guy Marchal, Yicheng Ni, Department of Radiology, University Hospitals, University of Leuven, Herestraat 49, B-3000 Leuven, Belgium
Author contributions: All authors made a substantial contribution to the conception and design of the manuscript, drafting the article or revising it.
Supported by (partially) The grants awarded by Fonds voor Wetenschappelijk Onderzoek-Vlaanderen (FWO Vlaanderen) Impulsfinanciering project (ZWAP/05/018); Geconcerteerde Onderzoeksactie of the Flemish Government, OT project (OT/06/70); the K.U. Leuven Molecular Small Animal Imaging Center MoSAIC (KUL EF/05/08); the center of excellence In vivo Molecular Imaging Research of K.U. Leuven; and a EU project Asia-Link CfP 2006-EuropeAid/123738/C/ACT/Multi-Proposal No. 128-498/111
Correspondence to: Dr. Yicheng Ni, Professor, Department of Radiology, University Hospitals, University of Leuven, Herestraat 49, B-3000 Leuven, Belgium. yicheng.ni@med.kuleuven.be
Telephone: +32-16-330165 Fax: +32-16-343765
Received: December 7, 2010 Revised: January 13, 2011
Accepted: January 20, 2011
Published online: January 28, 2011

## Abstract

Solid malignancies have to develop their own blood supply for their aggressive growth and metastasis; a process known as tumor angiogenesis. Angiogenesis is largely involved in tumor survival, progression and spread, which are known to be significantly attributed to treatment failures. Over the past decades, efforts have been made to understand the difference between normal and tumor vessels. It has been demonstrated that tumor vasculature is structurally immature with chaotic and leaky phenotypes, which provides opportunities for developing novel anticancer strategies. Targeting tumor vasculature is not only a unique therapeutic intervention to starve neoplastic cells, but also enhances the efficacy of conventional cancer treatments. Vascular disrupting agents (VDAs) have been developed to disrupt the already existing neovasculature in actively growing tumors, cause catastrophic vascular shutdown within short time, and induce secondary tumor necrosis. VDAs are cytostatic; they can only inhibit tumor growth, but not eradicate the tumor. This novel drug mechanism has urged us to develop multiparametric imaging biomarkers to monitor early hemodynamic alterations, cellular dysfunctions and metabolic impairments before tumor dimensional changes can be detected. In this article, we review the characteristics of tumor vessels, tubulin-destabilizing mechanisms of VDAs, and *in vivo* effects of the VDAs that have been mostly studied in preclinical studies and clinical trials. We also compare the different tumor models adopted in the preclinical studies on VDAs. Multiparametric imaging biomarkers, mainly diffusion-weighted imaging and dynamic contrast-enhanced imaging from magnetic resonance imaging, are evaluated for their potential as morphological and functional imaging biomarkers for monitoring therapeutic effects of VDAs.

© 2011 Baishideng. All rights reserved.

**Key words:** Vascular disrupting agents; Tumor vessels; Imaging biomarkers; Magnetic resonance imaging; Diffusion-weighted imaging; Dynamic contrast-enhanced magnetic resonance imaging

**Peer reviewer:** Rivka R Colen, MD, Department of Radiology, Brigham and Womens Hospital, 75 Francis St, Boston, MA 02115, United States

Wang H, Marchal G, Ni Y. Multiparametric MRI biomarkers for measuring vascular disrupting effect on cancer. *World J Radiol* 2011; 3(1): 1-16 Available from: URL: http://www.wjgnet.com/1949-8470/full/v3/i1/1.htm DOI: http://dx.doi.org/10.4329/wjr.v3.i1.1

## INTRODUCTION

For non-surgical anticancer strategies such as conventional radiotherapy and chemotherapy, the main disadvantage is lacking specificity for cancer tissue, i.e. concomitant

cytotoxic effects on normal tissues. In order to find more selective treatments, researchers have made efforts to exploit morphological, physiological and microenvironmental differences between normal and malignant tissues, including microvasculature, oxygenation and necrosis. One of the most prominent differences lies in the tumor neovasculature[1].

Tumor vasculature is a crucial component of pathophysiology in solid tumors, which affects growth, metastasis and therefore, response to therapy. Compared with the normal vasculature, tumor vessels are less mature in structure and leakier, where blood flow is spatially and temporally heterogeneous and often compromised. Furthermore, hyperpermeability of the vascular wall and lack of functional lymphatics within tumors elevate interstitial fluid pressure in solid tumors[2,3]. The molecular mechanisms of abnormal tumor vasculature may result from the imbalance between pro- and antiangiogenic regulating factors in tumor as well as host stromal cells[4]. Such vascular characteristics of solid tumors are sufficiently different from those of normal tissues and thus provide a unique target for tumor treatment[1].

Drugs developed for vascular targeting therapies can be divided into two different groups: antiangiogenic agents for inhibiting the formation of new vessels and vascular disrupting agents (VDAs) for destroying the existing vessels[5]. Hallmark characteristics with VDAs are selective reduction in tumor blood flow, induction of ischemic tumor necrosis, presence of viable neoplastic cells at the tumor periphery, and effect on delaying tumor growth[6]. According to their action mechanisms, VDAs can be further categorized into ligand-directed VDAs and small molecule VDAs. Small molecule VDAs include flavonoids such as 5,6-dimethylxanthenone-4-acetic acid (DMXAA/ASA404), and tubulin-destabilizing agents[7]. As a tubulin-destabilizing VDA, c*is*-1-(3,4,5,-trimethoxyphenyl)-2-(4'-methoxyphenyl)ethene-3'-0-phosphate or combretastatin A-4-phosphate (CA4P/Oxi2021) is most representative, and has been under phase Ⅲ clinical trials.

Unlike other conventional chemotherapies, VDAs are cytostatic rather than cytotoxic to malignant cells. They starve and indirectly kill tumor cells by depleting their blood supply, and can only delay tumor growth but not eradicate the tumor. Given this novel action mechanism, imaging biomarkers have been elaborated to detect and quantify non-invasively VDA-induced morphological, functional and metabolic alterations. Relative to the conventional clinical endpoints such as mortality and morbidity, these imaging biomarkers work in a more prompt, predictable and precise way[8,9]. Hereby, the term biomarker is adopted more broadly than its traditional definition, i.e. a biomarker can be derived not only from biofluid samples with the techniques of biochemistry and molecular biology, but also from modern imaging metrics including magnetic resonance imaging (MRI), computed tomography (CT), positron emission tomography (PET) or single photon emission tomography (SPECT), ultrasound, and optical imaging[10]. In this article, we review the action mechanisms of tubulin-destabilizing VDAs and the preclinical and clinical results of two lead VDAs, CA4P and ZD6126 (N-acetylcolchinol-O-phosphate), with the emphasis on the role of MRI in the preclinical evaluation of VDA effects.

## VDAs

### *Pathophysiological features of tumor vessels as targets of VDAs*

Oxygen diffusion distance from capillaries is only 150-200 μm. Because of the unrestrained growth, tumor cells growing outwith this effective diffusion distance become hypoxic and eventually necrotic[11-13]. Therefore, a tumor has to develop its own vessels to maintain its growth, i.e. angiogenesis, when its diameter exceeds about 0.5 mm[14].

These newly developed tumor vessels are often immature: the endothelial cells are irregular-shaped with larger interendothelial conjunctions[15,16] and poor connections between the endothelial lining and irregular basement membrane[17,18]. Due to these characteristics, tumor vessels are hyperpermeable and interstitial fluid pressure is higher than in normal tissues. Such high pressure is also contributed by the inefficient drainage with dysfunctional tumor lymphatics, which can be caused by rapid proliferation of tumor cells in a confined space, which creates mechanical stress that compresses intratumor lymphatics[19,20]. Besides, malignant tumors are known to feature with lymphatic deficiency or retarded development of lymphatics[19,20]. Tumor vessels are tortuous, disorganized and non-hierarchical, with complex branching of heterogeneous length and diameters, leading to high resistance to perfusion[21]. Under such conditions, any slight fluctuation of blood perfusion may cause catastrophic events in tumor vessels, while it has little effect on normal tissue, because mature vessels are more robust against perfusion changes due to efficient regulating mechanisms[21].

### *Role of cytoskeleton in the regulation of endothelial barrier function*

The endothelial barrier keeps the blood cells from exposure to surrounding tissues. Endothelial cells (ECs) line the inner surface of blood vessels and rely on their cytoskeleton to maintain the structural integrity of confluent monolayer and flat shape. Dysfunction in cellular shape can cause subsequent vascular hyperpermeability[22]. The cytoskeleton consists of three distinct components: microtubules, actin microfilaments and intermediate filaments[23], and the former two are associated *via* linking proteins, which, in turn, interact with these two cytoskeletal components for signaling[24]. As the scaffolding of the cell, the cytoskeleton plays a vital role in cell motility, division, shape maintenance, and signal transduction[24]. In tumor vessels, actin is ill-developed and thus the maintenance of cell shape depends more on microtubules[25,26].

The delicate dynamic balance between the centripetal tension and centrifugal force to ensure the cellular shape is finely modified by cytoskeleton and intercellular junc-

tional complexes of membrane-binding proteins that provide intercellular adherence, which is regulated by several signaling pathways[22]. Reorganization of actin leads to the assembly of bundled stress fibers, and therefore, increased cellular contractility. The main constituent of intercellular junctions is vascular endothelial (VE) cadherin/β-catenin complex anchored to actin[22]. Disruption of the VE-cadherin/β-catenin pathway causes the loss of intercellular junctional organization, dysfunction of monolayer barrier, and eventual rounding up of ECs[27].

### Mechanisms of VDA action

The mechanisms of action with VDAs still need to be fully elucidated. It has been speculated that CA4P binds to tubulin of microtubule at or close to the colchicine-binding site[28]. Unlike the antitumor effect with colchicine that is only achievable at a dose close to the maximum tolerated dose (MTD), the effect with VDAs is observed within a wide therapeutic window lower than the MTD. Their ability to selectively target the cytoskeleton and compromise the endothelial intercellular junctions is vital to their mechanisms of action[7]. CA4P has been most extensively studied. Therefore, we take CA4P as an example to discuss the potential molecular and cellular mechanisms of action, which are likely to be applicable to other tubulin-binding VDAs such as ZD6126.

On a long-term basis, CA4P inhibits the microtubule dynamics, interferes with the mitotic spindle function and leads to cell cycle arrest, which results in proliferation blockage and/or apoptosis[29]. Although such a direct cytotoxic or antiproliferative effect may contribute to the antivascular effects of CA4P, it would be too slow to account for the rapid vascular shutdown observed *in vivo*, which can occur within minutes after CA4P treatment in animal models[30]. Rather, immediate morphological and functional changes are more likely to be involved in such vascular collapse.

*In vitro*, it has been shown that Rho-GTPase plays an important role in the capillary-like collapse (Figure 1). Belonging to signaling G protein (GTPase), Rho proteins (Ras homologous proteins) are interconnected with microtubules[31]. The members of the Rho-GTPase family are essential in converting and amplifying external signals into cellular effects, including regulation of actin dynamics and cadherin/β-catenin pathway[32,33].

CA4P selectively binds to microtubules and depolymerizes tubulin, which results in the activation of Rho-GTPase and its associated Rho kinase[34-36] (Figure 1). Activation of the Rho/Rho-kinase pathway may cause downstream morphological and/or functional changes in ECs, which can lead to dysmorphism and hyperpermeability: (1) assembly of actin stress fibers and fortified contractility of ECs[24]; (2) disruption of the VE-cadherin/β-catenin complex to induce the loss of intercellular adhesion and the appearance of paracellular gaps[22]; (3) blebbing of ECs with regulation of stress-activated protein kinase p38 (SAPK-2/p38) to bring about increased monolayer permeability and resistance to blood flow[36,37]; and (4) vasoconstriction to give rise to increased geometric resistance to blood flow[38]. In addition, the direct binding of CA4P to tubulin compromises the integrity of cytoskeleton, and morphological changes of endothelial monolayer architecture further deteriorates[7,39] (Figure 1).

With the increased vascular permeability, the consequent leakage of plasma macromolecule into extravascular extracellular space (EES) results in fluid loss, increased hematocrit and formation of rouleaux[40]. As a result, the resistance to blood flow is increased. After EC damage, direct exposure of basement membrane to flowing blood initiates coagulation and hemorrhage[40]. Accordingly, the drop in blood flow induces hypoxia and deprivation of nutrients and subsequent necrosis of tumor (Figure 1).

*In vivo*, the increase in permeability may be the key event responsible for the VDA-induced vascular collapse[41]. Although the primary effects of CA4P have been confirmed *in vivo*, including morphological changes in ECs, such as blebbing[42] and increased permeability and vasoconstriction in arterioles[38], direct evidence of mechanisms *via* the activation of Rho/Rho-kinase pathway are still sparse. However, the CA4P-induced vascular shutdown effect is attenuated in combination with Rho or Rho kinase inhibitors[7,36,43], while amplified in combination with an anti-VE-cadherin agent[44], which may be considered indirect proof of the link between the cytoskeletal remodeling and permeability.

### Dose of VDAs

Some VDAs are orally active, e.g. ABT-751[39] and CYT 997[45], while intraperitoneal (ip) and intravenous (iv) administrations are most frequently applied in the treatment of tumors in rodent models. The ip injection is convenient for the handing of rodents, while it fails to mimic the clinical practice where iv injection is applied. Successful iv injection ensures an effective dose of VDA in the systemic circulation.

For single doses of CA4P, the MTD is estimated to be around 68 mg/m$^2$ in patients[46], which gives the clinically relevant dose of about 10 mg/kg in rats[47,48]. In mice, the roughly estimated MTD is 1000-1500 mg/kg[49]. However, the lowest effective dose is 25 mg/kg, which is already higher than the MTD in humans. Therefore, the CA4P effect with higher doses in mice is difficult to translate into humans[50].

For single doses of ZD6126, the MTD in patients is about 112 mg/m$^2$, which gives the clinically relevant dose of about 10 mg/kg in rats[51]. In mice, the MTD is about 750 mg/kg[52].

The tumor response to various VDAs depends mainly on drug type, tumor model and dosing regimen in preclinical studies. Generally speaking, the higher dose of VDAs can induce more striking antivascular effect, while the results cannot be convincingly translated into clinical practice if the dose for animal models exceeds the MTD in patients. Therefore, the results with clinically relevant doses in tumor models may better predict the outcomes in patients.

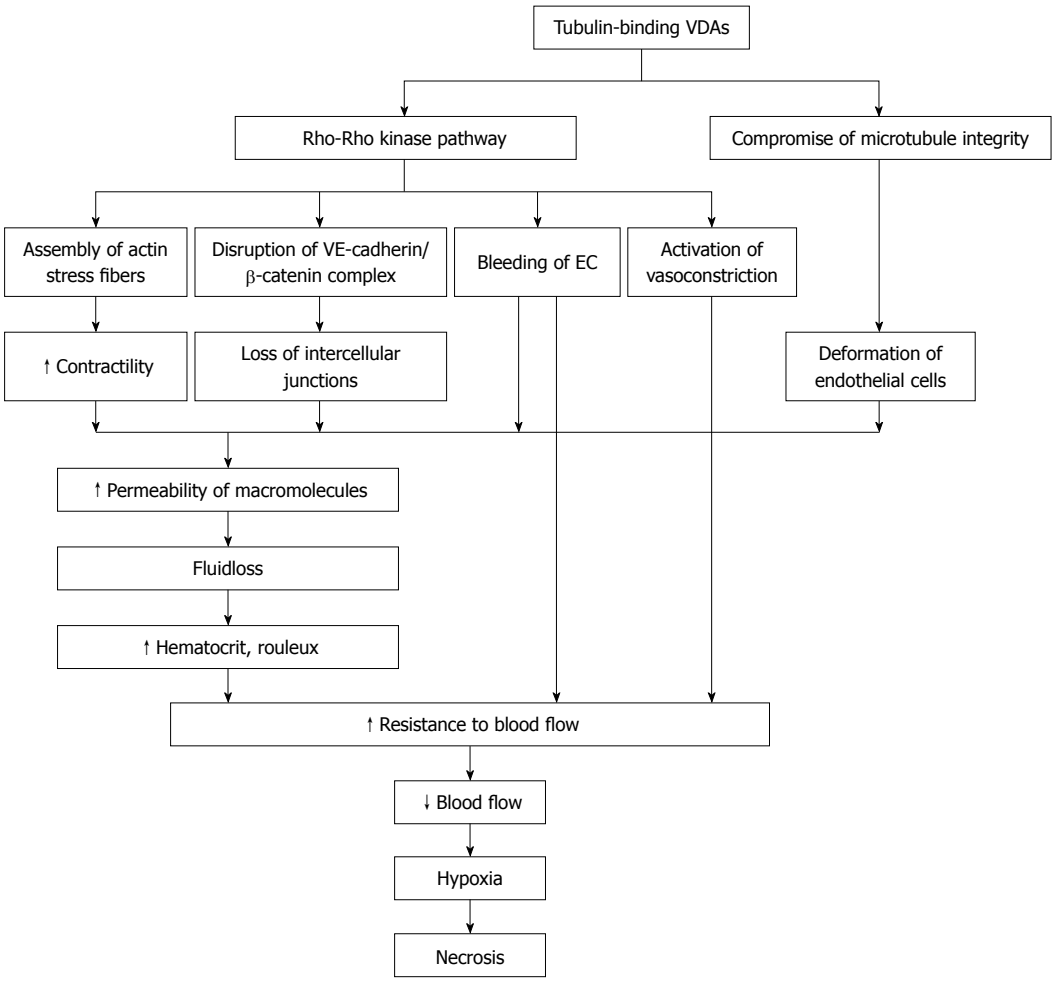


**Figure 1 Schematic mechanisms of action with tubulin-binding vascular disrupting agents.** VE: Vascular endothelial; VDAs: Vascular disrupting agents; EC: Endothelial cell.

### *In vivo effect*

After VDA treatment, a rapid increase in tumor vascular permeability triggers the catastrophic cascade of vessel collapse *in vivo*. A decrease in blood flow occurs almost immediately, and reaches the maximum in the following several hours. The collapsed blood supply induces central necrosis of the tumor. However, tumor sparing still exists at the periphery, leading to relapse after single-dose treatment[53-56]. The efficacy of such therapy relies largely on how fast blood supply is recovered. This restoration is unavoidable, because the tumor cells at the periphery can obtain a direct supply of oxygen and nutrients from neighboring normal tissues and engulfed normal vessels during the fast growth of malignancies[7,56]. Thus, growth of the tumor is only delayed due to the compromised blood supply and it cannot be eradicated.

Histopathologically, VDA-induced necrosis is located in the center of the tumor with a characteristic viable rim of a few cell layers adjacent to the normal tissue surrounding the tumor mass, which persists irrespective of differences in potency and efficacy of VDAs. In addition, hemorrhage often occurs together with necrotic tumor cells several hours after treatment[57]. Besides, the infiltration by inflammatory leukocytes may also contribute to the vascular-disrupting effect[41,42].

After VDA treatment, tumors may become phenotypically more aggressive due to hypoxia. With the regulation of hypoxia inducible factor 1α (HIF-1α), expression of angiogenic gene is activated and the level of vascular endothelial growth factor (VEGF) is thus increased[55,58]. Therefore, antiangiogenic therapy may be complementary to VDA, providing dual targeting at both preexisting and new vessels.

## ANIMAL TUMOR MODELS

*In vivo* cancer research in clinically relevant animal models bridges the *in vitro* studies of cell culture and biochemical assays with the more costly, time-consuming clinical practice. Considering the greater costs and stricter ethical regulations on human studies, a variety of rodent tumor models have been introduced particularly in combination with multiparametric imaging biomarkers to envisage the internal real-life events in experimental VDA research.

These animal models with various tumor cell lines can be classified according to several features. For examples, they can be categorized by locations such as subcutaneous[51,59], intramuscular[60-62] or visceral organ[57] tumors; by destination relative to source graft such as orthotopic[63-65] or ectopic tumors; by carcinogenesis such

as primary[26,48,65,66] or secondary tumors; by graft origins such as allograft[63] or xenograft human[61,67,68] or animal[69] tumors; and by immune status of tumor recipient such as the tumors growing in immunocompetent or immunodeficient[64,68] animals.

A wide range of diverse VDA effects have been observed in various tumor models[70,71]. Tumor microenvironment and host-tumor interaction may account for such discrepancy in responsiveness. Besides tumor cells with gene mutations, host stromal cells are also greatly involved in the tumor initiation, progression, invasion, and metastasis. For instance, with the expression of VEGF, stromal fibroblasts play a role in the formation and maintenance of tumor vessels[2]. Accordingly, when transplanted into various host locations or organs, the same neoplastic graft may have different angiogenesis and vascular functions. Thus, response to the same treatment may differ depending on tumor location and host-tumor interaction, because the organ-specific regulation of the balance between pro- and anti-angiogenic factors is responsible for the different angiogenesis activities[2,4,62,72]. As a result, tumor models of orthotopic transplantation into visceral organs of host animals with intact immune functions are thought to be more relevant to the conditions of clinical patients in terms of better mimicking tumor microenvironment, therefore, the treatment outcomes are more translatable into patients[62,72].

For imaging studies of VDA effects in small rodents, image quality has been shown to be satisfactory, even for organs susceptible to motion artifacts with non-respiratory-gated acquisition at a clinical magnet[56]. However, imaging in mice is more challenging than in rats, because the body weight of a mouse is about one-tenth of a rat, which results in lower signal-noise ratio (SNR) and poorer spatial resolution. In addition, success rate is sometimes compromised for the repetitive cannulations for intravenous injection of VDAs or contrast agents in mice during the dynamic follow-up of treatment monitoring, leading to some missing data.

## MEASURING TUMOR RESPONSE TO VDAs WITH *IN VIVO* IMAGING BIOMARKERS

VDAs have been shown to induce vascular shutdown in tumors within minutes, and how to evaluate accurately and promptly such effects remains a challenge to preclinical research and clinical practice. Ineffective treatment may not only hamper or delay the effective alternative therapies, but also cause unnecessary side effects and waste of resources. Considering the presence of possible non-responders to certain therapies, it is of immense importance to individualize the treatment regimens, in which early feedback after VDA treatment is deemed crucial.

For the assessment of anticancer effects, traditional clinical endpoints are difficult to quantify and may require lengthy and larger scales to complete[8,9]. Thus, it is impractical to perform such endpoints in the assessment of early effects with VDAs. Recently, multiparametric imaging biomarkers have been developed as "surrogate endpoints" to act as indispensable substitutes for such clinical endpoints. The quantitative structural, functional and metabolic information derived from these imaging biomarkers may enable more comprehensive assessments and predictions of clinical outcomes, and in this case, the possibility for timely therapeutic justification and adjustment in oncological patients under the VDA regimen.

Out of various imaging modalities, MRI has been most frequently applied for the evaluation of VDA effects due to its advantages such as excellent spatial and temporal resolution, imaging in arbitrary planes, no ionizing radiation and ability to provide morphological, functional and metabolic information (with MR spectroscopy) for serial post-treatment follow-up. In the following section, we focus on the role of MRI in the evaluation of VDAs and its validation with other robust and specific techniques.

### *Clinical and high-field-strength MRI scanners*

For preclinical research and clinical trials of VDAs, some animal studies have been performed with clinical 1.5 T MRI scanners[56,59,73], and more studies on small-bore research scanners[51,53,62,64,68,69,74,75]. The clinical and animal scanners are different in terms of availability in research centers, accessibility during working hours, usability, difficulty in method development, and translatability. Most important, with some parametrical optimization of built-in sequences, clinical scanners yield more translational results from small rodents to clinical patients than do dedicated animal scanners.

Recently, 3.0 T clinical scanners have become widely available with a trend for introducing even higher field whole body scanners (7-11 T) throughout the industry, since the safety approval of 3.0 T scanners in patients in 2002[76]. For intracranial tumors, 3.0 T scanners have shown better SNR, spatial and temporal resolution, contrast-to-noise ratio, and spectral resolution than 1.5 T scanners with the same acquisition parameters[76-79]. However, the applications in other regions of the body, the added value of 3.0 T compared with 1.5 T scanners is still controversial, due to issues such as specific absorption rate and motion and susceptibility artifacts. The modification of acquisition parameters and development of new coils may lead to wider applications in body imaging with 3.0 T MRI[80,81].

### *Biomarkers from conventional MRI sequences*

Conventional MRI biomarkers are derived from T2-weighted imaging (T2WI), T1-weighted imaging (T1WI) and contrast-enhanced T1WI (CE-T1WI). Despite the topographic information such as tumor location, shape and volume, the quantification of tumor signal intensity (SI) on T2WI can help to detect VDA-induced hemorrhage[64]. SI on T2WI can also help to differentiate the viable tissue from necrosis on a pixel-based image texture analysis[82]. The heterogeneous SI on T2WI after VDA

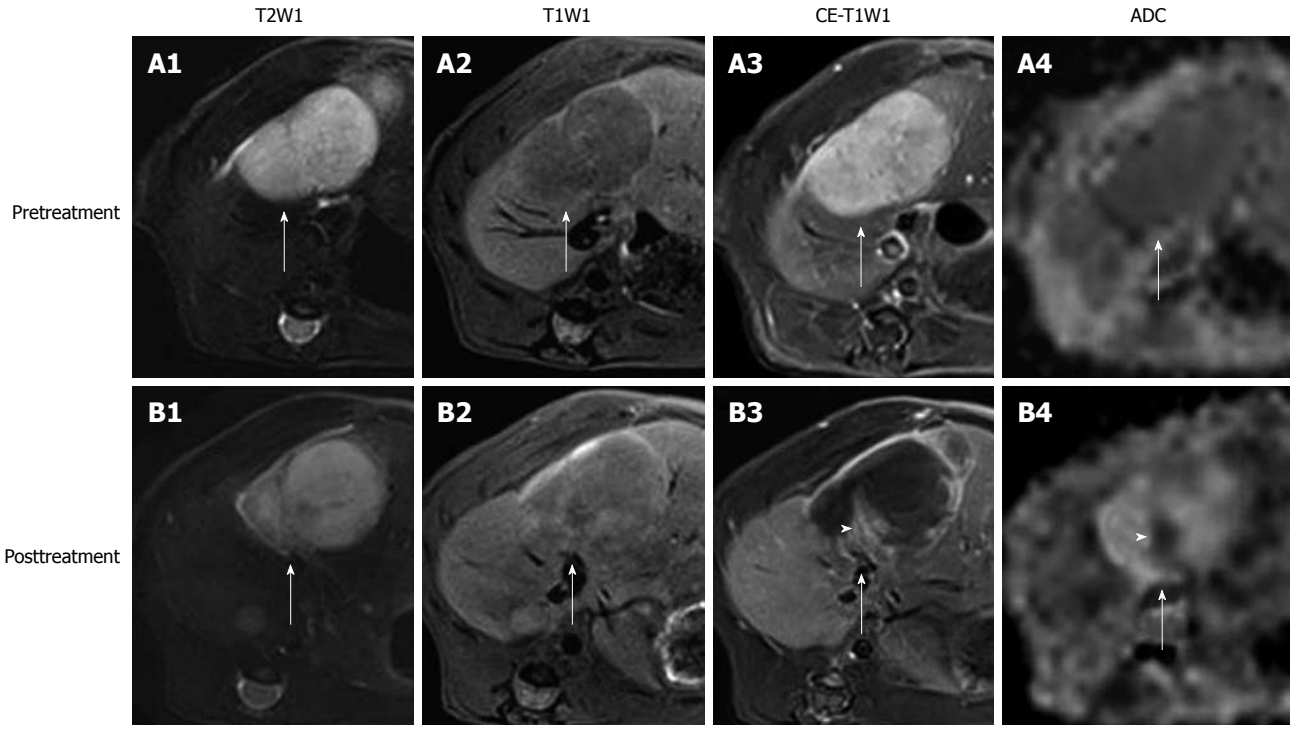


**Figure 2** ***In vivo*** **magnetic resonance imaging findings of an implanted tumor in rat liver.** Before treatment, the tumor (arrows) appeared hyperintense on T2WI (A1); hypointense on T1WI (A2); strongly enhanced on CE-T1WI (A3); and slightly hypointense on $ADC_{high}$ (b = 500, 750, 1000 s/mm$^2$) (A4). At 24 h after the intravenous treatment with CA4P at 10 mg/kg, obvious vascular shutdown was observed. The tumor (arrows) was still hyperintense on T2WI (B1) and hypointense on T1WI (B2). On CE-T1WI, the tumor (arrow) appeared hypointense in the center with an enhanced rim of viable neoplastic cells (B3). On $ADC_{high}$ map (B4), the hyperintensity in the center corresponded to necrosis, and the isointense ring was concordant with the viable tumor rim (arrow) on CE-T1WI. Note the viable tumor nodule at the periphery, shown as hyperintensity (arrowhead) on CE-T1WI (B3), and hypointensity (arrowhead) on $ADC_{high}$ (B4).

treatment is associated with (hemorrhagic) necrosis and complicated by evolving stages of necrosis and/or deoxyhemoglobin. Accordingly, SI change in T2WI is not considered a consistent imaging biomarker of hemorrhagic necrosis[51,71].

To date, the most frequently used surrogate endpoint for therapeutic evaluation of tumor response is the change in tumor size[83]. Tumor size can be measured linearly with 1D or 2D longest axis, although it may often lead to the overestimation of tumor volume of irregular shape. Manual delineation of tumor in tumor-containing slices or computer-assisted 3D analysis is more accurate for the estimation of tumor volume. Tumor volume of 3D analysis is predictive of survival in patients with tumors[84,85]. However, the change in tumor size/volume always falls as a late event behind the earlier and complex changes in microstructure and function induced by the downstream molecular and cellular events after VDA treatment[42,57], because VDAs only slow down the tumor growth without tumor eradication or size reduction[86]. Therefore, tumor size/volume is not a suitable imaging biomarker for very early assessment of the outcomes with VDAs (Figure 2).

Enhancement ratio is defined as the enhancement degree of tumor post-treatment on CE-T1WI relative to that before treatment[56]. It largely reflects the proportional distribution of contrast agent in blood vessels and EES of viable tumor tissues, and can be used for roughly assessing tumor vascularity, but it lacks the specific physiological meaning (Figure 2).

The necrosis ratio as an imaging biomarker for the evaluation of anticancer therapy has been endorsed as well as tumor size by the European Association for the Study of the Liver and the American Association for the Study of Liver Diseases[87,88]. The necrosis ratio can be measured on CE-T1WI, exploiting the perfusion deficit caused by the vascular shutdown in the non-viable tumor tissue (Figure 2). However, in this way, the necrosis ratio with non-specific contrast agent is underestimated due to inward diffusion of the contrast agent from the viable rim to the necrotic center of the tumor, when correlated with the necrosis ratio measured by histopathology[56,89]. Another method is to delineate the necrotic part on dynamic contrast-enhanced MRI (DCE-MRI) in order to minimize the diffusion of contrast agent[90]. Nevertheless, DCE-MRI has a relatively poor spatial resolution despite its high temporal resolution, i.e. the viable and necrotic tumor is sometimes difficult to discern on DCE-MRI. It needs to be explored which way to determine necrosis ratio can correlate better with the histopathological results. As an alternative to histopathology, the necrosis ratio from MRI may provide an imaging tool for assessing necrosis for the serial follow-up of patients after reliable necrosis develops. The ultimately reliable determination of necrosis may only be realized with the use of necrosis-avid contrast agents, which are not clinically available[91,92].

Conventional MRI biomarkers are easier to acquire and analyze, while they only reveal incomplete pathophysiological processes, and are often too late compared with

very rapid shutdown after VDA treatment. Thus, it is imperative to develop more prompt, accurate, quantifiable, and specific imaging biomarkers for characterizing those early molecular and cellular changes, which can be clinically applicable to depicting early functional and metabolic changes, offering the insight into VDA mechanisms of action, dictating the course of therapy, and predicting treatment outcomes. Fortunately, the recent rapid advances in MRI and other modalities have made such requirements feasible for developing functional imaging biomarkers.

### *Diffusion-weighted imaging*

First applied in neuroimaging, diffusion-weighted imaging (DWI) has rapidly evolved into a non-invasive oncological tool in the body, including the brain[93,94]. As a quantitative functional biomarker for detection and characterization of tumor, DWI is easy-to-perform and contrast-agent-free, and its innate imaging contrast is not significantly affected by exogenous contrast agents[95,96]. Therefore, DWI can be applied in patients with renal dysfunction, where contrast agents are contradicted, for repetitive monitoring after VDA treatment[97,98].

**Basic principles:** At a microscopic level, all water molecules undergo thermally driven random movement in three dimensions, so-called Brownian motion. Diffusion is a measure for the effective moving distance of water molecules within a given time[99,100]. In biological tissue, the mobility of water molecules are unavoidably hampered by their interaction with cell membranes, intracellular organelles and macromolecules, so that their apparent diffusion coefficient (ADC) within tissues in physiological or pathological conditions is determined by tissue cellularity, tissue components, and tortuosity of EES[101,102]. On the other hand, ADC is also affected by microscopic flow due to microcirculation within a voxel and water exchange between intracellular and extracellular compartments[8,103]. In general, ADC reflects the information of cellular density and membrane integrity, as well as different weighting of perfusion components, depending on the various diffusion gradients applied in the acquisition[103].

DWI can be obtained by applying two symmetrical diffusion-sensitizing gradients on the either side of a 180° refocusing pulse to a T2-weighted sequence. In a DWI sequence, moving water molecules undergo a phase shift after the first diffusion gradient and their phase shift cannot be canceled out as for static molecules after the second gradient, which causes the signal loss of moving water molecules on DWI. The imaging contrast between mobility-restricted and normal water molecules is thus created on SI[99]. For example, tumor tissues normally have higher cellular density, and after VDA treatment, edema with restricted mobility of water and necrosis with elevated diffusion in EES can be differentiated from normal tissues on DWI[86,104]. A diffusion gradient is characterized by the amplitude, duration and direction of diffusion-sensitizing factor (b value with the units s/mm$^2$), and the weighting of diffusion on SI depends on b value[99]. For quantification of ADC, gradients are applied in three directions (X, Y and Z axes). However, in tissues in which mobility of water molecules is restricted by some structural barriers such as fiber bundles in the brain, diffusion anisotropy is quantified in more than six directions on diffusion tensor imaging (DTI)[105].

**ADC-Quantification of DWI:** Frequently expressed in a unit of $10^{-3}$ mm$^2$/s, ADC is more robust against the influence of magnetic field strength and T2 shine-through effect, which facilitates intra- and inter-subject comparisons[106]. ADC can be quantified with the following least-squares algorithm[99]: $ADC = \ln(S_0/S_i)/b_i$ (1), where $S_i$ is the SI measured on the $i$th b value image and $b_i$ is the corresponding b value. $S_0$ is a variable that estimates the intrinsic SI (for b = 0 s/mm$^2$). In tumors, such quantification requires at least two values in one direction, while more than three values are used to reduce noise[107]. ADC value can be generated with mono-exponential fit between SI and b value for each voxel, and displayed as a parametric map for all voxels[94].

It is important to bear in mind that intravoxel incoherent motion (IVIM) may dominate ADC values in biological tissues when lower b values are used. This means that, for a given voxel, not only the diffusion of water molecules contributes to its ADC, but also the microcirculation of blood in capillary within the voxel[103]. In tumors, rapid blood flow leads to non-linearity of ADC fitting within lower range of b values, i.e. small increase in b value causes bigger attenuation of SI[108,109].

For the calculation of ADC, the usual method is to obtain an overall ADC fitting of mono-exponential decay through a range b values from 0 to about 1000 s/mm$^2$, or more specifically, flow-sensitive $ADC_{low}$ with lower b values (< 100-200 s/mm$^2$) and diffusion-sensitive $ADC_{high}$ with higher b values (> 500 s/mm$^2$) can be quantified. The difference between $ADC_{low}$ and $ADC_{high}$ can be defined as $ADC_{perfusion}$ to assess the perfusion fraction roughly[59,110] (Figure 3). Taking advantage of simplified calculation, mono-exponential analysis neglects the non-linearity of signal decay. To characterize the decay curve more adequately, bi- or multi-exponential models, as well as their alternative method, stretched model, are also explored in order to derive the perfusion fraction (f) and true diffusion coefficient (D). Despite the wider range of b values, longer acquisition time and requirement for higher SNR, the advantage of these more complicated models over mono-exponential methods still needs to be fully elucidated[8,108,111]. For any analytic method, the noise should be reduced whenever possible to ensure accurate fitting of ADC.

**Visual interpretation:** DW images can be evaluated on source DWI or quantitative ADC maps. DWI with b = 50 s/mm$^2$ is often called black blood imaging, due to its nullification of blood signals to render vessels black. Black blood DWI has a better detection rate for small tumor lesions than T2WI has[112], and has been recommended as

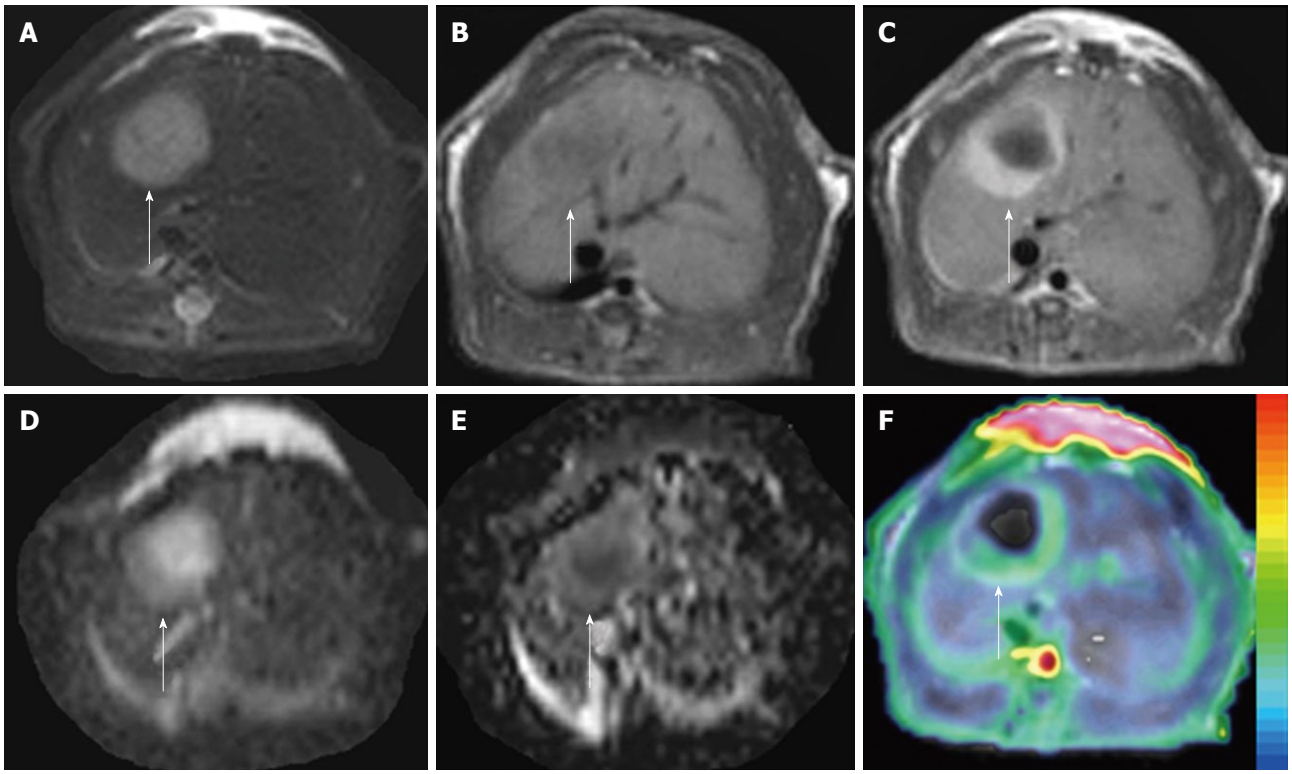


**Figure 3 $ADC_{perfusion}$ and initial area under the gadolinium curve in an implanted tumor in rat liver.** At 48 h after iv treatment with CA4P at 10 mg/kg, obvious tumor recurrence with partial recovery of blood supply was demonstrated. The tumor (arrows) appeared hyperintense on T2WI (A) and hypointense on T1WI (B); On CE-T1WI, the tumor relapsed at the periphery, shown as ring enhancement of viable tumor cells (C); $ADC_{10b}$ (derived from 10 b values from 0 to 1000 s/mm$^2$) revealed the hyperintense necrotic center and isointense viable tumor rim (D); On $ADC_{perfusion}$ ($ADC_{low}$-$ADC_{high}$) maps, the relative hyperintensity at the periphery suggested the partial recovery of perfusion, compared to the hypointensity in the necrotic center with perfusion deficit (E); $ADC_{perfusion}$ matched well with CE-T1WI-overlyaed initial area under the gadolinium curve (IAUGC) map (F).

an alternative to T2WI with conspicuity of small lesion on 3.0 T scanners[113]. The combination of DWI with T2WI and CE-T1WI has been suggested to improve the diagnostic accuracy of small tumor lesions[94]. However, due to T2 shine-through, hyperintensity on high b value (800-1000 s/mm$^2$) images does not always indicate increased cellularity, e.g. fluid shows hyperintense on both DWI and ADC maps. For this reason, ADC maps are preferable to DWI, and DWI should be always interpreted concurrently with the ADC map and all other available morphological images to prevent misinterpretation[104].

For the display of DWI or ADC maps, the inverted gray-scale (PET-like) for the suppression of background signal is used for whole-body DWI of high contrast from high b values, to detect multiple metastatic lesions[114]. With the co-registration between DWI or ADC maps with a color scale and structural T1WI or T2WI, fusion imaging can be obtained to integrate functional and anatomic information[8,94].

**Quantitative interpretation:** For the quantification of ADC, the most frequently used method is to draw a free-hand region of interest (ROI) or volume of interest (VOI) over the whole tumor, and mean or median values of all pixels/voxels within the ROI/VOI are obtained. Such manual delineation is easy but fails to characterize tumor heterogeneity. Histogram-based analysis can reflect the frequency of pixels with different diffusion, and the pixels can be divided into subgroups according to their ADC values. Therefore, it may better reflect how many pixels undergo change in ADC after treatment[8,115]. It has been demonstrated that ADC histogram analysis may be a superior and quicker biomarker of tumor response to bevacizumab than tumor volume[116]. With the spatially varying change in ADC after treatment, an ideal approach is to analyze the pixels present both before and after treatment with spatial tags to detect any change in ADC pixel by pixel. By using a threshold diffusion map, the pixels can be categorized into decrease, increase or no change after treatment. The segmented tumor can be overlaid on structural images to demonstrate clearly the heterogeneous response of a tumor to treatment depending on different locations within the tumor[117]. However, the pixel-wise registration is more susceptible to motion, and its applications in the body is more difficult than in the brain[8].

**Evolution of ADC changes:** In tumors, the mobility of water molecules is restricted due to cellular membranes or interaction with structural proteins. The high tumor cellularity results in lower diffusivity and thus lower measured ADC in most tumors. However, the restriction on diffusion is multifactorial and also influenced by the unique intracellular water diffusion and microscopic tissue/tumor organizational characteristics. Consequently, the ADC of

untreated tumors can occasionally be higher than that of native tissue[8,110], and it is vital to monitor intrasubject dynamic changes in ADC pre- and post-treatment.

Although the mechanism has not been fully explored, there is a temporary decrease in tumor ADC after VDA treatment. The probable reason may lie in abrupt decline in blood flow, subsequent cytotoxic edema due to the acute hypoxia, and resultant increased tortuosity of water molecules in EES[7,104]. Some preclinical studies have shown a transient decrease in ADC at 1 h after CA4P treatment[107,57]. The duration of decreased ADC was different in these two studies with the same tumor cell line but in different transplantation locations: ADC rebounded to pretreatment values in the intrahepatic tumor at 6 h[57]; however, ADC decreased gradually from 1 h until 6 h in the subcutaneous tumor[107]. The difference in doses of CA4P and tumor locations may have accounted for the phase discrepancy in ADC drop. On the other hand, the reduction in blood flow also contributed to the decrease in ADC[8,110], which was confirmed by the fact that $ADC_{low}$ decreased more significantly than $ADC_{high}$[56,107].

After the transient drop, ADC rebounds due to the collapsed cell membranes and decreased cellularity, and thus increased mobility of water molecules in EES throughout the progressing necrosis formation, during which the ADC value may reach the pretreatment baseline, and thus shows no significant difference from the baseline at some time points[74]; so-called pseudonormalization of ADC[118]. The onset and duration of pseudonormalization vary depending largely on tumor model and treatment strategy. If MRI falls within the window of pseudonormalization, there can be no significant change in ADC value, which, however, does not necessarily mean that ADC has not dynamically changed.

As necrosis develops, tumor cell volume is reduced with increased EES. The displacement of water molecules is less hampered, which increases ADC. The increase in ADC after VDA treatment has been shown in preclinical and clinical studies[53,57,68,119,120]. The peripheral sparing of tumor after VDA treatment has lower ADC, and can be distinguished from central necrosis of high ADC[8,110] (Figures 2 and 3). After single doses of VDA, the residual tumor unavoidably gives rise to recurrence, which in turn, leads to decreased overall ADC[59].

Derived from the different b values applied in DWI, $ADC_{high}$ mainly reflects the true diffusion and is more accurate for the characterization of VDA-induced necrosis; $ADC_{low}$, on the other hand, indicates the different weightings by several factors such as diffusion, microcirculation and structural barriers, which deteriorate its measurement reproducibility for individual or intergroup comparisons[119]; and $ADC_{perfusion}$ is most correlated with blood supply and can thus be used to approximate tumor blood perfusion as an alternative when venous access is limited[56,59] (Figure 3).

### *DCE-MRI*

DCE-MRI enables quantitative characterization of microcirculation in terms of blood flow, blood volume and/or capillary permeability, as well as pathophysiological insight into the mechanism of VDA action in tumors. Therefore DCE-MRI has been applied as a promising imaging biomarker for the assessment of VDA effects[121,122].

**Basic principles:** DCE-MRI involves serial acquisition of sequential images before, during and after injection of a contrast agent to cover the volume of the tumor. By tracking the pharmacokinetics of injected contrast agent, DCE-MRI is capable of the non-invasive quantification of microvascular structure and function. In VDA studies, two kinds of contrast agents are often used: low molecular weight agents (< 1000 Da, e.g. gadolinium diethylenetriaminepentaacetic acid or Gd-DTPA) that rapidly traverse from capillary into the EES, but not into tumor cells; and large molecular agents (> 20 kDa) with low capillary permeability for prolonged intravascular retention, so-called blood pool agents[123]. DCE-MRI sequences can be designed to be T1-weighted or T2*-weighted, which exploit different physiological properties to derive different kinetic variables. T1-weighted DCE-MRI is sensitive to the presence of contrast agent in the EES and reflects microvascular blood flow, permeability and extracellular leakage space, whereas T2*-weighted DCE-MRI, or more specifically, dynamic susceptibility contrast (DSC) MRI, is sensitive to the vascular phase of contrast agent delivery and reflects blood flow and volume[124].

Upon bolus injection, the contrast agent enters arterioles and passes through the capillary network, known as the first pass of the contrast agent. Its paramagnetic properties render a decrease in both the T1 and T2* (or T2) relaxation times of water molecules. On T2*-weighted DEC-MRI, the transient drop of SI of nearby tissue is due to the presence of contrast agent within the capillary compartment. Therefore, such a sequence performs better in brain with intact blood brain barrier (BBB) or when combined with blood pool contrast agents, since the tracer largely remains intravascular[125]. Measurement of the T2* effect during the rapid decrease and subsequent recovery in SI necessitates rapid sampling acquisition to ensure high temporal resolution. T2*-weighted DEC-MRI is mostly applied in brain tumors due to the presence of the BBB[124,126]. In extracranial tumors, the contrast agent readily extravasates from the intravascular space into the EES at a rate determined by several physiological factors including tissue blood flow, permeability of the capillaries and surface area. On T1-weighted DCE-MRI, contrast agent in EES shortens the $T_1$ relaxation time of nearby water hydrogen nuclei and causes increased SI. Therefore, T1-weighted DEC-MRI is widely applied in the extracranial tumors[127].

**Quantification of DCE-MRI:** For the quantification of DCE-MRI, we need to convert SI into the concentration of contrast agent at each time point during the acquisition. This is accomplished by measuring the T1 map on T1-weighted DCE-MRI, while it is more complicated in

T2*-weighted DCE-MRI. It is usually necessary to derive arterial input function (AIF) by measuring the SI in arteries near the locations of tumor, and AIF is useful for the compensation of the influence of injection speed of contrast agent and cardiac output[128].

**T2*-weighted DCE-MRI:** The quantification of T2*-weighted DCE-MRI can be semi-quantitative or quantitative. The former method does not employ complicated kinetic modeling or AIF, and derived summary parameters from contrast agent concentration time curve (or SI time curve) include area under the peak (AUP), and time to peak (TTP). Such analysis is straightforward, while it does not provide pathophysiological information of perfusion related to vascular shutdown[129], and may also be complicated with the leakage of contrast agent into the EES, which is likely in tumors with high permeability[130].

For quantitative analysis of T2*-weighted DCE-MRI, the most robust biomarker is relative blood volume (rBV) from the first-pass technique, calculated as the integral area under the concentration-time curve, with the interpretation of AIF and kinetic models[131]. Relative blood flow can also be quantified, and mean transit time (MTT) is obtained according to the central volume theorem BF = BV/MTT. However, extracranial tumors are usually hyperpermeable, and the compartmentalization of contrast agent is usually lost. Thus quantification of these parameters are less reliable due to the leakage of contrast agent into the EES and subsequent T1 effect on T2*-weighted sequence. The possible solutions include the correction with gamma-variate function by using more complicated kinetic models, preloaded dose of contrast agent to eliminate the effect of its leakage into the EES or its recirculation, and dual or multiecho imaging sequences[130,132-135].

**T1-weighted DCE-MRI:** T1-weighed DCE-MRI exploits the distribution of contrast agent in the EES, which increases the T1 relaxation rate (1/T1) of nearby hydrogen nuclei. The concentration of gadolinium ions is known to be directly proportional to the change in 1/T1, and the latter is related to changes in SI on T1WI. With a low gadolinium dose, we can assume that there is a linear relation between the amount of contrast agent in the tissue and the resultant difference in relaxation time[136]. Semi-quantitative and quantitative analyses of T1-weighted DCE-MRI are possible.

For semi-quantitative analysis, the model-free method utilizes the enhancement curve in terms of curve shape, time from injection to arrival of contrast agent, gradient of upslope or wash out phase and maximal intensity[124]. The most frequently used parameter is initial area under the gadolinium curve (IAUGC) (Figure 3), as well as maximal initial slope of curve, TTP, and the slope of washout[56,127]. The simplicity of this method with computer routine enables its easy accessibility to many investigators, and it has been shown to be successful to monitor the responses to VDA[59,137]. However, these semi-quantitative measures fail to show any direct correlation with underlying physiological measures of tumor perfusion, permeability or leakage space, and only provide a mixed complex that hampers the interpatient or interscanner comparison[122,138].

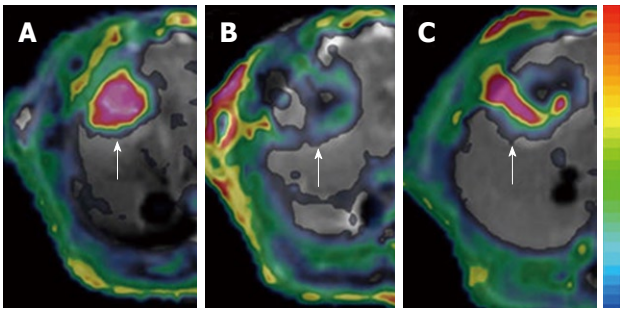


**Figure 4 Dynamic changes in $K^{trans}$.** The tumor (arrows) in rat liver showed an abundant blood supply with high $K^{trans}$ before treatment (A); At 6 h after CA4P treatment, vascular shutdown was indicated with low $K^{trans}$ in the center, surrounded by tumor residue at the periphery, with moderate $K^{trans}$ (B); At 48 h after treatment, the tumor relapsed upon the residue at the periphery with rebounding $K^{trans}$ (C).

Quantitative analysis of T1-weighed DCE-MRI involves a pharmacokinetic model to characterize the underlying physiological process of the contrast agent in tissues, including its administration, first pass, transendothelial process, distribution in EES, and wash out[124,139]. On the basis of some simplifying assumptions, biological tissues can be regarded as several compartments, e.g. two-compartment model with blood plasma and EES, within which contrast agent is instantaneously mixed and uniformly distributed[127]. The Tofts model is one of the frequently used pharmacokinetic models to fit concentration-time serial data in order to derive physiological parameters[140,141]. The robust parameters include $K^{trans}$ (volume transfer constant of the contrast agent, unit/min), $K_{ep}$ (rate constant of wash out of contrast agent refluxing from EES into blood, unit/min) and $V_e$ (the extravascular extracellular volume fraction, unit %).

Although quantification of $K^{trans}$ is often overestimated due to the innate assumptions in all kinetic models[142], and dedicated software has to be involved in the analysis, quantitative analysis of T1-weighted DCE-MRI highlights the underlying mechanism of VDA action in terms of the permeability change and subsequent perfusion collapse after VDAs, and it facilitates the direct comparison of these physiological parameters for intra- and inter-subject studies (Figure 4). Thus, the imaging biomarkers from DCE-MRI are most correlative to the VDA effects.

**Interpretation of DCE-MRI:** In general, successful VDA treatment causes the immediate vascular shutdown of tumors, shown as a rapid drop in semi-quantitative and quantitative DCE-MRI parameters within minutes or hours, and neoplastic recurrence is reflected as recovery in such measures to baseline level, which depends on the dose of VDAs and tumor models[7,26,39,53,54,73,143] (Figure 4).

$K^{trans}$ reflects a composite of both blood flow and vascular permeability-area product, and therefore, its interpretation depends on the rate-limiting step between

perfusion in vessels and diffusion into the EES. In untreated tumors, the vascular permeability-area product is often high, and the tissue is described as flow-limited, so that $K^{trans}$ approximates blood flow[140]; after the treatment with VDAs, the permeability transiently increases and then the blood flow drops abruptly, which decreases $K^{trans}$. However, in this mixed situation, the blood flow and permeability cannot be decoupled and it is difficult to identify the dominating factor between the perfusion and permeability-area product[56,124,140] (Figure 4).

For example, in a rat subcutaneous tumor model, tumor perfusion decreased by 57% with ABT-751 treatment after 1 h, but recovered to near pretreatment levels within 6 h[59]. In a rat liver tumor model with ZD6126 treatment, $K^{trans}$ dropped to its lowest at 24 h and partially recovered at 48 h[56], while for the same tumor cell line but in subcutaneous model with CA4P, $K^{trans}$ decreased to its lowest level at 6 h and recovered at 9 d[59]. Values of DCE-MRI parameters are derived from an ROI covering the whole tumor in most studies, which however, ignores the tumor heterogeneity due to the persistence of the viable rim after VDA treatment. Therefore, inclusion of non-enhancing pixels in the center artificially underestimates the mean and/or median parameter values[144]. Some authors have defined the tumor center and periphery and have analyzed the DCE-MRI parameters respectively, and have successfully shown the different responses in necrotic center and viable rim, which have helped to elucidate tumor pathophysiology and drug action of VDAs[46]. However, the definition of core and rim is debatable[145] and manual delineation of tumor center and periphery suffers from relatively poor spatial resolution on DCE-MRI, even with cross reference to other structural images of higher spatial resolution such as that derived from CE-T1WI.

Alternatively, pixel-based analysis of DCE-MRI quantifies the value of each pixel within a tumor, and distribution histogram and mean and/or median values can be derived, which is especially helpful in the dynamic follow-up of VDA treatment[146,147]. Nonetheless, this pixel-based method suffers more from motion artifacts in extracranial tumors, than whole-tumor-based analysis, and the technique remains challenging for physiological motion, such as cardiac and respiratory movements[148].

## VALIDATION OF MRI FINDINGS

The tumor response to VDA treatment has been widely validated using a number of methods. As an established index for determining VDA treatment efficacy, treatment-induced necrosis, as well as cytotoxic edema, has been confirmed with postmortem histopathology[57,107]. Necrosis has been an established end point of drug response with histopathological proofs in preclinical VDA studies, and the extent of necrosis is consistent with the DCE-MRI parameters. Considering uneasily accessible histopathology in patients, DCE-MRI is regarded as a promising biomarker to demonstrate the VDA-induced necrosis in patients[149].

Unfortunately, the validation of VDA-induced vascular collapse with resultant stoppage of tumor blood supply is still technically challenging due to a lack of more robust methods. One frequently adopted method is microvascular density (MVD) determination with immunohistochemical staining by using vascular markers such as CD31, CD34 or CD105[150]. Some studies with antiangiogenic treatment have shown a correlation between DCE-MRI parameters and immunohistochemical findings, whereas others have not[133]. There is a paucity of such correlation data in VDA studies. Gaya *et al*[151] have shown no strong relationship between changes in DCE-MRI kinetic variables following CA4P and the immunohistochemical angiogenic profile. There is always a discrepancy between histological MVD and functional vascular density: not all tumor vessels are perfused at a given time[124], and it is not surprising that MVD fails to characterize the functional properties including vessel permeability, which contribute to DCE-MRI parameters. On the other hand, blood vessels are often distended early after VDA treatment, with severe comprise of blood flow, which can be false-negative on MVD measurement[152]. Accordingly, its value as an indicator of the efficacy of VDA therapies is limited[153]. In other words, the absence of decreased MVD does not necessarily indicate ineffective VDA treatment[150]. Alternatively, Hoechst 33342 is a dye that stains the nuclei of ECs lining blood vessels that are perfused at the time of injection, and therefore, may provide a better histological measurement of functional vasculature *via* fluorescence microscopy after VDA treatment[149,153-155].

In a rat tumor model treated with CA4P, Maxwell *et al*[156] have compared $K^{trans}$ with tumor blood flow measured by the uptake of radiolabeled iodoantipyrine (IAP). They have shown that dynamic changes in $K^{trans}$ and AUC, and tumor blood flow from IAP uptake after treatment are highly correlated, although with the changes in $K^{trans}$ and AUC being smaller than those in blood flow by IAP. However, it is still uncertain to what extent $K^{trans}$ can mirror the blood flow changes, especially in the condition limited by permeability-surface area product, which may be the case in extracranial tumors after VDA treatment[156,157]. In VDA studies, the correlation still needs to be explored with other robust techniques such as H215O-PET[158] and microbubble ultrasound[159].

## FUTURE PERSPECTIVES

Multiparametric MRI biomarkers enable non-invasive characterization of tumor response to VDA, while the variety of biomarkers also leads to the challenges in terms of robust protocol for standardization of imaging acquisition and analysis on intrasubject or intersubject basis. Therefore, it is imperative to develop a standardized protocol to facilitate the comparative evaluation of VDA treatment effects in multicenter studies.

Due to practical limitations, advanced MRI methods of imaging acquisition and analysis for DWI and DCE-MRI are only accessible in research centers with expertise.

However, this should not be a hurdle to perform examinations. Therefore, to circumvent technical limitations, a hierarchical protocol with compromises can be expected, in which the protocols from the most ideal conditions to some practical alternatives are given, according to their relevance to the insight of pathophysiological mechanisms of VDA action[56].

Heterogeneity is involved throughout VDA treatment: tumors can be responders or non-responders to VDAs; the response degree can vary; and most importantly, tumor residue unavoidably remains at the periphery due to the incomplete tumoricidal effect of VDAs. The most adopted whole-tumor-based quantitative analysis neglects the spatial heterogeneity with central necrosis and peripheral sparing, which, however, may affect therapeutic evaluation and prognostic prediction for the adjustment of individual therapy strategy[144]. Other alternatives such as co-registration between pre- and post-treatment images facilitate the pixel-based demonstration of treatment response, although they are still problematic for application in areas with significant movement, such as the abdomen[117].

It is only by combining multiparametric imaging biomarkers that we may begin to understand how VDAs affect tissue environment and tumor cells. To date, DCE-MRI and DWI, as well as $^{18}$F fluorodeoxyglucose PET are the most advanced biomarkers, from which we can gain insights into vascular function, programmed cell death or necrosis, and glucose metabolism. However, procedural rigor of these multiparametric imaging biomarkers has to be established before they can take up an essential position in clinical decision making[56,160].

## CONCLUSION

Considering the requirements of prompt therapeutic justification and adjustment for oncological patients with VDA treatment, there are urgent demands for establishing comprehensive imaging protocol for "go or no-go" clinical decisions. Investigations in preclinical animal models can provide the insights into the mechanism of VDA action; realized by applying multiparametric imaging biomarkers with validation at microscopic levels. Therefore, it is possible that combination of these quantitative imaging biomarkers, especially DWI and DCE-MRI, can play an imperative role in clinical treatment regimens that involve VDAs. Standardization of imaging acquisition and analysis with advanced hardware and software needs to be developed to improve the accuracy and comparability of VDA studies in multicenter studies.

## REFERENCES


1 **Brown JM**, Giaccia AJ. The unique physiology of solid tumors: opportunities (and problems) for cancer therapy. *Cancer Res* 1998; **58**: 1408-1416
2 **Fukumura D**, Jain RK. Tumor microvasculature and microenvironment: targets for anti-angiogenesis and normalization. *Microvasc Res* 2007; **74**: 72-84
3 **Vaupel P**, Kallinowski F, Okunieff P. Blood flow, oxygen and nutrient supply, and metabolic microenvironment of human tumors: a review. *Cancer Res* 1989; **49**: 6449-6465
4 **Fidler IJ**. Angiogenic heterogeneity: regulation of neoplastic angiogenesis by the organ microenvironment. *J Natl Cancer Inst* 2001; **93**: 1040-1041
5 **Lippert JW 3rd**. Vascular disrupting agents. *Bioorg Med Chem* 2007; **15**: 605-615
6 **Heath VL**, Bicknell R. Anticancer strategies involving the vasculature. *Nat Rev Clin Oncol* 2009; **6**: 395-404
7 **Kanthou C**, Tozer GM. Microtubule depolymerizing vascular disrupting agents: novel therapeutic agents for oncology and other pathologies. *Int J Exp Pathol* 2009; **90**: 284-294
8 **Padhani AR**, Liu G, Koh DM, Chenevert TL, Thoeny HC, Takahara T, Dzik-Jurasz A, Ross BD, Van Cauteren M, Collins D, Hammoud DA, Rustin GJ, Taouli B, Choyke PL. Diffusion-weighted magnetic resonance imaging as a cancer biomarker: consensus and recommendations. *Neoplasia* 2009; **11**: 102-125
9 **Smith JJ**, Sorensen AG, Thrall JH. Biomarkers in imaging: realizing radiology's future. *Radiology* 2003; **227**: 633-638
10 **Murphy PS**, McCarthy TJ, Dzik-Jurasz AS. The role of clinical imaging in oncological drug development. *Br J Radiol* 2008; **81**: 685-692
11 **Jain RK**. Barriers to drug delivery in solid tumors. *Sci Am* 1994; **271**: 58-65
12 **Gimbrone MA Jr**, Cotran RS, Leapman SB, Folkman J. Tumor growth and neovascularization: an experimental model using the rabbit cornea. *J Natl Cancer Inst* 1974; **52**: 413-427
13 **Thomlinson RH**, Gray LH. The histological structure of some human lung cancers and the possible implications for radiotherapy. *Br J Cancer* 1955; **9**: 539-549
14 **Folkman J**. Role of angiogenesis in tumor growth and metastasis. *Semin Oncol* 2002; **29**: 15-18
15 **Dvorak HF**, Nagy JA, Dvorak JT, Dvorak AM. Identification and characterization of the blood vessels of solid tumors that are leaky to circulating macromolecules. *Am J Pathol* 1988; **133**: 95-109
16 **Hashizume H**, Baluk P, Morikawa S, McLean JW, Thurston G, Roberge S, Jain RK, McDonald DM. Openings between defective endothelial cells explain tumor vessel leakiness. *Am J Pathol* 2000; **156**: 1363-1380
17 **Paku S**, Paweletz N. First steps of tumor-related angiogenesis. *Lab Invest* 1991; **65**: 334-346
18 **Baluk P**, Morikawa S, Haskell A, Mancuso M, McDonald DM. Abnormalities of basement membrane on blood vessels and endothelial sprouts in tumors. *Am J Pathol* 2003; **163**: 1801-1815
19 **Leu AJ**, Berk DA, Lymboussaki A, Alitalo K, Jain RK. Absence of functional lymphatics within a murine sarcoma: a molecular and functional evaluation. *Cancer Res* 2000; **60**: 4324-4327
20 **Padera TP**, Stoll BR, Tooredman JB, Capen D, di Tomaso E, Jain RK. Pathology: cancer cells compress intratumour vessels. *Nature* 2004; **427**: 695
21 **Sevick EM**, Jain RK. Geometric resistance to blood flow in solid tumors perfused ex vivo: effects of tumor size and perfusion pressure. *Cancer Res* 1989; **49**: 3506-3512
22 **Bogatcheva NV**, Verin AD. Reprint of "The role of cytoskeleton in the regulation of vascular endothelial barrier function" [Microvascular Research 76 (2008) 202-207]. *Microvasc Res* 2009; **77**: 64-69
23 **Pasquier E**, Kavallaris M. Microtubules: a dynamic target in cancer therapy. *IUBMB Life* 2008; **60**: 165-170
24 **Lee TY**, Gotlieb AI. Microfilaments and microtubules maintain endothelial integrity. *Microsc Res Tech* 2003; **60**: 115-127
25 **Thorpe PE**. Vascular targeting agents as cancer therapeutics. *Clin Cancer Res* 2004; **10**: 415-427
26 **Siemann DW**, Chaplin DJ, Walicke PA. A review and update of the current status of the vasculature-disabling agent combretastatin-A4 phosphate (CA4P). *Expert Opin Investig Drugs*

2009; **18**: 189-197
27 **Schwartz EL**. Antivascular actions of microtubule-binding drugs. *Clin Cancer Res* 2009; **15**: 2594-2601
28 **Lee RM**, Gewirtz DA. Colchicine site inhibitors of microtubule integrity as vascular disrupting agents. *Drug Dev Res* 2008; **69**: 352-358
29 **Jordan MA**, Wilson L. Microtubules as a target for anticancer drugs. *Nat Rev Cancer* 2004; **4**: 253-265
30 **Anderson HL**, Yap JT, Miller MP, Robbins A, Jones T, Price PM. Assessment of pharmacodynamic vascular response in a phase I trial of combretastatin A4 phosphate. *J Clin Oncol* 2003; **21**: 2823-2830
31 **Wittmann T**, Waterman-Storer CM. Cell motility: can Rho GTPases and microtubules point the way? *J Cell Sci* 2001; **114**: 3795-3803
32 **Boureux A**, Vignal E, Faure S, Fort P. Evolution of the Rho family of ras-like GTPases in eukaryotes. *Mol Biol Evol* 2007; **24**: 203-216
33 **Bustelo XR**, Sauzeau V, Berenjeno IM. GTP-binding proteins of the Rho/Rac family: regulation, effectors and functions in vivo. *Bioessays* 2007; **29**: 356-370
34 **Waterman-Storer CM**, Salmon E. Positive feedback interactions between microtubule and actin dynamics during cell motility. *Curr Opin Cell Biol* 1999; **11**: 61-67
35 **Birukova AA**, Adyshev D, Gorshkov B, Bokoch GM, Birukov KG, Verin AD. GEF-H1 is involved in agonist-induced human pulmonary endothelial barrier dysfunction. *Am J Physiol Lung Cell Mol Physiol* 2006; **290**: L540-L548
36 **Kanthou C**, Tozer GM. The tumor vascular targeting agent combretastatin A-4-phosphate induces reorganization of the actin cytoskeleton and early membrane blebbing in human endothelial cells. *Blood* 2002; **99**: 2060-2069
37 **Houle F**, Huot J. Dysregulation of the endothelial cellular response to oxidative stress in cancer. *Mol Carcinog* 2006; **45**: 362-367
38 **Tozer GM**, Prise VE, Wilson J, Cemazar M, Shan S, Dewhirst MW, Barber PR, Vojnovic B, Chaplin DJ. Mechanisms associated with tumor vascular shut-down induced by combretastatin A-4 phosphate: intravital microscopy and measurement of vascular permeability. *Cancer Res* 2001; **61**: 6413-6422
39 **Luo Y**, Hradil VP, Frost DJ, Rosenberg SH, Gordon GB, Morgan SJ, Gagne GD, Cox BF, Tahir SK, Fox GB. ABT-751, a novel tubulin-binding agent, decreases tumor perfusion and disrupts tumor vasculature. *Anticancer Drugs* 2009; **20**: 483-492
40 **Tozer GM**, Kanthou C, Baguley BC. Disrupting tumour blood vessels. *Nat Rev Cancer* 2005; **5**: 423-435
41 **Tozer GM**, Kanthou C, Parkins CS, Hill SA. The biology of the combretastatins as tumour vascular targeting agents. *Int J Exp Pathol* 2002; **83**: 21-38
42 **Yeung SC**, She M, Yang H, Pan J, Sun L, Chaplin D. Combination chemotherapy including combretastatin A4 phosphate and paclitaxel is effective against anaplastic thyroid cancer in a nude mouse xenograft model. *J Clin Endocrinol Metab* 2007; **92**: 2902-2909
43 **Ishizaki T**, Uehata M, Tamechika I, Keel J, Nonomura K, Maekawa M, Narumiya S. Pharmacological properties of Y-27632, a specific inhibitor of rho-associated kinases. *Mol Pharmacol* 2000; **57**: 976-983
44 **Vincent L**, Kermani P, Young LM, Cheng J, Zhang F, Shido K, Lam G, Bompais-Vincent H, Zhu Z, Hicklin DJ, Bohlen P, Chaplin DJ, May C, Rafii S. Combretastatin A4 phosphate induces rapid regression of tumor neovessels and growth through interference with vascular endothelial-cadherin signaling. *J Clin Invest* 2005; **115**: 2992-3006
45 **Burns CJ**, Fantino E, Phillips ID, Su S, Harte MF, Bukczynska PE, Frazzetto M, Joffe M, Kruszelnicki I, Wang B, Wang Y, Wilson N, Dilley RJ, Wan SS, Charman SA, Shackleford DM, Fida R, Malcontenti-Wilson C, Wilks AF. CYT997: a novel orally active tubulin polymerization inhibitor with potent cytotoxic and vascular disrupting activity in vitro and in vivo. *Mol Cancer Ther* 2009; **8**: 3036-3045
46 **Galbraith SM**, Maxwell RJ, Lodge MA, Tozer GM, Wilson J, Taylor NJ, Stirling JJ, Sena L, Padhani AR, Rustin GJ. Combretastatin A4 phosphate has tumor antivascular activity in rat and man as demonstrated by dynamic magnetic resonance imaging. *J Clin Oncol* 2003; **21**: 2831-2842
47 **Prise VE**, Honess DJ, Stratford MR, Wilson J, Tozer GM. The vascular response of tumor and normal tissues in the rat to the vascular targeting agent, combretastatin A-4-phosphate, at clinically relevant doses. *Int J Oncol* 2002; **21**: 717-726
48 **Tozer GM**, Prise VE, Lewis G, Xie S, Wilson I, Hill SA. Nitric oxide synthase inhibition enhances the tumor vascular-damaging effects of combretastatin a-4 3-o-phosphate at clinically relevant doses. *Clin Cancer Res* 2009; **15**: 3781-3790
49 **Dark GG**, Hill SA, Prise VE, Tozer GM, Pettit GR, Chaplin DJ. Combretastatin A-4, an agent that displays potent and selective toxicity toward tumor vasculature. *Cancer Res* 1997; **57**: 1829-1834
50 **Rustin GJ**, Galbraith SM, Anderson H, Stratford M, Folkes LK, Sena L, Gumbrell L, Price PM. Phase I clinical trial of weekly combretastatin A4 phosphate: clinical and pharmacokinetic results. *J Clin Oncol* 2003; **21**: 2815-2822
51 **Bradley DP**, Tessier JJ, Ashton SE, Waterton JC, Wilson Z, Worthington PL, Ryan AJ. Correlation of MRI biomarkers with tumor necrosis in Hras5 tumor xenograft in athymic rats. *Neoplasia* 2007; **9**: 382-391
52 **Davis PD**, Dougherty GJ, Blakey DC, Galbraith SM, Tozer GM, Holder AL, Naylor MA, Nolan J, Stratford MR, Chaplin DJ, Hill SA. ZD6126: a novel vascular-targeting agent that causes selective destruction of tumor vasculature. *Cancer Res* 2002; **62**: 7247-7253
53 **Chen G**, Horsman MR, Pedersen M, Pang Q, Stødkilde-Jørgensen H. The effect of combretastatin A4 disodium phosphate and 5,6-dimethylxanthenone-4-acetic acid on water diffusion and blood perfusion in tumours. *Acta Oncol* 2008; **47**: 1071-1076
54 **Delmonte A**, Sessa C. AVE8062: a new combretastatin derivative vascular disrupting agent. *Expert Opin Investig Drugs* 2009; **18**: 1541-1548
55 **Sheng Y**, Hua J, Pinney KG, Garner CM, Kane RR, Prezioso JA, Chaplin DJ, Edvardsen K. Combretastatin family member OXI4503 induces tumor vascular collapse through the induction of endothelial apoptosis. *Int J Cancer* 2004; **111**: 604-610
56 **Wang H**, Li J, Chen F, De Keyzer F, Yu J, Feng Y, Nuyts J, Marchal G, Ni Y. Morphological, functional and metabolic imaging biomarkers: assessment of vascular-disrupting effect on rodent liver tumours. *Eur Radiol* 2010; **20**: 2013-2026
57 **Wang H**, Sun X, Chen F, De Keyzer F, Yu J, Landuyt W, Vandecaveye V, Peeters R, Bosmans H, Hermans R, Marchal G, Ni Y. Treatment of rodent liver tumor with combretastatin a4 phosphate: noninvasive therapeutic evaluation using multiparametric magnetic resonance imaging in correlation with microangiography and histology. *Invest Radiol* 2009; **44**: 44-53
58 **Dachs GU**, Steele AJ, Coralli C, Kanthou C, Brooks AC, Gunningham SP, Currie MJ, Watson AI, Robinson BA, Tozer GM. Anti-vascular agent Combretastatin A-4-P modulates hypoxia inducible factor-1 and gene expression. *BMC Cancer* 2006; **6**: 280
59 **Thoeny HC**, De Keyzer F, Vandecaveye V, Chen F, Sun X, Bosmans H, Hermans R, Verbeken EK, Boesch C, Marchal G, Landuyt W, Ni Y. Effect of vascular targeting agent in rat tumor model: dynamic contrast-enhanced versus diffusion-weighted MR imaging. *Radiology* 2005; **237**: 492-499
60 **Siim BG**, Laux WT, Rutland MD, Palmer BN, Wilson WR. Scintigraphic imaging of the hypoxia marker (99m)technetium-labeled 2,2'-(1,4-diaminobutane)bis(2-methyl-3-butanone) dioxime (99mTc-labeled HL-91; prognox): noninvasive detection of tumor response to the antivascular agent 5,6-dimethylxanthenone-4-acetic acid. *Cancer Res* 2000;

**60**: 4582-4588
61 **Siemann DW**, Shi W. Dual targeting of tumor vasculature: combining Avastin and vascular disrupting agents (CA4P or OXi4503). *Anticancer Res* 2008; **28**: 2027-2031
62 **Seshadri M**, Bellnier DA, Cheney RT. Assessment of the early effects of 5,6-dimethylxanthenone-4-acetic acid using macromolecular contrast media-enhanced magnetic resonance imaging: ectopic versus orthotopic tumors. *Int J Radiat Oncol Biol Phys* 2008; **72**: 1198-1207
63 **Grosios K**, Holwell SE, McGown AT, Pettit GR, Bibby MC. In vivo and in vitro evaluation of combretastatin A-4 and its sodium phosphate prodrug. *Br J Cancer* 1999; **81**: 1318-1327
64 **Seshadri M**, Toth K. Acute vascular disruption by 5,6-dimethylxanthenone-4-acetic Acid in an orthotopic model of human head and neck cancer. *Transl Oncol* 2009; **2**: 121-127
65 **Kleespies A**, Köhl G, Friedrich M, Ryan AJ, Barge A, Jauch KW, Bruns CJ. Vascular targeting in pancreatic cancer: the novel tubulin-binding agent ZD6126 reveals antitumor activity in primary and metastatic tumor models. *Neoplasia* 2005; **7**: 957-966
66 **Liu JJ**, Ching LM, Goldthorpe M, Sutherland R, Baguley BC, Kirker JA, McKeage MJ. Antitumour action of 5,6-dimethylxanthenone-4-acetic acid in rats bearing chemically induced primary mammary tumours. *Cancer Chemother Pharmacol* 2007; **59**: 661-669
67 **McPhail LD**, Chung YL, Madhu B, Clark S, Griffiths JR, Kelland LR, Robinson SP. Tumor dose response to the vascular disrupting agent, 5,6-dimethylxanthenone-4-acetic acid, using in vivo magnetic resonance spectroscopy. *Clin Cancer Res* 2005; **11**: 3705-3713
68 **Vogel-Claussen J**, Gimi B, Artemov D, Bhujwalla ZM. Diffusion-weighted and macromolecular contrast enhanced MRI of tumor response to antivascular therapy with ZD6126. *Cancer Biol Ther* 2007; **6**: 1469-1475
69 **Thomas CD**, Walczak C, Kaffy J, Pontikis R, Jouanneau J, Volk A. Early effects of combretastatin A4 phosphate assessed by anatomic and carbogen-based functional magnetic resonance imaging on rat bladder tumors implanted in nude mice. *Neoplasia* 2006; **8**: 587-595
70 **Wankhede M**, Dedeugd C, Siemann DW, Sorg BS. In vivo functional differences in microvascular response of 4T1 and Caki-1 tumors after treatment with OXi4503. *Oncol Rep* 2010; **23**: 685-692
71 **Breidahl T**, Nielsen FU, Stødkilde-Jørgensen H, Maxwell RJ, Horsman MR. The effects of the vascular disrupting agents combretastatin A-4 disodium phosphate, 5,6-dimethylxanthenone-4-acetic acid and ZD6126 in a murine tumour: a comparative assessment using MRI and MRS. *Acta Oncol* 2006; **45**: 306-316
72 **Ni Y**, Wang H, Chen F, Li J, DeKeyzer F, Feng Y, Yu J, Bosmans H, Marchal G. Tumor models and specific contrast agents for small animal imaging in oncology. *Methods* 2009; **48**: 125-138
73 **Stevenson JP**, Rosen M, Sun W, Gallagher M, Haller DG, Vaughn D, Giantonio B, Zimmer R, Petros WP, Stratford M, Chaplin D, Young SL, Schnall M, O'Dwyer PJ. Phase I trial of the antivascular agent combretastatin A4 phosphate on a 5-day schedule to patients with cancer: magnetic resonance imaging evidence for altered tumor blood flow. *J Clin Oncol* 2003; **21**: 4428-4438
74 **Beauregard DA**, Thelwall PE, Chaplin DJ, Hill SA, Adams GE, Brindle KM. Magnetic resonance imaging and spectroscopy of combretastatin A4 prodrug-induced disruption of tumour perfusion and energetic status. *Br J Cancer* 1998; **77**: 1761-1767
75 **Madhu B**, Waterton JC, Griffiths JR, Ryan AJ, Robinson SP. The response of RIF-1 fibrosarcomas to the vascular-disrupting agent ZD6126 assessed by in vivo and ex vivo 1H magnetic resonance spectroscopy. *Neoplasia* 2006; **8**: 560-567
76 **Kuhl CK**, Träber F, Schild HH. Whole-body high-field-strength (3.0-T) MR Imaging in Clinical Practice. Part I. Technical considerations and clinical applications. *Radiology* 2008; **246**: 675-696
77 **Willinek WA**, Schild HH. Clinical advantages of 3.0 T MRI over 1.5 T. *Eur J Radiol* 2008; **65**: 2-14
78 **Barth MM**, Smith MP, Pedrosa I, Lenkinski RE, Rofsky NM. Body MR imaging at 3.0 T: understanding the opportunities and challenges. *Radiographics* 2007; **27**: 1445-1462; discussion 1462-1464
79 **Di Costanzo A**, Pollice S, Trojsi F, Giannatempo GM, Popolizio T, Canalis L, Armillotta M, Maggialetti A, Carriero A, Tedeschi G, Scarabino T. Role of perfusion-weighted imaging at 3 Tesla in the assessment of malignancy of cerebral gliomas. *Radiol Med* 2008; **113**: 134-143
80 **Akisik FM**, Sandrasegaran K, Aisen AM, Lin C, Lall C. Abdominal MR imaging at 3.0 T. *Radiographics* 2007; **27**: 1433-1444; discussion 1462-1464
81 **Kuhl CK**, Träber F, Gieseke J, Drahanowsky W, Morakkabati-Spitz N, Willinek W, von Falkenhausen M, Manka C, Schild HH. Whole-body high-field-strength (3.0-T) MR imaging in clinical practice. Part II. Technical considerations and clinical applications. *Radiology* 2008; **247**: 16-35
82 **Chen G**, Jespersen S, Pedersen M, Pang Q, Horsman MR, Stødkilde Jørgensen H. Evaluation of anti-vascular therapy with texture analysis. *Anticancer Res* 2005; **25**: 3399-3405
83 **Therasse P**, Arbuck SG, Eisenhauer EA, Wanders J, Kaplan RS, Rubinstein L, Verweij J, Van Glabbeke M, van Oosterom AT, Christian MC, Gwyther SG. New guidelines to evaluate the response to treatment in solid tumors. European Organization for Research and Treatment of Cancer, National Cancer Institute of the United States, National Cancer Institute of Canada. *J Natl Cancer Inst* 2000; **92**: 205-216
84 **Dempsey MF**, Condon BR, Hadley DM. Measurement of tumor "size" in recurrent malignant glioma: 1D, 2D, or 3D? *AJNR Am J Neuroradiol* 2005; **26**: 770-776
85 **Warren KE**, Patronas N, Aikin AA, Albert PS, Balis FM. Comparison of one-, two-, and three-dimensional measurements of childhood brain tumors. *J Natl Cancer Inst* 2001; **93**: 1401-1405
86 **Koh DM**, Padhani AR. Diffusion-weighted MRI: a new functional clinical technique for tumour imaging. *Br J Radiol* 2006; **79**: 633-635
87 **Lencioni R**, Llovet JM. Modified RECIST (mRECIST) assessment for hepatocellular carcinoma. *Semin Liver Dis* 2010; **30**: 52-60
88 **Bruix J**, Sherman M, Llovet JM, Beaugrand M, Lencioni R, Burroughs AK, Christensen E, Pagliaro L, Colombo M, Rodés J. Clinical management of hepatocellular carcinoma. Conclusions of the Barcelona-2000 EASL conference. European Association for the Study of the Liver. *J Hepatol* 2001; **35**: 421-430
89 **Lang P**, Wendland MF, Saeed M, Gindele A, Rosenau W, Mathur A, Gooding CA, Genant HK. Osteogenic sarcoma: noninvasive in vivo assessment of tumor necrosis with diffusion-weighted MR imaging. *Radiology* 1998; **206**: 227-235
90 **Schima W**, Ba-Ssalamah A, Kurtaran A, Schindl M, Gruenberger T. Post-treatment imaging of liver tumours. *Cancer Imaging* 2007; **7** Spec No A: S28-S36
91 **Ni Y**, Bormans G, Chen F, Verbruggen A, Marchal G. Necrosis avid contrast agents: functional similarity versus structural diversity. *Invest Radiol* 2005; **40**: 526-535
92 **Ni Y**. Metalloporphyrins and Functional Analogues as MRI Contrast Agents. *Curr Med Imaging Rev* 2008; **4**: 96-112
93 **Chenevert TL**, Stegman LD, Taylor JM, Robertson PL, Greenberg HS, Rehemtulla A, Ross BD. Diffusion magnetic resonance imaging: an early surrogate marker of therapeutic efficacy in brain tumors. *J Natl Cancer Inst* 2000; **92**: 2029-2036
94 **Taouli B**, Koh DM. Diffusion-weighted MR imaging of the liver. *Radiology* 2010; **254**: 47-66
95 **Chiu FY**, Jao JC, Chen CY, Liu GC, Jaw TS, Chiou YY, Hsu FO, Hsu JS. Effect of intravenous gadolinium-DTPA on diffu-

sion-weighted magnetic resonance images for evaluation of focal hepatic lesions. *J Comput Assist Tomogr* 2005; **29**: 176-180
96 **Ogura A**, Hayakawa K, Miyati T, Maeda F. The effect of susceptibility of gadolinium contrast media on diffusion-weighted imaging and the apparent diffusion coefficient. *Acad Radiol* 2008; **15**: 867-872
97 **Bellin MF**, Van Der Molen AJ. Extracellular gadolinium-based contrast media: an overview. *Eur J Radiol* 2008; **66**: 160-167
98 **Prince MR**, Zhang HL, Prowda JC, Grossman ME, Silvers DN. Nephrogenic systemic fibrosis and its impact on abdominal imaging. *Radiographics* 2009; **29**: 1565-1574
99 **Bammer R**. Basic principles of diffusion-weighted imaging. *Eur J Radiol* 2003; **45**: 169-184
100 **Le Bihan D**. Molecular diffusion nuclear magnetic resonance imaging. *Magn Reson Q* 1991; **7**: 1-30
101 **Szafer A**, Zhong J, Anderson AW, Gore JC. Diffusion-weighted imaging in tissues: theoretical models. *NMR Biomed* 1995; **8**: 289-296
102 **Chenevert TL**, Brunberg JA, Pipe JG. Anisotropic diffusion in human white matter: demonstration with MR techniques in vivo. *Radiology* 1990; **177**: 401-405
103 **Le Bihan D**, Breton E, Lallemand D, Aubin ML, Vignaud J, Laval-Jeantet M. Separation of diffusion and perfusion in intravoxel incoherent motion MR imaging. *Radiology* 1988; **168**: 497-505
104 **Patterson DM**, Padhani AR, Collins DJ. Technology insight: water diffusion MRI--a potential new biomarker of response to cancer therapy. *Nat Clin Pract Oncol* 2008; **5**: 220-233
105 **Le Bihan D**, Mangin JF, Poupon C, Clark CA, Pappata S, Molko N, Chabriat H. Diffusion tensor imaging: concepts and applications. *J Magn Reson Imaging* 2001; **13**: 534-546
106 **Provenzale JM**, Engelter ST, Petrella JR, Smith JS, MacFall JR. Use of MR exponential diffusion-weighted images to eradicate T2 "shine-through" effect. *AJR Am J Roentgenol* 1999; **172**: 537-539
107 **Thoeny HC**, De Keyzer F, Chen F, Ni Y, Landuyt W, Verbeken EK, Bosmans H, Marchal G, Hermans R. Diffusion-weighted MR imaging in monitoring the effect of a vascular targeting agent on rhabdomyosarcoma in rats. *Radiology* 2005; **234**: 756-764
108 **Mulkern RV**, Gudbjartsson H, Westin CF, Zengingonul HP, Gartner W, Guttmann CR, Robertson RL, Kyriakos W, Schwartz R, Holtzman D, Jolesz FA, Maier SE. Multi-component apparent diffusion coefficients in human brain. *NMR Biomed* 1999; **12**: 51-62
109 **Yamada I**, Aung W, Himeno Y, Nakagawa T, Shibuya H. Diffusion coefficients in abdominal organs and hepatic lesions: evaluation with intravoxel incoherent motion echo-planar MR imaging. *Radiology* 1999; **210**: 617-623
110 **Sun X**, Wang H, Chen F, De Keyzer F, Yu J, Jiang Y, Feng Y, Li J, Marchal G, Ni Y. Diffusion-weighted MRI of hepatic tumor in rats: comparison between in vivo and postmortem imaging acquisitions. *J Magn Reson Imaging* 2009; **29**: 621-628
111 **Bennett KM**, Schmainda KM, Bennett RT, Rowe DB, Lu H, Hyde JS. Characterization of continuously distributed cortical water diffusion rates with a stretched-exponential model. *Magn Reson Med* 2003; **50**: 727-734
112 **Parikh T**, Drew SJ, Lee VS, Wong S, Hecht EM, Babb JS, Taouli B. Focal liver lesion detection and characterization with diffusion-weighted MR imaging: comparison with standard breath-hold T2-weighted imaging. *Radiology* 2008; **246**: 812-822
113 **van den Bos IC**, Hussain SM, Krestin GP, Wielopolski PA. Liver imaging at 3.0 T: diffusion-induced black-blood echo-planar imaging with large anatomic volumetric coverage as an alternative for specific absorption rate-intensive echo-train spin-echo sequences: feasibility study. *Radiology* 2008; **248**: 264-271
114 **Takahara T**, Imai Y, Yamashita T, Yasuda S, Nasu S, Van Cauteren M. Diffusion weighted whole body imaging with background body signal suppression (DWIBS): technical improvement using free breathing, STIR and high resolution 3D display. *Radiat Med* 2004; **22**: 275-282
115 **DeVries AF**, Kremser C, Hein PA, Griebel J, Krezcy A, Ofner D, Pfeiffer KP, Lukas P, Judmaier W. Tumor microcirculation and diffusion predict therapy outcome for primary rectal carcinoma. *Int J Radiat Oncol Biol Phys* 2003; **56**: 958-965
116 **Pope WB**, Kim HJ, Huo J, Alger J, Brown MS, Gjertson D, Sai V, Young JR, Tekchandani L, Cloughesy T, Mischel PS, Lai A, Nghiemphu P, Rahmanuddin S, Goldin J. Recurrent glioblastoma multiforme: ADC histogram analysis predicts response to bevacizumab treatment. *Radiology* 2009; **252**: 182-189
117 **Moffat BA**, Chenevert TL, Lawrence TS, Meyer CR, Johnson TD, Dong Q, Tsien C, Mukherji S, Quint DJ, Gebarski SS, Robertson PL, Junck LR, Rehemtulla A, Ross BD. Functional diffusion map: a noninvasive MRI biomarker for early stratification of clinical brain tumor response. *Proc Natl Acad Sci USA* 2005; **102**: 5524-5529
118 **Fiebach JB**, Jansen O, Schellinger PD, Heiland S, Hacke W, Sartor K. Serial analysis of the apparent diffusion coefficient time course in human stroke. *Neuroradiology* 2002; **44**: 294-298
119 **Koh DM**, Blackledge M, Collins DJ, Padhani AR, Wallace T, Wilton B, Taylor NJ, Stirling JJ, Sinha R, Walicke P, Leach MO, Judson I, Nathan P. Reproducibility and changes in the apparent diffusion coefficients of solid tumours treated with combretastatin A4 phosphate and bevacizumab in a two-centre phase I clinical trial. *Eur Radiol* 2009; **19**: 2728-2738
120 **Cui Y**, Zhang XP, Sun YS, Tang L, Shen L. Apparent diffusion coefficient: potential imaging biomarker for prediction and early detection of response to chemotherapy in hepatic metastases. *Radiology* 2008; **248**: 894-900
121 **Harry VN**, Semple SI, Parkin DE, Gilbert FJ. Use of new imaging techniques to predict tumour response to therapy. *Lancet Oncol* 2010; **11**: 92-102
122 **Perini R**, Choe R, Yodh AG, Sehgal C, Divgi CR, Rosen MA. Non-invasive assessment of tumor neovasculature: techniques and clinical applications. *Cancer Metastasis Rev* 2008; **27**: 615-630
123 **Geraldes CF**, Laurent S. Classification and basic properties of contrast agents for magnetic resonance imaging. *Contrast Media Mol Imaging* 2009; **4**: 1-23
124 **Collins DJ**, Padhani AR. Dynamic magnetic resonance imaging of tumor perfusion. Approaches and biomedical challenges. *IEEE Eng Med Biol Mag* 2004; **23**: 65-83
125 **Reimer P**, Schuierer G, Balzer T, Peters PE. Application of a superparamagnetic iron oxide (Resovist) for MR imaging of human cerebral blood volume. *Magn Reson Med* 1995; **34**: 694-697
126 **Wintermark M**, Sesay M, Barbier E, Borbély K, Dillon WP, Eastwood JD, Glenn TC, Grandin CB, Pedraza S, Soustiel JF, Nariai T, Zaharchuk G, Caillé JM, Dousset V, Yonas H. Comparative overview of brain perfusion imaging techniques. *Stroke* 2005; **36**: e83-e99
127 **Yankeelov TE**, Gore JC. Dynamic Contrast Enhanced Magnetic Resonance Imaging in Oncology: Theory, Data Acquisition, Analysis, and Examples. *Curr Med Imaging Rev* 2009; **3**: 91-107
128 **Padhani AR**, Khan AA. Diffusion-weighted (DW) and dynamic contrast-enhanced (DCE) magnetic resonance imaging (MRI) for monitoring anticancer therapy. *Target Oncol* 2010; **5**: 39-52
129 **Weisskoff RM**, Chesler D, Boxerman JL, Rosen BR. Pitfalls in MR measurement of tissue blood flow with intravascular tracers: which mean transit time? *Magn Reson Med* 1993; **29**: 553-558
130 **Jackson A**, Buckley D, Parker G. Dynamic contrast-enhanced magnetic resonance imaging in oncology. 1st ed. New York: Springer Berlin Heidelberg, 2005
131 **Ostergaard L**, Sorensen AG, Kwong KK, Weisskoff RM,

Gyldensted C, Rosen BR. High resolution measurement of cerebral blood flow using intravascular tracer bolus passages. Part II: Experimental comparison and preliminary results. *Magn Reson Med* 1996; **36**: 726-736
132 **Vonken EP**, van Osch MJ, Bakker CJ, Viergever MA. Simultaneous quantitative cerebral perfusion and Gd-DTPA extravasation measurement with dual-echo dynamic susceptibility contrast MRI. *Magn Reson Med* 2000; **43**: 820-827
133 **Padhani AR**. MRI for assessing antivascular cancer treatments. *Br J Radiol* 2003; **76** Spec No 1: S60-S80
134 **Kassner A**, Annesley DJ, Zhu XP, Li KL, Kamaly-Asl ID, Watson Y, Jackson A. Abnormalities of the contrast re-circulation phase in cerebral tumors demonstrated using dynamic susceptibility contrast-enhanced imaging: a possible marker of vascular tortuosity. *J Magn Reson Imaging* 2000; **11**: 103-113
135 **Barbier EL**, Lamalle L, Décorps M. Methodology of brain perfusion imaging. *J Magn Reson Imaging* 2001; **13**: 496-520
136 **Tofts PS**, Berkowitz BA. Rapid measurement of capillary permeability using the early part of the dynamic Gd-DTPA MRI enhancement curve. *J Magn Reson* 1993; **102**: 129-136
137 **McIntyre DJ**, Robinson SP, Howe FA, Griffiths JR, Ryan AJ, Blakey DC, Peers IS, Waterton JC. Single dose of the antivascular agent, ZD6126 (N-acetylcolchinol-O-phosphate), reduces perfusion for at least 96 hours in the GH3 prolactinoma rat tumor model. *Neoplasia* 2004; **6**: 150-157
138 **Walker-Samuel S**, Parker CC, Leach MO, Collins DJ. Reproducibility of reference tissue quantification of dynamic contrast-enhanced data: comparison with a fixed vascular input function. *Phys Med Biol* 2007; **52**: 75-89
139 **Jackson A**. Analysis of dynamic contrast enhanced MRI. *Br J Radiol* 2004; **77** Spec No 2: S154-S166
140 **Tofts PS**, Brix G, Buckley DL, Evelhoch JL, Henderson E, Knopp MV, Larsson HB, Lee TY, Mayr NA, Parker GJ, Port RE, Taylor J, Weisskoff RM. Estimating kinetic parameters from dynamic contrast-enhanced T(1)-weighted MRI of a diffusable tracer: standardized quantities and symbols. *J Magn Reson Imaging* 1999; **10**: 223-232
141 **Larsson HB**, Tofts PS. Measurement of blood-brain barrier permeability using dynamic Gd-DTPA scanning--a comparison of methods. *Magn Reson Med* 1992; **24**: 174-176
142 **Buckley DL**. Uncertainty in the analysis of tracer kinetics using dynamic contrast-enhanced T1-weighted MRI. *Magn Reson Med* 2002; **47**: 601-606
143 **Siemann DW**, Horsman MR. Vascular targeted therapies in oncology. *Cell Tissue Res* 2009; **335**: 241-248
144 **Jackson A**, O'Connor JP, Parker GJ, Jayson GC. Imaging tumor vascular heterogeneity and angiogenesis using dynamic contrast-enhanced magnetic resonance imaging. *Clin Cancer Res* 2007; **13**: 3449-3459
145 **Salmon BA**, Siemann DW. Characterizing the tumor response to treatment with combretastatin A4 phosphate. *Int J Radiat Oncol Biol Phys* 2007; **68**: 211-217
146 **Evelhoch JL**, LoRusso PM, He Z, DelProposto Z, Polin L, Corbett TH, Langmuir P, Wheeler C, Stone A, Leadbetter J, Ryan AJ, Blakey DC, Waterton JC. Magnetic resonance imaging measurements of the response of murine and human tumors to the vascular-targeting agent ZD6126. *Clin Cancer Res* 2004; **10**: 3650-3657
147 **McKeage MJ**, Fong P, Jeffery M, Baguley BC, Kestell P, Ravic M, Jameson MB. 5,6-Dimethylxanthenone-4-acetic acid in the treatment of refractory tumors: a phase I safety study of a vascular disrupting agent. *Clin Cancer Res* 2006; **12**: 1776-1784
148 **Buonaccorsi GA**, Roberts C, Cheung S, Watson Y, O'Connor JP, Davies K, Jackson A, Jayson GC, Parker GJ. Comparison of the performance of tracer kinetic model-driven registration for dynamic contrast enhanced MRI using different models of contrast enhancement. *Acad Radiol* 2006; **13**: 1112-1123
149 **Salmon HW**, Siemann DW. Effect of the second-generation vascular disrupting agent OXi4503 on tumor vascularity. *Clin Cancer Res* 2006; **12**: 4090-4094
150 **Nico B**, Benagiano V, Mangieri D, Maruotti N, Vacca A, Ribatti D. Evaluation of microvascular density in tumors: pro and contra. *Histol Histopathol* 2008; **23**: 601-607
151 **Gaya A**, Daley F, Taylor NJ, Tozer G, Qureshi U, Padhani A, Pedley RB, Begent R, Wellsted D, Stirling JJ, Rustin G. Relationship between human tumour angiogenic profile and combretastatin-induced vascular shutdown: an exploratory study. *Br J Cancer* 2008; **99**: 321-326
152 **Tozer GM**. Measuring tumour vascular response to antivascular and antiangiogenic drugs. *Br J Radiol* 2003; **76** Spec No 1: S23-S35
153 **Dalal S**, Burchill SA. Preclinical evaluation of vascular-disrupting agents in Ewing's sarcoma family of tumours. *Eur J Cancer* 2009; **45**: 713-722
154 **McPhail LD**, Griffiths JR, Robinson SP. Assessment of tumor response to the vascular disrupting agents 5,6-dimethylxanthenone-4-acetic acid or combretastatin-A4-phosphate by intrinsic susceptibility magnetic resonance imaging. *Int J Radiat Oncol Biol Phys* 2007; **69**: 1238-1245
155 **Zhao D**, Richer E, Antich PP, Mason RP. Antivascular effects of combretastatin A4 phosphate in breast cancer xenograft assessed using dynamic bioluminescence imaging and confirmed by MRI. *FASEB J* 2008; **22**: 2445-2451
156 **Maxwell RJ**, Wilson J, Prise VE, Vojnovic B, Rustin GJ, Lodge MA, Tozer GM. Evaluation of the anti-vascular effects of combretastatin in rodent tumours by dynamic contrast enhanced MRI. *NMR Biomed* 2002; **15**: 89-98
157 **van der Sanden BP**, Rozijn TH, Rijken PF, Peters HP, Heerschap A, van der Kogel AJ, Bovée WM. Noninvasive assessment of the functional neovasculature in 9L-glioma growing in rat brain by dynamic 1H magnetic resonance imaging of gadolinium uptake. *J Cereb Blood Flow Metab* 2000; **20**: 861-870
158 **de Langen AJ**, van den Boogaart VE, Marcus JT, Lubberink M. Use of H2(15)O-PET and DCE-MRI to measure tumor blood flow. *Oncologist* 2008; **13**: 631-644
159 **Niermann KJ**, Fleischer AC, Huamani J, Yankeelov TE, Kim DW, Wilson WD, Hallahan DE. Measuring tumor perfusion in control and treated murine tumors: correlation of microbubble contrast-enhanced sonography to dynamic contrast-enhanced magnetic resonance imaging and fluorodeoxyglucose positron emission tomography. *J Ultrasound Med* 2007; **26**: 749-756
160 **Padhani AR**, Miles KA. Multiparametric imaging of tumor response to therapy. *Radiology* 2010; **256**: 348-364

**S- Editor** Cheng JX **L- Editor** Kerr C **E- Editor** Zheng XM

World Journal of Radiology

Online Submissions: http://www.wjgnet.com/1949-8470office
wjr@wjgnet.com
doi:10.4329/wjr.v3.i1.17

*World J Radiol* 2011 January 28; 3(1): 17-23
ISSN 1949-8470 (online)
© 2011 Baishideng. All rights reserved.

ORIGINAL ARTICLE

# CT patterns of nodal disease in pediatric chest tuberculosis

Amar Mukund, Rashmi Khurana, Ashu S Bhalla, Arun K Gupta, Sushil K Kabra

Amar Mukund, Rashmi Khurana, Ashu S Bhalla, Arun K Gupta, Department of Radiology, All India Institute of Medical Sciences, New Delhi 110029, India
Sushil K Kabra, Department of Pediatrics, All India Institute of Medical Sciences, New Delhi 110029, India
Author contributions: Mukund A and Khurana R were responsible for performing the radiological investigation and involved in data analysis; Bhalla AS and Gupta AK were involved in analysis of imaging and manuscript preparation; Kabra SK performed the clinical evaluation of the patients.
Correspondence to: Dr. Ashu S Bhalla, Department of Radiology, All India Institute of Medical Sciences, Ansari Nagar, New Delhi 110029, India. ashubhalla1@yahoo.com
Telephone: +91-11-265949258 Fax: +91-11-26588641
Received: December 24, 2010 Revised: January 18, 2011
Accepted: January 25, 2011
Published online: January 28, 2011

## Abstract

**AIM:** To highlight various patterns of nodal involvement and post treatment changes in pediatric chest tuberculosis based on contrast enhanced computed tomography (CECT) scans of chest.

**METHODS:** This was a retrospective study consisting of 91 patients aged less than 17 years, who attended Paediatrics OPD of All India Institute of Medical Sciences with clinically diagnosed tuberculosis or with chest radiographs suggestive of chest tuberculosis. These patients had an initial chest radiograph as well as CECT of the chest and follow up imaging after 6 mo, and in some cases 9 mo, of completion of anti-tubercular treatment (ATT). CECT of these patients was reviewed for the location and extent of nodal involvement along with determination of site, size, enhancement pattern and calcification.

**RESULTS:** Enlargement of mediastinal or hilar lymph nodes was found in 88/91 patients (96.7%), with the most common locations being paratracheal (84.1%), and subcarinal (76.1%). The most common pattern of enhancement was found to be inhomogenous. The nodes were conglomerate in 56.8% and discrete in 43.2%. In addition, perinodal fat was obscured in 84.1% of patients. In the post-treatment scan, there was 87.4% reduction in the size of the nodes. All nodes post-treatment were discrete and homogenous with perinodal fat present. Calcification was found both pre- and post-treatment, but there was an increase in incidence after treatment (41.7%). There was hence a reduction in size, change in enhancement pattern, and appearance of perinodal fat with treatment.

**CONCLUSION:** Tubercular nodes have varied appearance and enhancement pattern. Conglomeration and obscuration of perinodal fat suggest activity. In residual nodes decision to continue ATT requires clinical correlation.

© 2011 Baishideng. All rights reserved.

**Key words:** Tuberculosis; Lymph nodes; Contrast enhanced computed tomography

**Peer reviewer:** Francesco Lassandro, MD, Department of Radiology, Monaldi Hospital, via Leonardo Bianchi, Napoli, 80129, Italy

Mukund A, Khurana R, Bhalla AS, Gupta AK, Kabra SK. CT patterns of nodal disease in pediatric chest tuberculosis. *World J Radiol* 2011; 3(1): 17-23 Available from: URL: http://www.wjgnet.com/1949-8470/full/v3/i1/17.htm DOI: http://dx.doi.org/10.4329/wjr.v3.i1.17

## INTRODUCTION

Tuberculosis is one of the major causes of morbidity and mortality worldwide. Children represent one of the high risk groups in the resurgence of the disease. Pediatric patients generally have primary tuberculosis, presenting as Ghon's complex, consisting of small parenchymal infiltrates with lymphatic spread leading to mediastinal and hilar lymphadenopathy. This generally heals but may prog-

ress to progressive pulmonary tuberculosis in 5%-10% of patients.

Chest radiography may not be sensitive in detecting lymphadenopathy, which is considered to be the fingerprint of primary pulmonary tuberculosis. Moreover, computed tomography (CT) is considered the imaging modality of choice to diagnose the presence, location and characteristics of mediastinal adenopathy. The advantages of CT are the characterization of lesions by showing low attenuation nodes with rim enhancement, calcification, nodules of bronchogenic spread, or miliary disease, in defining the extent of tuberculous disease and its complications and in differentiating active from inactive phases[1-5]. This study describes the various CT patterns of nodal involvement in pediatric chest tuberculosis in active as well as in post-treatment phases.

## MATERIALS AND METHODS

In this retrospective study (from December 2006 to December 2009) we analyzed the CT scans of 91 patients less than 17 years of age who were diagnosed with tuberculosis on the basis of clinical and/or radiographic and/or pathological data. CT was performed after administration of non ionic contrast [Iomeron 400 (Iomeprol, Bracco, Milano, Italy), Iohexol 300 (Omnipaque, GE Health care, Ireland)] which was injected by hand leading to an average delay of 50 to 70 s and thus providing venous phase images. The dose of contrast was calculated based on the body weight of the child, not exceeding 2 mL/kg body weight. CT scans of these patients were reviewed by two radiologists with 20 years and 5 years experience, respectively, in thoracic imaging.

Medical records of these patients were thoroughly studied by a clinical investigator who looked for presenting clinical symptoms, history of *Mycobacterium tuberculosis* contact, previous diagnoses of tuberculosis, demographic information, and status of BCG vaccination, a Mantoux test result and isolation of acid fast bacilli (AFB).

### Inclusion criteria

Patients who presented with clinical symptoms suggestive of active tuberculosis like cough for more than 2 wk, fever, weight loss, hemoptysis, anorexia, dyspnea and weakness were included. Apart from these clinical features at least 2 of the following 4 criteria had to be fulfilled: (1) A tuberculin skin test with 5 tuberculin units PPD, showing area of induration more than 10 mm; (2) Radiographic findings compatible with *Mycobacterium tuberculosis* like miliary disease, cavitary lesions, hilar lymphadenopathy or primary complex; (3) History of adult source patient with contagious disease, caused by *Mycobacterium tuberculosis*; and (4) Isolation of AFB from sputum, FNAC from cervical nodes, bronchioalveolar lavage, or other sites like empyema, *etc*.

Informed consent and clearance from the local ethical committee was not required due to the retrospective nature of the study.

**Table 1 Demographic profile of patients *n* (%)**

| Variables | Frequency (*n* = 91) |
|---|---|
| Age group (yr) | |
| 0-5 | 19 (20.9) |
| 5-10 | 26 (28.6) |
| 10-15 | 39 (42.9) |
| 15-17 | 7 (7.7) |
| Sex | |
| Male | 47 (51.6) |
| Female | 44 (48.4) |
| Presenting symptoms | |
| Fever | 88 (96.7) |
| Cough | 56 (61.5) |
| Weight loss | 78 (85.7) |
| Loss of appetite | 90 (98.9) |
| Lymphadenopathy | 38 (41.7) |
| History of contact | 41 (45.0) |
| Laboratory investigations | |
| Mantoux positivity | 91 (100) |
| Elevated ESR | 65 (71.4) |
| AFB detection | 20 (22.0) |

ESR: Erythrocyte sedimentation rate; AFB: Acid fast bacilli.

### Contrast enhanced CT chest

An initial CT scan done within 30 d of commencement of anti-tubercular treatment (ATT) was available in all these patients. Amongst these, 45 patients had a follow up CT performed following 6 mo of treatment. Some patients with persistent nodes underwent a 3rd scan after 9 mo of ATT.

Contrast enhanced CT (CECT) was assessed for the location and extent of nodal, parenchymal, airway, and pleural involvement. Particular attention was given to the site, size, enhancement pattern and calcification of the lymph nodes. Mediastinal nodes having a size > 1 cm in the short axis were considered abnormal. In addition sites of nodal involvement were also analyzed. The enhancement pattern was categorized into three groups consisting of homogeneously enhancing nodes, nodes with peripheral enhancement and central necrosis and inhomogeneous nodes. The nodes were also classified as being discrete or conglomerate and we looked for presence or obscuration of perinodal fat. Discrete nodes were defined as having smooth, well defined margins with preserved adjacent fat; whereas clubbed or clusters of nodes with ill defined margins and adjacent fat streakiness were called conglomerate. Nodes with ill defined fuzzy margins with loss of adjacent fat or fat stranding were said to have obscuration of perinodal fat.

Further size as well as the enhancement pattern of the nodes was compared with the follow up CT done after 6 and 9 mo.

## RESULTS

The clinical profile of the study population is depicted in Table 1. The 91 patients (47 males, 44 females) aged 3 mo to 17 years had a majority of patients (42.9%) in the age group of 10 to 15 years, with a median age of 11 years.

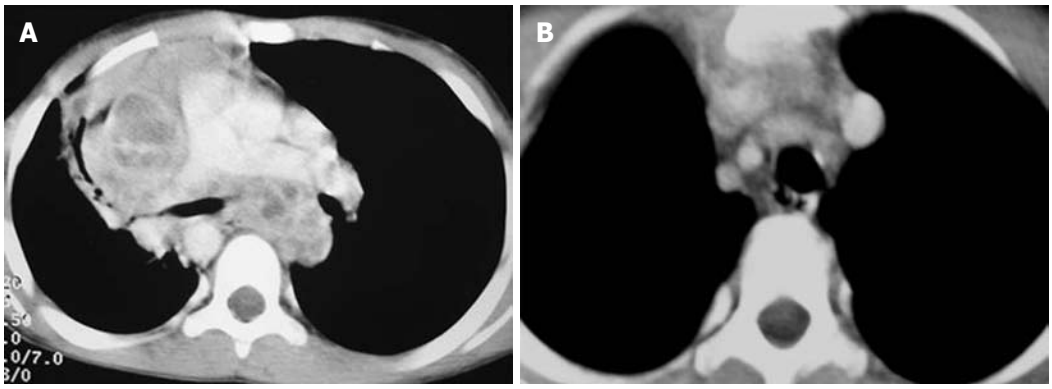


**Figure 1 Computed tomography chest of a patient (A) showing large, conglomerate rim enhancing nodes, with central necrosis (B) post anti-tubercular treatment, showing resolution of adenopathy, with appearance of perinodal fat.**

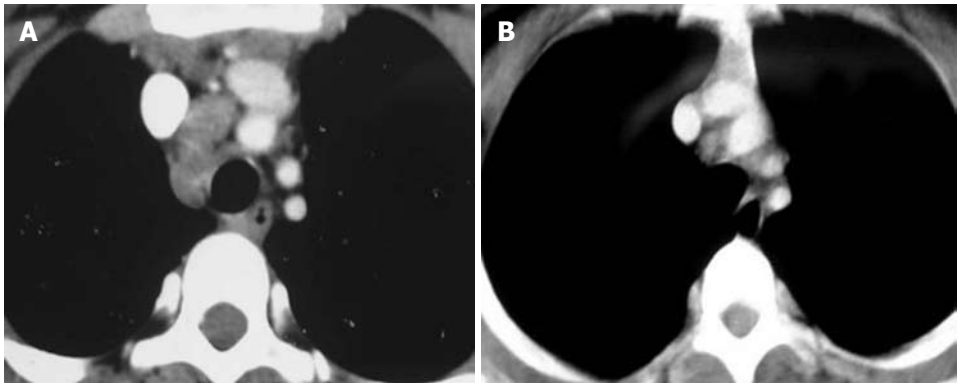


**Figure 2 Pretreatment computed tomography (A) showing conglomerate, inhomogenous paratracheal lymph nodes and follow up computed tomography (B) showing reduction in size of the nodes to < 1 cm size, with reappearance of perinodal fat.**

**Table 2 Computed tomography findings *n* (%)**

| Findings | Frequency (*n* = 91) |
|---|---|
| Lymph nodal involvement | 88 (96.7) |
| Parenchymal lesion | 64 (70.3) |
| Airway disease | 32 (35.2) |
| Pleural lesion | 18 (19.8) |

Most of the patients presented with a plethora of symptoms with the commonest being fever (96.7%), weight loss (85.7%) and loss of appetite (98.9%). Of these, Mantoux positivity was seen in all patients (100%) whereas elevated ESR in 61 (71.4%) cases and AFB could be isolated in only 20 (22%) cases.

An initial CT scan performed within 30 d of commencement of ATT was available for all 91 patients. It was reviewed for nodal, parenchymal, airway, and pleural lesions (Table 2). Enlargement of mediastinal or hilar lymph nodes was found in 88 patients (96.7%). The nodal distribution and lymph node size is described in Table 3. The most common site for lymphadenopathy was the paratracheal location, and the largest nodes were seen in prevascular and subcarinal locations. The incidence of lymphadenopathy in children < 5 years was 19/19 (100%), while that in children > 5 years was 69/72 (96%).

**Table 3 Nodal distribution and characteristics**

| | Frequency (*n* = 88) | % |
|---|---|---|
| Nodal distribution | Frequency and mean size | |
| Paratracheal | 74 (2.21 cm) | 84.1 |
| Pretracheal | 50 (1.62 cm) | 56.8 |
| Precarinal | 48 (1.72 cm) | 54.4 |
| Subcarinal | 67 (2.03 cm) | 76.1 |
| Right hilar | 46 (1.87 cm) | 52.3 |
| Left hilar | 32 (1.68 cm) | 36.4 |
| Prevascular | 22 (2.82 cm) | 25.0 |
| Azygoesophageal | 30 (1.9 cm) | 34.1 |
| Aorto-pulmonary window | 10 (2.0 cm) | 11.4 |
| Nodal characteristics | | |
| Enhancement pattern | | |
| Peripheral rim | 12 | 13.6 |
| Homogeneous | 30 | 34.1 |
| Inhomogeneous | 46 | 52.3 |
| Calcification | 25 | 28.4 |
| Conglomerate | 50 | 56.8 |
| Discrete | 38 | 43.2 |
| Obscured perinodal fat | 74 | 84.1 |

Enlarged nodes displayed 3 patterns of enhancement consisting of homogeneous, inhomogeneous and peripherally enhancing nodes with central necrosis (Figures 1-3). A homogeneous and inhomogenous pattern of enhancement was more common than peripheral enhancement.

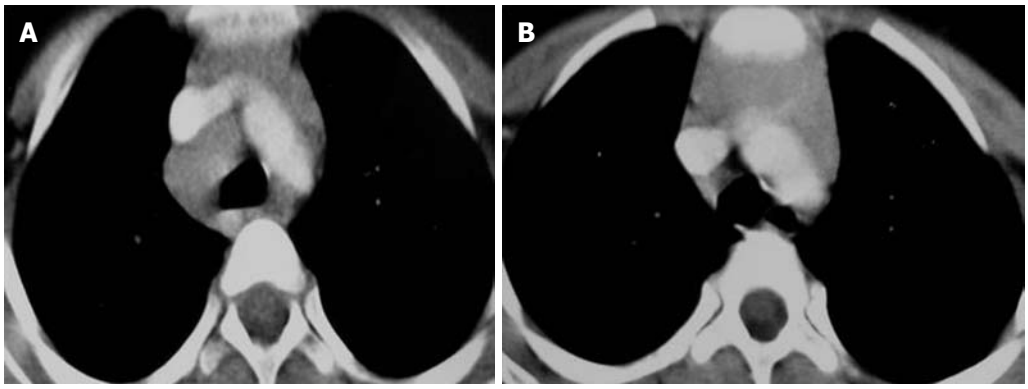


**Figure 3 Computed tomography (A) showing conglomerate, homogenous paratracheal lymph nodes and (B) showing reduction in size of the nodes (< 1 cm) after treatment.**

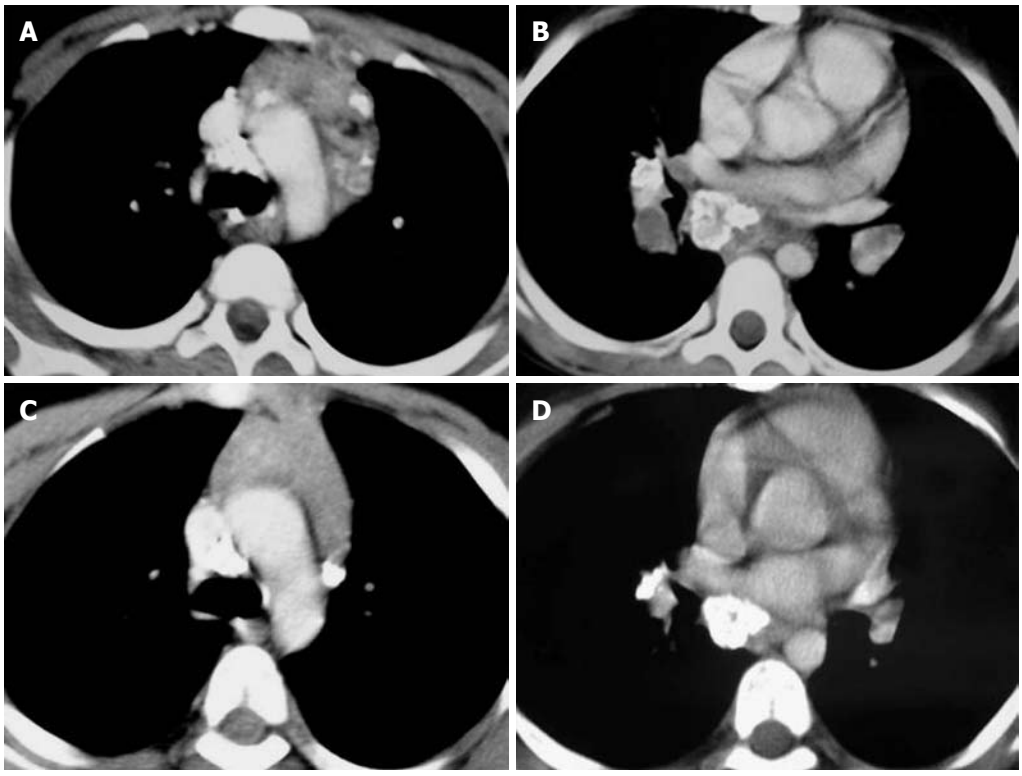


**Figure 4 Pretreatment computed tomography (A, B) showing calcified precarinal, prevascular, right hilar, and azygoesophageal nodes, with necrotic areas and follow up computed tomography after anti-tubercular treatment (C, D) showing resolution of necrotic areas, with residual calcification.**

Nodal calcification was seen even in the pre-treatment scan of 25 patients (28.4%). The majority of patients had conglomerate nodes in the initial scan and most of the patients (84.1%) showed obscuration of perinodal fat.

In 45 of these 91 patients a follow up scan (performed 6-7 mo after ATT) was available. Comparison of pre- and post-treatment scans of these 45 patients was made. Regression of nodes was seen in 30 patients (Figures 1-3). Out of 30 patients, 6 patients showed complete resolution of nodes whereas 24 had nodes < 1 cm in the short axis. These nodes were insignificant according to the size criteria; we, however, studied these small nodes for morphological characteristics. In the post-treatment CT, these nodes were discrete. Perinodal fat was obscured in 17 patients in pre-treatment scans and it reappeared in all patients in post-treatment scans (Figures 1-3). A peripheral and inhomogenous pattern of enhancement changed to a homogenous pattern of enhancement (Figure 2). Calcification was found in 8 patients in the pre-treatment scan and 10 patients after treatment (41.7%) (Figure 4 and Table 4).

The comparison between active and inactive disease ($n = 30$) was made using McNemar test and a value of $P < 0.05$ was regarded as significant. For comparison between size of nodes, Wilcoxon signed ranks test was used. There was a statistically significant reduction in the size of nodes. The difference in the incidence of peripheral, inhomogenous, and mixed patterns of enhancement, conglomerate nodes and obscuration of perinodal fat was statistically significant.

**Table 4 Comparison of nodal characteristics pre- and post-treatment**

| Lymph nodal characteristics | Frequency ($n$ = 30) | | $P$ value |
|---|---|---|---|
| | Pre-treatment | Post-treatment | |
| Lymph nodes seen with mean size | 30 (1.83 cm) | 24 (0.23 cm) | < 0.05 |
| Enhancement pattern | | | |
| Peripheral rim | 3 | 0 | < 0.05 |
| Homogeneous | 7 | 24 | > 0.05 |
| Inhomogeneous | 20 | 0 | < 0.05 |
| Calcification | 8 | 10 | > 0.05 |
| Conglomerate | 11 | 0 | < 0.05 |
| Discrete | 19 | 24 | > 0.05 |
| Obscured perinodal fat | 17 | 0 | < 0.05 |

**Table 5 Nodal characteristics in patients who had residual disease at 6 mo**

| Nodes | Pre-treatment | 6 mo | 9 mo |
|---|---|---|---|
| Mean size (cm) | 2.4 | 1.8 | 1.4 |
| Maximum size (cm) | 5 | 4.5 | 3.5 |
| Enhancement | | | |
| Peripheral rim | 2 | 2 | 1 |
| Homogeneous | 0 | 1 | 2 |
| Inhomogeneous | 1 | 0 | 0 |
| Calcification | 1 | 1 | 1 |
| Conglomerate | 1 | 1 | 1 |
| Discrete | 2 | 2 | 2 |
| Obscured perinodal fat | 2 | 1 | 0 |

Fifteen patients had nodes > 1 cm, which were hence within the significant range using the size criteria. The decision for continuing or stopping ATT in these patients was based on correlation of radiological and clinical findings. A further follow up scan after 3 mo was available in 9 patients divided into 2 groups - one in whom ATT was continued ($n$ = 7) and the other in whom ATT was discontinued ($n$ = 2) (Table 5). Though a constant reduction in the mean and maximum size of the nodes was noted as the duration of treatment progressed, at the end of 9 mo of ATT, significant nodes (> 1 cm) persisted in 3 cases, with few showing rim enhancement and conglomeration, suggesting activity.

## DISCUSSION

Tuberculosis continues to be a major health problem all over the world, especially in developing countries. Pediatric cases are particularly important epidemiologically because each usually represents a new infection rather than reactivation of prior disease. Indeed it is said that, "Children with primary tuberculosis are the reservoir from which future cases will emerge"[6].

Lymphadenopathy is the most common finding in primary TB. In a study by Lamont *et al*[7], it was concluded that lymphadenopathy was the most common single manifestation of primary tuberculosis in children, occurring in two-thirds of patients in a series of 154 patients, 90% of whom had associated parenchymal abnormalities. Weber *et al*[8] reported lymphadenopathy in 96% of cases. Leung *et al*[9] found lymphadenopathy was present in 92% cases on chest radiography, and it was the most common abnormality detected. We found enlargement of mediastinal or hilar lymph nodes in 88/91 patients (96.7%), which is comparable to other reports.

### Location

The common sites of lymphadenopathy reported in primary tuberculosis are right paratracheal, hilar and subcarinal. Leung *et al*[9] noted that the most common sites were right paratracheal and hilar. Andronikou *et al*[10] observed that the most frequently involved location was subcarinal (90%), followed by the hilar (85%), anterior mediastinum (79%), precarinal (64%) and right paratracheal (63%). Multiple sites were involved in 88% of patients and a single site (subcarinal) was present in only 4% of patients. Nodes at all the sites simultaneously were present in 35% of patients. Kim *et al*[11] found that right paratracheal nodes (73%) were the most common, followed by right hilar (34.1%). Our study was in concordance with the above studies, with the most common locations being paratracheal (84.1%), subcarinal (76.1%), pretracheal (56.8%), precarinal (54.5%), and right hilar (52.3%). Prevascular nodes were enlarged in 25% of patients. Lymph node involvement was found in a single site in only 1 (1.1%) patient, involving the right paratracheal node, while in the rest of the patients multiple sites were involved. Lymph nodes were seen in all the sites in 4 (4.4%) patients.

### Size

In a study by Andronikou *et al*[10], subcarinal was the most commonly affected site and also the site with the largest nodes. Other sites with the largest lymph nodes were prevascular and paratracheal. We also observed that the largest nodes were found in the prevascular (6.5 cm), subcarinal (5.5 cm), and paratracheal (5 cm) nodes.

### Characteristics

Though the typical enhancement pattern reported in tuberculosis is peripheral rim enhancement with central necrosis, several studies have described other patterns, like homogenous and inhomogenous enhancement. Kim *et al*[11] found that 70.7% of patients had nodes with a low attenuation centre and enhancing rim. In the study by Andronikou *et al*[10], enhancement was present in 67% and was invariably ghost like, rather than ring enhancing. In our study, we found the most common pattern enhancement to be inhomogeneous (52.3%) followed by homogeneous (34.1%) and rim enhancing (13.6%). The major difference observed in our study was the presence of homogeneous nodes which has not been reported in pediatric studies; however in a study in adults, the incidence was reported to be 9%[12].

We also observed calcification in 28.4% of patients, as compared to the reported incidence of 9% by Andronikou *et al*[10], and 12.2% by Kim *et al*[11]. In the present study, we observed conglomeration of nodes and obliteration of

perinodal fat as an important indicator of active disease. The nodes were conglomerate in 56.8% and discrete in 43.2%. In addition, perinodal fat was obscured in 84.1% patients. The pediatric studies did not make a mention of these characteristics. In a study in adults, by Pombo *et al*[12], obliteration of perinodal fat was found in 39.5% of patients.

To the best of our knowledge, there is no study in a pediatric population which has compared the nodal characteristics on imaging before and after treatment in children. In a study in adults, by Moon *et al*[13], 49 patients were studied, of which 37 were classified as active and 12 as inactive on the basis of lymph nodal biopsy. They reported that in 100% of patients with active disease, the nodes had peripheral rim enhancement with central low attenuation on CT. Calcification was observed in 19%. On the other hand, in inactive disease the nodes were homogenous, without central low attenuation areas, and calcification was found in 83% of patients. The central hypodense areas pathologically corresponded to areas of caseation necrosis. In the present study, we found small nodes in 24/30 patients (80%), which were insignificant as they were < 1 cm in size. The mean size of the nodes was 0.23 cm, with 87.4% reduction in size of the nodes, as compared to the initial scan. All nodes in the post-treatment scan were discrete and homogenous with visible surrounding perinodal fat. Calcification was found in both pre- and post-treatment scans, but there was an increase in its incidence after treatment (41.7%). Hence, although nodes were seen on follow up, these were insignificant as per size criteria.

Thus, there was a reduction in size, change in the enhancement pattern, and reappearance of perinodal fat with treatment. Our study correlated with the study by Moon *et al*[13] in adults, in terms of homogenous nodes without necrosis in the post-treatment CT. However, the incidence of calcification in inactive disease was lower in our study.

In our study, there were 15 patients who had residual disease on imaging after 6 mo of ATT. Even though there was a 52% reduction in the size of nodes the mean size was still significant. There was an increase in the number of patients showing homogenous nodes, but still 33.3% patients showed peripheral and inhomogenous enhancement. Obscuration of perinodal fat was found in 13.3% of patients. Thus, though there was a response to treatment, significant nodes persisted after 6 mo. Further follow-up CT at 9 mo was available in 9 patients which showed regression of nodes, either with ATT ($n$ = 4), or without ATT ($n$ = 2). Hence, in all patients, nodes became insignificant, except in 3 patients in whom the clinical signs of activity still persisted. The decision for continuation or discontinuation of ATT was based on clinical signs of activity.

Hence, residual sizable nodes at the end of 6 mo of ATT did not necessarily indicate an active disease on the basis of radiological finding alone. Rather the evaluation of activity required a clinical correlation. Hence, nodes of size > 1 cm represented an active disease only in symptomatic patients. We have reached this conclusion based on the fact that our patients who became clinically inactive at 6 mo ($n$ = 2) showed regression of nodes at 9 mo to insignificant size despite stopping the ATT at 6 mo. The rate of regression, however, was variable in children, ranging from 6 to 9 mo. We do not have a pathological correlation to say that the residual nodes were active or inactive, and the decision to treat these nodes was based on clinical correlation. Also to ascertain the significance of residual nodes, particularly in asymptomatic children, and to determine whether nodes should determine the end point of treatment, further studies with histopathological correlation can only conclusively prove activity *vs* inactivity in these patients. Although the numbers in our study are small for making any definite conclusions we recommend that in patients having > 1 cm size nodes on completion of 6 mo of treatment the decision to continue or stop treatment should be based on clinical and radiological correlation.

To conclude, tubercular nodes may have varied appearances, the most common being inhomogeneous and only a small number of patients having typical rim enhancement with central necrosis. However, homogeneous enlargement does not exclude tubercular etiology. Major determinants of disease activity are nodal enlargement, conglomeration and obscuration of perinodal fat. The decision to continue or withdraw ATT should always be taken after correlating clinical and imaging findings as persistent homogeneous and discrete but enlarged/equivocal nodes may not always suggest active disease.

## COMMENTS

### Background

This study aims to highlight various patterns of nodal involvement and post-treatment changes in pediatric chest tuberculosis based on contrast enhanced computed tomography (CECT) scans of the chest.

### Innovations and breakthroughs

We inferred that tubercular nodes which are < 1 cm, homogenous, discrete and with surrounding perinodal fat are inactive, while > 1 cm nodes with any pattern of enhancement (homogenous, rim like, or inhomogenous) should be considered active. Calcification can be seen in both active and inactive nodes.

### Applications

Residual mediastinal/hilar lymph nodes do not necessarily indicate disease activity; rather it is the clinical scenario along with the trend of regression of nodes which suggests if the disease is active or not.

### Peer review

This is a very interesting and well conducted study. However there are some points to be clarified.

## REFERENCES


1 **Im JG**, Itoh H, Shim YS, Lee JH, Ahn J, Han MC, Noma S. Pulmonary tuberculosis: CT findings--early active disease and sequential change with antituberculous therapy. *Radiology* 1993; **186**: 653-660

2 **Moon WK**, Im JG, Yeon KM, Han MC. Mediastinal tuberculous lymphadenitis: CT findings of active and inactive disease. *AJR Am J Roentgenol* 1998; **170**: 715-718

3 **Lee KS**, Hwang JW, Chung MP, Kim H, Kwon OJ. Utility of CT in the evaluation of pulmonary tuberculosis in patients without AIDS. *Chest* 1996; **110**: 977-984

4 **Hatipoğlu ON**, Osma E, Manisali M, Uçan ES, Balci P, Akkoçlu A, Akpinar O, Karlikaya C, Yüksel C. High resolution computed tomographic findings in pulmonary tuberculosis. *Thorax* 1996; **51**: 397-402

5 **Poey C**, Verhaegen F, Giron J, Lavayssiere J, Fajadet P, Duparc B. High resolution chest CT in tuberculosis: evolutive patterns and signs of activity. *J Comput Assist Tomogr* 1997; **21**: 601-607

6 **Agrons GA**, Markowitz RI, Kramer SS. Pulmonary tuberculosis in children. *Semin Roentgenol* 1993; **28**: 158-172

7 **Lamont AC**, Cremin BJ, Pelteret RM. Radiological patterns of pulmonary tuberculosis in the paediatric age group. *Pediatr Radiol* 1986; **16**: 2-7

8 **Weber AL**, Bird KT, Janower ML. Primary tuberculosis in childhood with particular emphasis o hanges affecting the tracheobronchial tree. *Am J Roentgenol Radium Ther Nucl Med* 1968; **103**: 123-132

9 **Leung AN**, Müller NL, Pineda PR, FitzGerald JM. Primary tuberculosis in childhood: radiographic manifestations. *Radiology* 1992; **182**: 87-91

10 **Andronikou S**, Joseph E, Lucas S, Brachmeyer S, Du Toit G, Zar H, Swingler G. CT scanning for the detection of tuberculous mediastinal and hilar lymphadenopathy in children. *Pediatr Radiol* 2004; **34**: 232-236

11 **Kim WS**, Moon WK, Kim IO, Lee HJ, Im JG, Yeon KM, Han MC. Pulmonary tuberculosis in children: evaluation with CT. *AJR Am J Roentgenol* 1997; **168**: 1005-1009

12 **Pombo F**, Rodríguez E, Mato J, Pérez-Fontán J, Rivera E, Valvuena L. Patterns of contrast enhancement of tuberculous lymph nodes demonstrated by computed tomography. *Clin Radiol* 1992; **46**: 13-17

13 **Moon WK**, Im JG, Yeon KM, Han MC. Tuberculosis of the central airways: CT findings of active and fibrotic disease. *AJR Am J Roentgenol* 1997; **169**: 649-653


**S- Editor** Cheng JX **L- Editor** O'Neill M **E- Editor** Zheng XM

World Journal of Radiology

Online Submissions: http://www.wjgnet.com/1949-8470office
wjr@wjgnet.com
doi:10.4329/wjr.v3.i1.24

*World J Radiol* 2011 January 28; 3(1): 24-31
ISSN 1949-8470 (online)
© 2011 Baishideng. All rights reserved.

BRIEF ARTICLE

# Content-based image retrieval applied to BI-RADS tissue classification in screening mammography

Júlia Epischina Engrácia de Oliveira, Arnaldo de Albuquerque Araújo, Thomas M Deserno

Júlia Epischina Engrácia de Oliveira, Arnaldo de Albuquerque Araújo, Department of Computer Science, Universidade Federal de Minas Gerais, 31270-901, Belo Horizonte, MG, Brazil
Thomas M Deserno, Department of Medical Informatics, RWTH Aachen University, 52074, Aachen, Germany
Author contributions: de Oliveira JEE performed the majority of experiments, and provided major parts of the manuscript; Araújo A de A initiated the investigation and was involved in editing the manuscript; Deserno TM provided the data collection and contributed to the study design as well as writing of the manuscript.
Supported by CNPq-Brazil, Grants 306193/2007-8, 471518/2007-7, 307373/2006-1 and 484893/2007-6, by FAPEMIG, Grant PPM 347/08, and by CAPES; The IRMA project is funded by the German Research Foundation (DFG), Le 1108/4 and Le 1108/9
Correspondence to: Júlia Epischina Engrácia de Oliveira, PhD, Department of Computer Science, Universidade Federal de Minas Gerais, Av. Antônio Carlos, 6627, 31270-901, Belo Horizonte, MG, Brazil. julia@dcc.ufmg.br
Telephone: +55-31-34095854 Fax: +55-31-34095858
Received: November 8, 2010 Revised: December 8, 2010
Accepted: December 15, 2010
Published online: January 28, 2011

## Abstract

**AIM:** To present a content-based image retrieval (CBIR) system that supports the classification of breast tissue density and can be used in the processing chain to adapt parameters for lesion segmentation and classification.

**METHODS:** Breast density is characterized by image texture using singular value decomposition (SVD) and histograms. Pattern similarity is computed by a support vector machine (SVM) to separate the four BI-RADS tissue categories. The crucial number of remaining singular values is varied (SVD), and linear, radial, and polynomial kernels are investigated (SVM). The system is supported by a large reference database for training and evaluation. Experiments are based on 5-fold cross validation.

**RESULTS:** Adopted from DDSM, MIAS, LLNL, and RWTH datasets, the reference database is composed of over 10 000 various mammograms with unified and reliable ground truth. An average precision of 82.14% is obtained using 25 singular values (SVD), polynomial kernel and the one-against-one (SVM).

**CONCLUSION:** Breast density characterization using SVD allied with SVM for image retrieval enable the development of a CBIR system that can effectively aid radiologists in their diagnosis.

© 2011 Baishideng. All rights reserved.

**Key words:** Computer-aided diagnosis; Content-based image retrieval; Image processing; Screening mammography; Singular value decomposition; Support vector machine

**Peer reviewers:** Ragab Hani Donkol, Professor, Radiology Department, Aseer Central Hospital, 34 Abha, Saudi Arabia; Ioannis Valais, PhD, Department of Medical Instrument Technology, Technological Educational Institution of Athens, Ag Spyridonos and Dimitsanis, Egaleo, Athens, 12210, Greece

de Oliveira JEE, Araújo A de A, Deserno TM. Content-based image retrieval applied to BI-RADS tissue classification in screening mammography. *World J Radiol* 2011; 3(1): 24-31 Available from: URL: http://www.wjgnet.com/1949-8470/full/v3/i1/24.htm DOI: http://dx.doi.org/10.4329/wjr.v3.i1.24

## INTRODUCTION

Breast cancer represents one of the main causes of death among women in occidental countries[1], and its early detection is the most effective way to reduce mortality with mammography posing as the best method of screening. Breast tissue density has been shown to be related to the risk of development of breast cancer[2], since dense breast tissue can hide lesions, causing the disease to be

detected at later stages. As a result, there is also a decline in the sensitivity of mammography with increasing breast density. The Breast Imaging Reporting and Data System (BI-RADS)[3], developed by the American College of Radiology (ACR) (http://www.acr.org), provides a standardized density scale. BI-RADS defines density as (1) almost entirely fatty; (2) heterogeneously dense tissue; and (3) extremely dense tissue.

Besides visual evaluation and the report of breast density by radiologists, computer-aided diagnosis (CAD) and content-based image retrieval (CBIR) may assist the radiologist to improve the reliability of medical findings, and to decrease the number of breast biopsies from benign tissue[4-6]. CBIR aims at retrieving images from a database, which are relevant to a given query[7-9]. Information access is based on comparing visual attributes that are extracted from the image. The definition of a set of features (so-called feature vector or signature, which is capable of effectively describing each region of the image) and an appropriate similarity measure are the most complex tasks affecting all subsequent steps of a CBIR system[10].

An effective CAD or CBIR system, i.e. a system that provides diagnostic information of the image or a system that effectively presents similar images according to a certain pattern, must be evaluated using a large number of reference images with approved findings (ground truth). Nevertheless, published studies are usually based on a rather small set of data. For instance, Castella *et al*[11] developed a semi-automatic method in order to estimate the ACR breast density category using features extracted from 352 mammograms from Grangettes Hospital (http://www.grangettes.ch), Geneva, Switzerland. Sheshadri *et al*[12] used 60 mammograms of the Mammographic Image Analysis Society digital mammogram database (MIAS) (http://peipa.essex.ac.uk/ipa/pix/mias/) to characterize breast tissue density according to the BI-RADS categories. The mean, standard deviation, smoothness, third moment, uniformity, and entropy from the intensity histograms have been used to describe the tissue texture. Wang *et al*[13] used 195 mammograms from the Medical Center of Pittsburgh (http://www.upmc.com/Services/Radiology/Pages/default.aspx) in order to automatically evaluate breast density according to the BI-RADS categories. Bovis *et al*[14] proposed to increase breast cancer detection sensitivity through breast density classification using 377 mammograms taken from the Digital Database for Screening Mammography (DDSM) (http://marathon.csee.usf.edu/mammography/database.html), although DDSM provides about 10 000 images. Therefore, the reliability of classification rates published in these studies is ambiguous, and the smallness of the data hinders the generalization of results obtained.

Furthermore, the appropriate characterization of images, the storage and management of the large amount of image data produced by hospitals and medical centers are not straightforward issues to be jointly taken care of. Although large databases for mammography are publicly available[15], the problem of reference data requirement is manifold, and a sufficient number of appropriate cases for CAD and CBIR development and evaluation is needed.

From a clinical point of view, CBIR systems based on breast density can guide radiologists in the detection of a lesion and its classification. Moreover, from a technical point of view, this system is the first step, and a very important one, for the development of a CAD system. Based on the Image Retrieval in Medical Applications (IRMA) (http://irma-project.org) framework[16], we aimed to define a unified database structure and coding scheme for mammography that is associated with diagnostic information, and use this reference to develop and evaluate a CBIR system called MammoSVx, where singular value decomposition (SVD) and a support vector machine (SVM) are used for breast density characterization and retrieval, respectively. This article will contribute to a reliable and large reference database, and the combination and parameterization of SVD and SVM for automatic breast density classification.

## MATERIALS AND METHODS

The MammoSVx system was developed in several stages. In the following, we describe the composition of the reference database, which is used to respond to user queries. We also describe the feature extraction and selection process using SVD and the similarity measure based on the SVM. As part of our methodology, we describe the implementation of the system, as well as the design of the evaluation experiments.

### *IRMA reference database*

The IRMA project aims to develop and implement high-level methods for CBIR with prototypal application for medico-diagnostic tasks on radiological image archives[16]. The database for mammograms integrated to the IRMA project was developed based on the union of the DDSM, MIAS, the Lawrence Livermore National Laboratory (LLNL), and routine images from the university hospital of Rheinisch-Westfälische Technische Hochschule (RWTH) Aachen University, Aachen, Germany[15].

### *DDSM database*

The DDSM database[17] officially contains 2,479 studies (695 normal, 870 benign, and 914 cancerous cases). Each study includes two images of each breast, acquired in craniocaudal (CC) and mediolateral (ML) views that have been scanned from the film-based sources by four different scanners with a resolution between 50 and 42 microns, providing a total of 9916 radiographs. Since image coding was originally proprietary, they had to be converted to a standard file format with special software: the C source code provided at the DDSM web page needed extensions to cope with endianness, palettes, and others[15]. For all cases, ground truth is provided in additional ACSII text files including the BI-RADS tissue type classification and type as well as resolution of the scanner used to digitize the film-based mammograms.

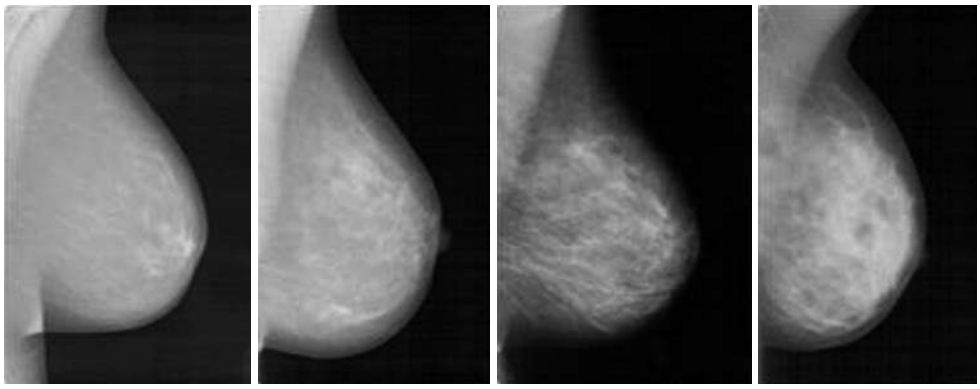

1124-410-620-d10 1124-410-620-e10 1124-410-620-f10 1124-410-620-g10

**Figure 1 Mammograms of different breast tissues.** From left to right: BI-RADS Ⅰ to BI-RADS Ⅳ. Corresponding Image Retrieval in Medical Applications (IRMA) codes are given below the images.

### *MIAS database*

The MIAS database[18] contains only 322 mammograms, all of which were acquired in the ML view. Initially scanned from film with a resolution of 50 microns, all images were reduced to 200 microns and clipped/padded so that they fit into a 1024 × 1024 bounding box. The image files are available in the portable network graphics (PNG) format and annotated with the following details: a database reference number indicating left and right breast, character of background tissue, pathology, class of lesion present and coordinates as well as size of these lesions.

### *LLNL database*

The LLNL database[19] contains a total of 197 mammograms that have been digitized at 35 microns per pixel. The images are stored in the image cytometry standard (ICS) format and had to be converted to a standard file format with a program provided as source code. For 190 images, there is a plain text file containing patient status, biopsy results and ground truth comments.

### *RWTH dataset*

In order to evaluate the extensibility of mammogram reference resources, 170 cases were extracted arbitrarily from the picture archiving and communication system (PACS) at the Department of Diagnostic Radiology, University Hospital, RWTH Aachen University, Aachen, Germany. These images were acquired digitally using a General Electric Senographe operating with low beam energy about 26 to 32 kV and with a phosphor storage system from Fuji/Philips capable of recording 7 lp/mm (approx 70 microns). The cassette was read using a Philips PCR Eleva CosimaX. Where available, a free text diagnosis in German describing the breast examination, pathology, type of tissue and lesion was included along with the digital imaging and communications in medicine (DICOM) files.

### *Integration*

To uniformly integrate all data into the IRMA system, the IRMA code[20] was extended for mammography, and based on the meta-information available with all the databases, all images were coded consistently according to the mono-hierarchical, multi-axial IRMA ontology[15]. In particular, there are four axes, each having three to four hierarchical positions, which describe: (1) technique: The imaging modality axis of the coding scheme is used to differ direct digital and secondarily digitized imaging and their resolution; (2) direction: The body orientation axis captures the CC and ML views; (3) anatomy: The body region examined axis holds information on the left and right breast; and (4) biosystem: The biological system examined provides three positions that code the tissue density according to the ACR classes, the tumor staging according to BI-RADS[3], and the type of lesion, i.e. micro or macro calcification, speckled or circumscribed masses, architectural distortions, and asymmetry.

### *Breast density characterization*

In machine vision, an image is represented numerically by a so-called feature vector (also referred to as signature), preferentially at a low-dimensional space in which the most relevant visual aspects are emphasized[21,22]. Visually, breasts of fatty and dense tissues differ through gray level intensities (Figure 1). Since texture contains information about the spatial distribution of gray levels and variations in brightness, its use for breast density assessment becomes appropriate[23]. However, the high dimensionality of a feature vector that represents texture attributes limits its computational efficiency, so it is desirable to choose a technique that combines the representation of texture with the reduction of dimensionality, in such a way as to make the retrieval algorithm more effective and computationally treatable.

SVD may satisfy these requirements representing the structure of the original data on a new basis in which the variables are ordered from the largest to the smallest degree of explained variation[24,25]. Wang *et al*[26] proposed a method of classification based on neural networks, in which the features used are the singular values of face images. For face photography recognition, the relevant technical properties of SVD are (1) stability (if a small disturbance is inserted in the image, the singular values

alter only slightly); (2) algebraic properties, and; and (3) invariance of an image by the singular values.

Singular values represent important attributes of a matrix. As images can be observed as matrices, the singular values can serve as important features for evaluation of similarity. Also aiming to reduce the dimensionality and characterizing images in a medical CBIR system, Chen *et al*[27] applied SVD to represent color images of the stomach. SVD was performed on the color histograms to form a new feature vector. Concluding their study, the authors indicated the need for further studies to determine the optimal parameterization.

In general, let A be an $m \times n$ signature representing an image. Then, SVD is expressed as: $A = UWV^T$ (1). where U and V are orthogonal matrices, $W = diag(\lambda_1, \lambda_2, \ldots, \lambda_k)$ and is the matrix of singular values of A with $\lambda_1 \geqslant \lambda_2 \geqslant \ldots \geqslant \lambda_k \geqslant 0$ and $k$ is the rank of A. For purposes of dimensionality reduction, suppose that matrix $U_k$ of size $m \times k$ is composed of the first $k$ leftmost singular vectors of U, matrix $V_k$ of size $n \times k$ is composed of the first $k$ rightmost singular vectors of V and the diagonal matrix $W_k$ of size $k \times k$ is composed of the $k$ singular values. Matrix $A_k$ is defined as follows: $A_k = U_k W_k V^T_k$ (2). The parameter $k$ is crucial[27]. The smaller the value of $k$, the less storage and processing load is required, but if $k$ is too small, important visual information is disregarded by the signature and retrieval results will become worse. In our study, $k$ is determined by systematic experiments (see Experiments).

### Similarity of signatures

The support vector machine (SVM) method was initially developed to solve binary classification problems[28]. It guides the construction of classifiers with a good degree of generalization[29], i.e. with the ability of correctly predicting the class of a sample that was not used in the learning process. The use of SVM was extended to CBIR systems[30], where the similarity between images is measured by the relevance of an image to a particular query[31]. For instance, Yang *et al*[32] have used SVM specifically for CBIR of mammograms. However, SVM requires adjustments when applied to more than two classes, such as the four BI-RADS codes used for breast density classification.

Machine learning techniques may employ an inference principle called induction. The general conclusions are obtained from a particular set of examples[22]. In supervised learning, an external agent is used to indicate the desired answers to the entry patterns. The classifier is trained with a broad set of labeled data. Given a set of labeled examples as $(x_i,y_i)$, where $x_i$ represents an example and $y_i$ denotes its label, one should be able to produce a classifier that can precisely predict the label of the new data. This induction process of a classifier from a sample of data is called training. The obtained classifier may also be seen as a function $f$ that receives a dataset $x$ and associated labels $y$. The labels or classes represent the phenomenon of interest on which one wants to make predictions. The labels can assume discrete values 1, …, $p$. A classification problem with $p = 2$ is called binary.

For a binary classification, SVM can be described as follows: given two classes and a set of points that belong to these classes, the SVM classifier determines the hyperplane in the feature space that separates the points in order to place the highest number of points of the same class on the same side, while maximizing the distance of each class to that hyperplane. The hyperplane is determined by a subset of items from the two classes, called support vectors. In most cases, however, the data set cannot be precisely separated by a hyperplane, so a kernel function is used instead. It receives two points $x_i$ and $x_j$ from the input space and computes the product between these data in the feature space. The most commonly used kernels are polynomial and Gaussian, in which the parameters must be empirically adjusted.

For more than two classes, this problem turns into a multi-class problem[33,34], which is the case of the MammoSVx system that works with four classes corresponding to the four BI-RADS categories for breast density.

There are two basic approaches for a multi-class application: (1) one-against-all: A SVM is built for each class through the discrimination of this class against the remaining classes. Successively, i.e. class by class, the decision is made. Let C denote the number of classes (here, C = 4). Then, the number of SVMs used is $M = C$-1. Hence, the MammoSVx system yields $M = 3$. Test data $x$ is classified using a decision strategy, i.e. the class with the maximum value of the discriminant function $f(x)$ is assigned to that data. All the $n$ training examples are used to construct the SVM for one class. The SVM for one class $p$ is built using the set of training data $(x)$ and the desired outputs $(y)$; (2) one-against-one: A SVM is built for a pair of classes through its training in the discrimination of two classes. In this way, the number of SVMs used in the method is $M = (C\text{-}1)(C\text{-}2)/2 = 3$. Here, one SVM for a pair of classes $(p,m)$ is built using training examples belonging to only these two classes. This approach is a kind of generalization of the binary classification to more than two classes. Advantageously, all training examples are used at the same time[33].

With respect to the four BI-RADS tissue classes, both methods require three SVMs. In order to optimize the training phase providing all the data, we apply the one-against-one method to separate the four BI-RADS categories, two by two, for all experiments.

### Implementation

The MammoSVx system was implemented using MatLab (Matrix Laboratory), using the image processing and symbolic math toolboxes, and the LSSVM library[35]. It was executed on an Intel Core 2 Duo 2GHz processor with 3GB of RAM under the Microsoft Windows operating system.

The IRMA system is implemented in C and operated on a common Linux/Unix system. The PostgreSQL database is used to manage image, feature, and feature transform data[36].

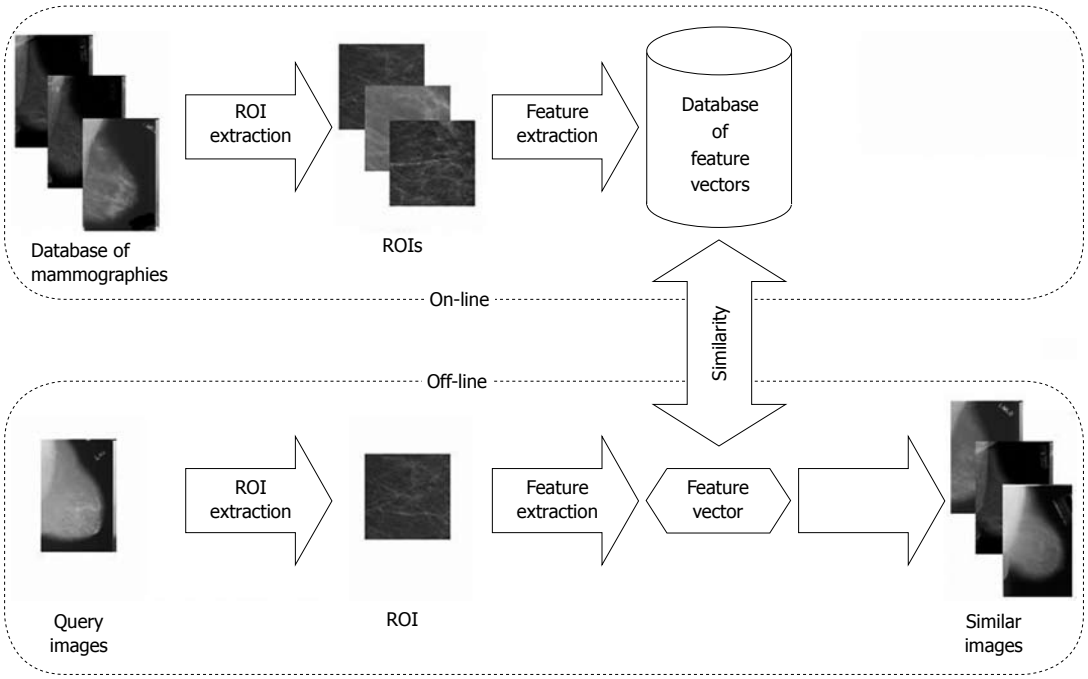


**Figure 2** Scheme of the **MammoSVx content-based image retrieval system.** From both the query image and images from the database, features are extracted and an index of similarity between these images is obtained. The most relevant images to the query are retrieved from the database and presented to the user.

Web-based access is provided by PHP hypertext preprocessor and the Smarty template engine (http://www.smarty.net)[37].

The methodologies were fused to MammoSVx (Figure 2). To remove noise, examination labels and other annotations from all images, regions of interest (ROI) were extracted. In a first step, a standardized image size was obtained shrinking all mammograms into a format of 1024 × $Z$ pixels, where $Z$ varies according to the aspect ratios of the radiographs between 300 and 800 pixels. In this step, linear interpolation is applied. In the resulting scale, the size of the ROI that was extracted automatically was set to 300 × 300 pixels, which ensures the ROI contains tissue pattern only. Thereafter, the textural features were extracted using the SVD method, and compared to the features in the IRMA reference database using the SVM method.

## *Experiments*

**Selection of image data:** The IRMA database was merged from data of different sources and provides a reliable base for parameterization and evaluation of CBIR and CAD applications. Using the IRMA code, groups of reference images can be easily formed. As a result, the data used in the experiments were uniformly mixed from directly digital acquired and secondarily digitized mammograms of the left or right breast in CC or ML views with and without pathological alteration. However, the frequency of occurrence of tissue type in the IRMA database differs. To ensure an equal distribution for classification experiments, all images from the least frequent BI-RADS class are used, and the same amount is taken arbitrarily from the other classes.

**Extraction of features:** SVD was performed for all selected mammograms. The first $k$ singular values were kept for the composition of the feature vector. The values for $k$ used in the experiments were 25, 50, 100, 150 and 200. These values were chosen empirically in accordance with Elden and Andrews[25,38]. Optionally, SVD features were combined with the gray level histogram, as histograms have been successfully used in previous work[12,13,39]. In addition, we analyze the impact of the gray level histograms using this information solely for retrieval.

**Evaluation of MammoSVx for CBIR:** The CBIR task keeps the physician in the loop. Usually, the user presents an image, and the system offers a set of, for instance, ten responses, visually displayed to the physician, who can select appropriate information from the responses, or refine the query.

For the evaluation of the CBIR system, measures of precision and recall were obtained based on the top 10 retrieved images. Precision is the ratio of the number of relevant images retrieved to the total number of irrelevant and relevant images, whereas recall is the ratio of the number of relevant images retrieved to the total number of relevant images in the database[40]. Both measures are usually expressed as a percentage. We apply 5-fold cross validation and variance analysis (ANOVA) to obtain the best configuration of MammoSVx.

**Evaluation of MammoSVx as a classifier:** Furthermore, one can think of using the MammoSVx system as an automatic classifier. In this setting, the physician is excluded from the loop, and the system is used for automatic decision making. There are several ways of combining the

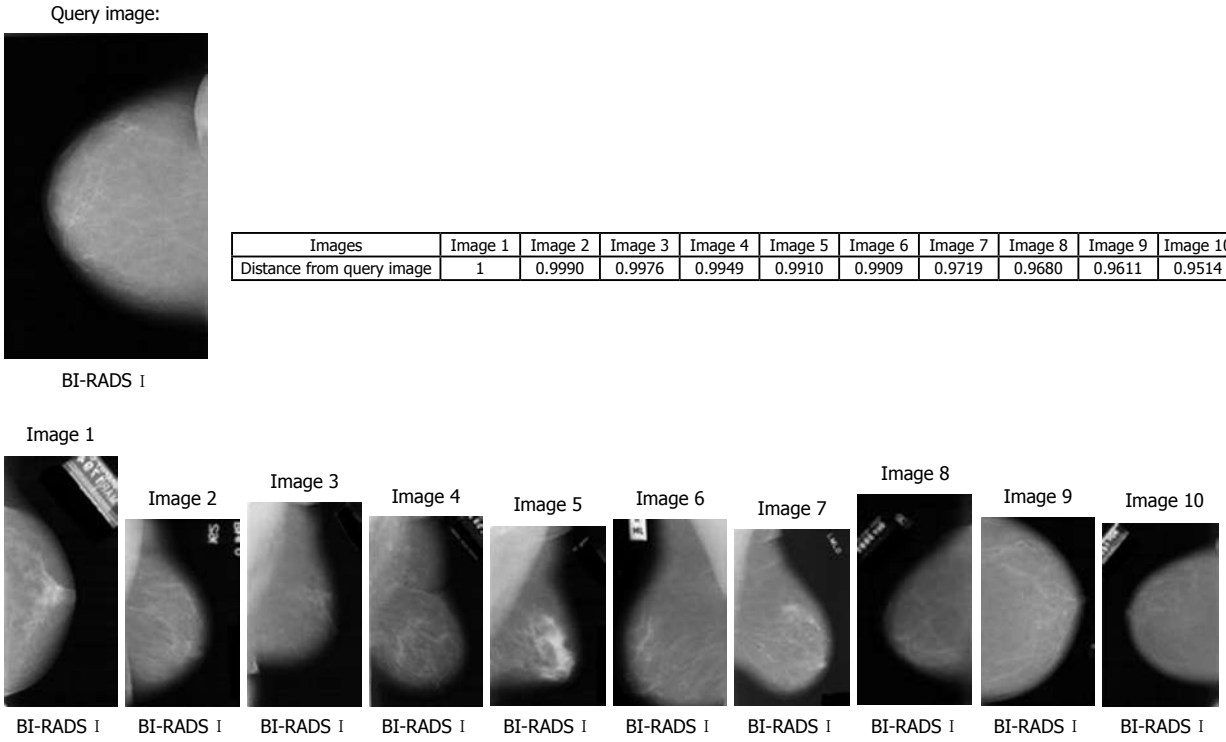


| Images | Image 1 | Image 2 | Image 3 | Image 4 | Image 5 | Image 6 | Image 7 | Image 8 | Image 9 | Image 10 |
|---|---|---|---|---|---|---|---|---|---|---|
| Distance from query image | 1 | 0.9990 | 0.9976 | 0.9949 | 0.9910 | 0.9909 | 0.9719 | 0.9680 | 0.9611 | 0.9514 |

**Figure 3 Retrieval example of the MammoSVx system.** The retrieval is based on breast density, with $k$ = 25 as parameter for singular value decomposition (SVD) and support vector machine (SVM) using the polynomial kernel.

**Table 1 Parameters of the kernels of the support vector machine model**

| Parameters | Polynomial kernel | Radial kernel |
|---|---|---|
| Cost (C) | 10 | 1 |
| Gamma (g) | 0.00022 | 0.0055 |
| Epsilon (e) | 0.1 | 0.1 |
| Degree | 2 | - |

ground truth of a set of retrieved images and forming a decision. The easiest, but usually not the best way, is to return only one image, and simply decide whether it is from the correct class or not. In doing so, the obtained results can be best compared with others.

Hence, this evaluation was performed measuring the accuracy, which is the percentage of correctly classified images of a certain class over the ground truth of the total mammograms in that class. For this experiment, we apply 10-fold cross validation.

## RESULTS

### Reference database

Based on international standards such as ACR and BI-RADS, we provided a scheme to integrate available mammogram databases using a standardized description of imaging modality and resolution, orientation and view, left and right position of the breast, tissue type, tumor staging and lesion description. Integrating different resources that are freely available in the Internet, our database currently holds 10 509 images from 232 different code classes.

BI-RADS tissue class Ⅱ was found to be most common with about 4000 entries, and BI-RADS class I was at least represented with only 1256 images. According to the protocol defined in the previous section, 1256 radiographs were randomly selected from all the groups yielding a total of 5024 mammograms.

### Feature extraction

Table 1 shows the resulting parameterization of the SVM with polynomial, radial, and linear kernels. Depending on the kernel, $k$ = 25, $k$ = 100, and $k$ = 200 performed best, respectively. Therefore, the polynomial SVM kernel was superior since it needed the least number of data. Table 2 shows the overall results. In general, the combination of SVD and gray level histogram outperformed SVD and histogram feature extraction.

### Evaluation of MammoSVx

The best average precision of 82.14%, 71.75%, and 76.87% was obtained using the polynomial, radial, and linear kernel functions, respectively (Table 2). The ANOVA variance analysis yielded statistical significance. In order to verify the number of singular values that really represent breast density, the trace of the matrix $A_k$ of singular values was examined. The last column in Table 2 shows the average amount of variables that are represented by the $k$ singular values. The diagonal matrix has $k$ singular values that are significantly larger than the others, and the zero singular values usually appear as small numbers. For all different values of $k$, only 24 singular values really represented breast density, and so the other values could be

**Table 2 Average precision results of the MammoSVx system**

| k | Feature | Average precision (mean ± SD, %) | | | Trace of Ak |
|---|---|---|---|---|---|
| | | Polynomial | Radial | Linear | |
| 25 | SVD | 79.42 ± 0.44 | 68.92 ± 0.05 | 75.36 ± 0.10 | 23 |
| | SVD + histogram | 82.14 ± 0.30 | 70.48 ± 0.12 | 75.66 ± 0.01 | |
| 50 | SVD | 76.61 ± 0.40 | 71.00 ± 0.09 | 75.12 ± 0.07 | 24 |
| | SVD + histogram | 76.72 ± 0.50 | 71.47 ± 0.16 | 76.26 ± 0.04 | |
| 100 | SVD | 77.91 ± 0.15 | 69.23 ± 0.16 | 75.32 ± 0.06 | 24 |
| | SVD + histogram | 78.31 ± 0.14 | 71.75 ± 0.04 | 75.70 ± 0.18 | |
| 150 | SVD | 76.85 ± 0.16 | 71.52 ± 0.06 | 74.41 ± 0.14 | 25 |
| | SVD + histogram | 76.47 ± 0.20 | 68.76 ± 0.17 | 76.44 ± 0.16 | |
| 200 | SVD | 75.69 ± 0.16 | 71.57 ± 0.06 | 74.80 ± 0.08 | 26 |
| | SVD + histogram | 76.67 ± 0.23 | 70.87 ± 0.16 | 76.87 ± 0.04 | |
| | Histogram only | 50.00 | 50.00 | 67.80 | |

SVD: Singular value decomposition.

considered irrelevant. In conclusion, $k = 25$ appropriately represented breast texture in a lower-dimensional space with maximized computational savings, and the polynomial kernel significantly outperformed the other configurations.

Figure 3 represents an example of the MamoSVx system, with a query image of BI-RADS category I for breast density. All the top ten retrieved images are from the same category of breast density of the query image. In this experiment, the system was not designed to differentiate the projection (CC or MLO) as only a ROI was selected for characterization, which does not consider the pectoral muscle (signature of the MLO projection). Also, the distance of these retrieved images to the query image is presented, where images with distance values near 1.0 are closer to the query image. Time of retrieval was 3.85 s.

Considering the classification experiment, an average accuracy rate of 76.4% was obtained.

## DISCUSSION

We have presented a system design for CBIR for breast tissue density classification, which can be used directly to assist radiologists or as a preprocessing stage in CAD applications for lesion detection and tumor staging.

The evaluation of MammoSVx was based on a large database merged from a variety of sources, which supports the generalization of the experimental results. Furthermore, we were able to improve previously published results. For instance, Bovis and Singh[14] reported an average recognition rate of 71.4%, calculated on 377 images only, which is clearly below the corresponding finding in our experiment (76.4% obtained from 5,024 mammograms). This improvement was obtained by combining SVD with the gray scale histogram distribution. In other words, the chosen signature characterized breast density well. Furthermore, the small standard deviations obtained within the cross-over design (Table 2) indicate that our reference database was of sufficient size for the given problem.

An important characteristic of the MammoSVx CBIR system is the use of a priori breast density classification, as all the images contained in the IRMA database have their ground truth already set by an experienced radiologist. This supports the physician visually, as can be seen in Figure 3. Although radiologists might look further for breast lesions such as masses and calcifications in mammograms, a CBIR system for mammograms should include all possibilities. Therefore, MammoSVx may form the first stage of a CAD system, as breast density plays an important role in the diagnostic process.

Future work may focus on tests with more images and the combination of breast density, view and lesion as a pattern for retrieval. In addition, a weight combination of features should be tested in an attempt to avoid non-relevant images in the results.

## COMMENTS

### *Background*

Systems assisting radiologists in lesion detection and classification, or just presenting similar images to a sketched query are of great importance in clinical practice. They impact case-based reasoning, evidence-based medicine, and advanced blended learning techniques.

### *Research frontiers*

In screening mammography, the compilation of a large data collection with reliable ground truth is important to compile reliable systems for computer-aided diagnosis. Automatic detection of BI-RADS categories for breast tissue has not yet been solved, although several works on this topic has been published.

### *Innovations and breakthroughs*

We provide a content-based image retrieval approach that relies on a large compilation of ground truth data in mammography. For computer-assisted diagnosis, breast tissue patterns are represented using a few singular values and a support vector machine for classification.

### *Applications*

The Image Retrieval in Medical Applications framework provides server and client components to interface computer-aided diagnosis in routine clinical practice. A sample application is provided.

### *Peer review*

The topic is well presented and the article is reasonable. Some corrections need to be made, especially in the experimental section to improve the clarity.

## REFERENCES

1 **Xue F**, Michels KB. Intrauterine factors and risk of breast cancer: a systematic review and meta-analysis of current evidence. *Lancet Oncology* 2007; **8**: 1088-1100

2 **Wolfe JN**. Breast patterns as an index of risk for developing breast cancer. *AJR Am J Roentgenol* 1976; **126**: 1130-1137
3 American College of Radiology – Breast Imaging Reporting and Data System (BI-RADS). Atlas 2006.
4 **del Bimbo A**. Visual information retrieval. San Francisco: Morgan Kaufmann Publishers Inc., 1999
5 **Doi K**. Computer-aided diagnosis in medical imaging: historical review, current status and future potential. *Comput Med Imaging Graph* 2007; **31**: 198-211
6 **Rangayyan RM**, Ayres FJ, Desautels JEL. A review of computer-aided diagnosis of breast cancer: Toward the detection of subtle signs. *J Franklin Inst* 2007; **344**: 312-348
7 **Tagare HD**, Jaffe CC, Duncan J. Medical image databases: a content-based retrieval approach. *J Am Med Inform Assoc* 1997; **4**: 184-198
8 **Müller H**, Michoux N, Bandon D, Geissbuhler A. A review of content-based image retrieval systems in medical applications-clinical benefits and future directions. *Int J Med Inform* 2004; **73**: 1-23
9 **Lehmann TM**, Güld MO, Deselaers T, Keysers D, Schubert H, Spitzer K, Ney H, Wein BB. Automatic categorization of medical images for content-based retrieval and data mining. *Comput Med Imaging Graph* 2005; **29**: 143-155
10 **Baeza-Yates R**, Ribeiro-Neto B. Modern information retrieval. Addison-Wesley Professinal, 1999
11 **Castella C**, Kinkel K, Eckstein MP, Sottas PE, Verdun FR, Bochud FO. Semiautomatic mammographic parenchymal patterns classification using multiple statistical features. *Acad Radiol* 2007; **14**: 1486-1499
12 **Sheshadri HS**, Kandaswamy A. Breast tissue classification using statistical feature extraction of mammograms. *Med Imag Inform Sci* 2006; **23**: 105-107
13 **Wang XH**, Good WF, Chapman BE, Chang YH, Poller WR, Chang TS, Hardesty LA. Automated assessment of the composition of breast tissue revealed on tissue-thickness-corrected mammography. *AJR Am J Roentgenol* 2003; **180**: 257-262
14 **Bovis K**, Singh S. Classification of mammographic breast density using a combined classifier paradigm. Medical Image Understanding and Analysis (MIUA) Conference, Portsmouth, 2002
15 **de Oliveira JEE**, Güld M, de Albuquerque Araújo A, Ott B, Deserno T. Towards a standard reference database for computer-aided mammography. Proceedings of SPIE Medical Imaging, volume 6915. 2008: 69151Y
16 **Lehmann TM**, Güld MO, Thies C, Fischer B, Spitzer K, Keysers D, Ney H, Kohnen M, Schubert H, Wein BB. Content-based image retrieval in medical applications. *Methods Inf Med* 2004; **43**: 354-361
17 **Heath M**, Bowyer KW, Kopans D, Moore R, Kegelmeyer P. Current status of the digital database for screening mammography. In: Digital mammography. Dordrecht: Kluwer Academic Publishers, 1998: 457-460
18 **Suckling J**. The mammographic image analysis society digital datagram database. *Exerpta Medica International Congress Series* 1994; **1069**: 375-378
19 **Center for Health Care Technologies Livermore**. Lawrence Livermore National Library/UCSF Digital Mammogram Database. Livermore, CA, 1995
20 **Lehmann TM**, Schubert H, Keysers D, Kohnen M, Wein BB. The IRMA code for unique classification of medical images. Proc SPIE 2003; 5033: 440-451
21 **Castelli V**, Bergman LD. Image databases: search and retrieval of digital imagery. New York: Wiley-Interscience, 2001
22 **Duda RO**, Hart PE, Stork DG. Pattern classification. New York: John Wiley & Sons, 2001
23 **Gonzalez RC**, Woods RE, Eddins SL. Digital image processing using MATLAB. New Jersey: Prentice-Hall, 2003
24 **Golub GH**. Matrix computations. Johns Hopkins series in the matematicals sciences, 1983
25 **Eldén L**. Numerical linear algebra in data mining. *Acta Numerica* 2006; **15**: 327-384
26 **Wang Y**, Tan T, Zhu Y. Face verification based on singular value decomposition and radial basis function neural network. Proceedings of Asian Conference on Computer Vision. Taipei, Taiwan; 2000
27 **Chen Q**, Tai X, Dong Y, Pan S, Wang X, Yin C. Medical image retrieval based on semantic of neighborhood color moment histogram. In: The 2nd International Conference on Bioinformatics and Biomedical Engineering, 2008: 2221-2224
28 **Akay MF**. Support vector machines combined with feature selection for breast cancer diagnosis. *Expert Syst Appl* 2009; **36**: 3240-3247
29 **Vapnik VN**. The nature of statistical learning theory. New York: Springer-Verlag, 1995
30 **Wong WT**, Hsu SH. Application of SVM and ANN for image retrieval. *Eur J Oper Res* 2006; **173**: 938-950
31 **van Rijsbergen CJ**. Information retrieval. London: Butterworth & Co, 1979
32 **Yang Y**, Wei L, Nishikawa RM. Microcalcification classification assisted by content-based image retrieval for breast cancer diagnosis. In: IEEE International Conference on Image Processing, 2007: 1-4
33 **Crammer K**, Singer Y. On the learnability and design of output codes for multiclass problems. Computational Learning Theory 2000; 35-46
34 **Hsu CW**, Lin CJ. A comparison of methods for multiclass support vector machines. *IEEE Trans Neural Netw* 2002; **13**: 415-425
35 **Suykens JAK**, Gestel TV, Brabanter JD, Moor BD, Vandewalle J. Least squares support vector machines. Singapore: World Scientific, 2002
36 **Güld MO**, Thies C, Fischer B, Lehmann TM. A generic concept for the implementation of medical image retrieval systems. *Int J Med Inform* 2007; **76**: 252-259
37 **Deserno TM**, Güld MO, Plodowski B, Spitzer K, Wein BB, Schubert H, Ney H, Seidl T. Extended query refinement for medical image retrieval. *J Digit Imaging* 2008; **21**: 280-289
38 **Andrews H**, Patterson C. Singular value decompositions and digital image processing. *IEEE Trans Acoust Speech Signal Process* 1976; **24**: 26-53
39 **Kinoshita SK**, de Azevedo-Marques PM, Pereira RR Jr, Rodrigues JA, Rangayyan RM. Content-based retrieval of mammograms using visual features related to breast density patterns. *J Digit Imaging* 2007; **20**: 172-190
40 **Davis J**, Goadrich M. The relationship between precision-recall and roc curves. In: ICML '06: Proceedings of the 23rd international conference on Machine learning. New York, NY: ACM, 2006: 233-240


**S- Editor** Cheng JX **L- Editor** Webster JR **E- Editor** Zheng XM

World Journal of Radiology

Online Submissions: http://www.wjgnet.com/1949-8470office
wjr@wjgnet.com
doi:10.4329/wjr.v3.i1.32

*World J Radiol* 2011 January 28; 3(1): 32-37
ISSN 1949-8470 (online)
© 2011 Baishideng. All rights reserved.

CASE REPORT

# Breast and lung metastasis from pancreatic neuroendocrine carcinoma

Shevonne Satahoo-Dawes, Joshua Palmer, Eddie W Manning III, Joe Levi

Shevonne Satahoo-Dawes, Joshua Palmer, Eddie W Manning III, Joe Levi, DeWitt Daughtry Family Department of Surgery, Jackson Memorial Hospital, University of Miami Miller School of Medicine, Miami, FL 33136, United States
Author contributions: Satahoo-Dawes S and Palmer J performed the literature search; Satahoo-Dawes S, Palmer J and Manning III EW analyzed the literature and wrote the manuscript; Levi J and Manning III EW performed the surgery, collected the photographs and coordinated the study.
Correspondence to: Eddie W Manning III, MD, DeWitt Daughtry Family Department of Surgery, Jackson Memorial Hospital, University of Miami Miller School of Medicine, Miami, FL 33136, United States. emanning@med.miami.edu
Telephone: +1-305-5851280 Fax: +1-305-5856043
Received: March 31, 2010 Revised: December 7, 2010
Accepted: December 14, 2010
Published online: January 28, 2011

## Abstract

Pancreatic neuroendocrine tumors (PNETs) are an uncommon malignancy, accounting for a small percentage of all pancreatic malignancies. Due to their insidious course, most PNETs present with metastatic disease. Although reports in the literature describe PNET metastasis to the liver, lung and brain, to date there are no reports of stage Ⅳ disease involving the breast. Moreover, the lack of consensus regarding classification and treatment of this entity leaves practitioners without standards of practice or a firm base from which to formulate prognosis. In this report, the case of a previously healthy 51-year-old woman with stage Ⅳ PNET is examined. After combined neoadjuvant therapy with 5-fluorouracil, carboplatin, etoposide and radiation, surgical resection revealed metastatic PNET to the breast and lung, with no microscopic evidence of residual disease within the pancreas. An extensive analysis of the presentation, diagnosis, imaging modalities, treatment options, and prognosis is included in the discussion. As demonstrated by our review, there is a need for further studies to delineate inconclusive evidence with respect to subtype classification, treatment and prognosis of PNETs.

© 2011 Baishideng. All rights reserved.

**Key words:** Neuroendocrine tumor; Metastatic tumor; Pancreatic tumor; Breast; Lung

**Peer reviewer:** Ian C Roberts-Thomson, Professor, Department of Gastroenterology and Hepatology, The Queen Elizabeth Hospital, 28 Woodville Road, Woodville South, 5011, Australia

Satahoo-Dawes S, Palmer J, Manning III EW, Levi J. Breast and lung metastasis from pancreatic neuroendocrine carcinoma. *World J Radiol* 2011; 3(1): 32-37 Available from: URL: http://www.wjgnet.com/1949-8470/full/v3/i1/32.htm DOI: http://dx.doi.org/10.4329/wjr.v3.i1.32

## INTRODUCTION

Neuroendocrine cells are widely distributed throughout the body. Common sites include the lung, gastrointestinal tract, adrenal gland and thyroid gland; any of which may give rise to malignant neoplasms. Pancreatic neuroendocrine tumors (PNETs) are thought to develop from embryonic neural crest cells[1] that later give rise to islet cell tissue. It is believed that these cells belong to the amine precursor uptake decarboxylase system[2-4]. PNETs are an uncommon malignancy, accounting for 1%-5% of all pancreatic malignancies[4-8]. The estimated incidence is 1-5 cases per million[5,7,9]. However, incidence rates of 1-1.5 cases per 100 000 population have been reported[8,10]. Abood *et al*[4] and You *et al*[8] have reported approximately 2500 cases per year in the United States, with a peak age of 30-60 years, and no gender preference. PNETs are classified as functioning or non-functioning depending on the presence of clinical manifestations secondary to

increased hormonal secretion, with multiple hormones being common[11]. Non-functioning PNETs are the result of tumors that either produce inert hormones or subclinical concentrations of active hormones without symptoms. Non-functioning PNETs account for 15%-52% of all pancreatic endocrine tumors[2,4,6,7,12-14].

In 2000, the World Health Organization (WHO) classified gastroenteropancreatic neuroendocrine tumors based on histological and pathological characteristics into well-differentiated, poorly differentiated, and mixed endocrine-exocrine subtypes[2,15]. Other classifications grade PNETs based on behavior as low, intermediate, or high grade lesions[2,16]. Histologically, PNETs show features similar to small cell carcinoma of the lung, lymphoma, and neuroendocrine tumors of the stomach and colon. PNETs have a more indolent course than the more common pancreatic adenocarcinoma with a longer survival, although 50%-75% present with metastatic disease[2,4,6,9]. Common PNET metastases occur in lymph nodes, liver, spleen, and bone at 50%, 30%, 10% and 7%, respectively[17]. Solorzano *et al*[18] have described metastasis to lung and brain as well. The malignancy rate is often > 50%[2,4,7,9,19], with a mean survival of 6-8 years even in widely metastatic disease[2,10].

A literature search of Medline and Embase has revealed no cases of PNETs metastatic to the breast. Thus, the present case broadens the discussion because it describes the clinical course of a 51-year-old woman with a poorly differentiated pancreatic neuroendocrine carcinoma metastatic to the breast and lung. Additionally, this case illustrates the successful management of stage IV disease with neoadjuvant chemotherapy and radiotherapy, followed by radical surgical resection. The benefit of combined, aggressive medical and surgical management is highlighted, as well as an interesting parallel to the management of metastatic liver disease.

## CASE REPORT

A previously healthy 51-year-old, Caucasian woman presented to her primary care physician with a 1-wk history of bloating and right abdominal discomfort, with radiation to the back. Initial imaging by abdominal ultrasound showed a pancreatic head mass with associated biliary dilatation, which was highly suspicious for primary pancreatic carcinoma. Further assessment by computed tomography (CT) revealed a 5 cm × 5 cm well-circumscribed pancreatic head lesion in the c-loop of the duodenum, which appeared to have a well-circumscribed edge or capsule. Of note, the lesion was not clearly cystic and had solid heterogeneous enhancement. Initial laboratory tests were significant for elevated amylase and lipase (598 IU/L and 1802 IU/L, respectively), along with elevated aspartate aminotransferase, alanine aminotransferase and alkaline phosphatase (86 IU/L, 129 IU/L and 334 IU/L, respectively) and elevated total bilirubin at 2.9 mg/dL, despite normal prothrombin and partial thromboplastin time. Tumor markers at the time were significant for elevated visceral cancer markers: carbohydrate antigen (CA) 19-9 (81 IU/mL) and CA 125 (39 IU/mL). CA 27.29 and carcinoembryonic antigen (CEA) were within normal limits.

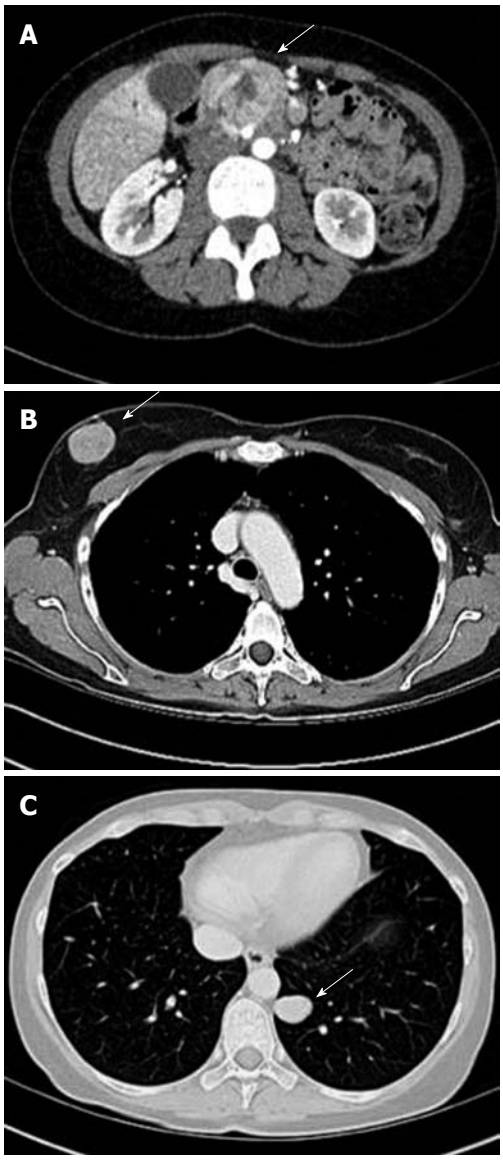


**Figure 1 Preoperative computed tomography scans of the chest, abdomen and pelvis.** A: Pancreatic mass with associated biliary dilatation; B: Large, well-circumscribed, right breast lesion; C: Small left lung lesion. Postoperative pathology revealed a poorly differentiated carcinoma with clear cell features, favoring a poorly differentiated neuroendocrine carcinoma in the right breast and left lower lobe of the lung. The arrows depict the lesion of reference.

During the work-up of the pancreatic mass, the patient developed a stabbing breast pain and a new lump in the right breast. A diagnostic mammogram showed a new lobular mass in the right breast that was not present a year before. Positron emission tomography (PET)/CT was done to stage the disease process. There was abnormal activity corresponding to a large, ill-defined mass in the head of the pancreas, as well as within a 2.7-cm nodule in the left lower lobe of the lung and a 2.5-cm nodule in the superior aspect of the right breast (Figure 1). Both the lung and breast lesions were suspected to be metastatic nodules from the primary pancreatic mass. With these findings, stage IV carcinoma was diagnosed.

One month after the onset of symptoms, the patient underwent endoscopic retrograde cholangiopancreatography with stent placement to improve biliary obstruction. During the procedure, a single 40-mm region of stenosis was noted in the distal third of the main duct, with diffuse dilation in the middle third. Pancreatic biopsy revealed cellular evidence of poorly differentiated carcinoma, with non-contributory immunostaining. In addition, a right breast core biopsy demonstrated poorly differentiated carcinoma. Subsequent immunostaining for CD10 and epithelial membrane antigen (EMA) was positive, with stains for RCA and ER being negative. As such, the breast mass was considered to be immunohistochemically consistent with metastatic renal cell carcinoma. This pathology was later reviewed at an outside facility and described as a well-differentiated endocrine neoplasm with clear cell features. There was no prior clinical or radiographic evidence of renal involvement, therefore, renal cell carcinoma was unlikely. An octreotide scan, done 2 mo after the biopsy, was positive for uptake in the large pancreatic mass and right breast lesion. Given the results of this scan, a diagnosis of neuroendocrine carcinoma was favored by the consultant pathologist.

Shortly after the octreotide scan, the patient developed life-threatening gastrointestinal hemorrhage as the pancreatic tumor eroded into the duodenum. She subsequently underwent angiography and embolization of branched tumor vessels of the celiac, gastroduodenal and superior mesenteric arteries. She developed diarrhea and was started on 5-fluorouracil (5-FU) and octreotide (Sandostatin), for its postulated symptomatic relief and antitumor effect. She remained on Sandostatin LAR 30 mg once monthly for 6 mo. In an attempt to reduce tumor size, neoadjuvant chemotherapy and radiation were initiated. She underwent radiation for 3 mo and received three cycles of 5-FU followed by three cycles of carboplatin and etoposide (Appendix A). Bone marrow stimulation was administered *via* a combination of filgrastim, pegfilgrastim and darbepoetin alfa.

Surveillance CT scans were obtained at 5 mo post-presentation and again at 7 mo, just 3 wk before her first operation. During this 2-mo interval, there was progression of the right breast mass from 2.5 cm at presentation to 4.1 cm at 5 mo and 4.5 cm at 7 mo. The lesion in the left lung was reduced in size from 2.7 cm at presentation to 2.1 cm and remained relatively unchanged at 2.2 cm 7 mo later. Of note, there were small bilateral pulmonary nodules seen on the second scan at 5 mo. Finally, the mass at the head of the pancreas was reduced from 5 cm at presentation to 3.4 cm 7 mo later. A benign hemangioma of the left liver lobe was also noted on her 5-mo scan, which was the only liver finding.

Her first operation was a combined robotic video-assisted thoracoscopy with mini-thoractomy, resection of anterior basilar segment of the left lower lobe of the lung, and a right breast lumpectomy. There were no known post-surgical complications. The final pathology report of the right breast mass revealed a poorly differentiated carcinoma with clear cell features with positive margins, whereas the lung segment showed poorly differentiated malignant neoplasm with spindle and clear cell features with clear margins. Both specimens were thought to favor the diagnosis of poorly differentiated neuroendocrine carcinoma. Immunohistochemical staining of both specimens revealed some variability (Table 1). However, there was enough histological similarity to consider these two lesions to be from the same primary site.

**Table 1 Immunohistochemical characterization of breast and lung lesions**

| Staining | Breast | Lung |
|---|---|---|
| NSE | Positive | Positive |
| CD 56 | Positive | Positive |
| HMB-45 | Positive | Positive |
| CD10 | Positive | Positive |
| MIB-1 | High index | High index |
| EMA | Negative | Negative |
| S-100 | Negative | Negative |
| Melan A | Negative | Negative |
| Synaptophysin | Negative | Negative |
| Chromogranin | Negative | Negative |
| AE1-3 | Weakly reactive | Negative |
| CAM 5.2 | Weakly reactive | Negative |

Three weeks later, in preparation for her Whipple procedure (pancreatoduodenectomy), she underwent another CT scan of the chest, abdomen and pelvis. Imaging demonstrated that the previously visualized pulmonary nodule in the left lower lobe was resected, with no new pulmonary nodules. The liver had a cystic lesion that was consistent with a hemangioma, but no new lesions were seen. Additionally, there was still some enlargement of the pancreatic head mass, although it was smaller compared to a prior study (now 2.9 cm from 3.4 cm). The pancreas was also atrophic from mid-body to tail with no lymphadenopathy. Laboratory tests at that time were within normal limits, demonstrating resolution of previously elevated liver enzymes, lactate dehydrogenase, serotonin, uric acid, and chromogranin A.

Nine months after presentation, the patient had a pylorus-sparing Whipple procedure and intraoperative ultrasound of the liver (Figure 2). Imaging showed a marked reduction in the size of her primary pancreatic head lesion, with atrophic body and tail. She also had a hemangioma in the left lobe of the liver and a cyst in the right lobe. The pancreatic specimen had no evidence of viable tumor, with clear margins and negative nodes.

The postoperative course was uncomplicated and the patient was discharged to home 1 wk later. One month after the operation, she is doing well and will undergo another round of chemotherapy with carboplatin and gemcitabine.

## DISCUSSION

Most PNETs are diagnosed incidentally as a part of the workup for non-specific abdominal pain or mass effect

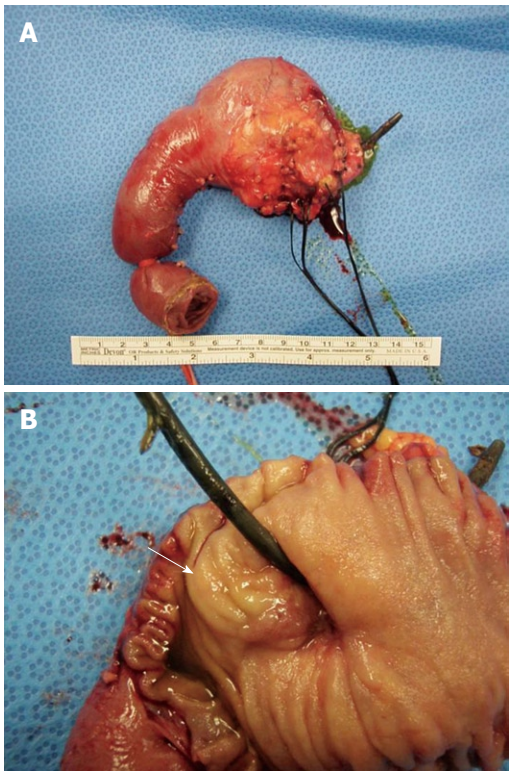


**Figure 2 Pyloric sparing Whipple gross specimen with biliary stent in place.** A: There is a marked decrease in the size of the tumor, producing an undetectable remnant lesion on gross examination; B: Small periampullary remnant lesion (arrow) noted on gross examination.

leading to biliary or bowel obstruction[4]. General presenting symptoms include abdominal pain, weight loss, palpable mass and jaundice[6,8,16]. With lesions in the head of pancreas, there can be gastrointestinal bleeding secondary to erosion in the duodenum, as well as gastric or biliary outlet obstruction[18]. The patient presented with many of these symptoms including abdominal pain, weight loss, biliary obstruction and gastrointestinal bleeding.

As initial imaging, transabdominal ultrasound may be done. It is relatively inexpensive and widely available, but has a reported sensitivity of only 9%-64%[6]. Therefore, further imaging modalities may still be necessary. CT scanning also may be done as initial imaging to localize and stage the disease. It also can be used to assess liver metastases and pancreatic lymph node involvement[9]. Magnetic resonance imaging (MRI) also is helpful to evaluate metastatic disease, and to delineate the mass in relation to the pancreatic duct and major vessels[9]. MRI has been shown to be generally effective at detecting lesions > 1 cm, with 50% effectiveness in detecting lesions between 1 and 2 cm[6]. Somatostatin receptor scintigraphy or octreotide scanning has been deemed to be the most sensitive imaging modality[4] because it can effectively localize and stage disease by detecting primary and metastatic tumors > 1 cm[4,9]. It is especially good at detecting hepatic and bone metastases; however, it provides no information about tumor size or resectability[6]. Endoscopic ultrasound allows for visualization of small tumors in the head, uncinate and body of the pancreas[9]. It has been reported to be capable of detecting lesions as small as 0.5 cm[6]. It allows for visualization of lymph nodes, with a sensitivity of 58%[9]. Additionally, it is effective at visualizing the walls of the stomach, duodenum and adjacent structures[6]. Intraoperative ultrasound is used to evaluate non-palpable tumors, as well as the ducts, vessels, duodenal wall and lymph nodes[9]. Other modalities include PET, radiolabeled imaging selective venous sampling and selective pancreatic angiography. Imaging for this patient included many of these modalities: transabdominal ultrasound as initial evaluation, CT scan for initial and follow-up imaging, octreotide scan for localization, and intraoperative ultrasound for evaluation during resection. In this particular case, there was moderate concordance among these particular imaging modalities in determining the appearance and location of the primary cancer and its metastases.

Several studies have reported a difference in tumor size based on tumor type and stage. Hochwald *et al*[16] have reported the median size of non-functioning tumors to be 4.7 cm as opposed to 1.6 cm seen in functioning tumors ($P = 0.005$). O'Grady *et al*[6] have noted similar findings of 4.0 cm for non-functioning tumors *vs* 1.9 cm for functional tumors. Additionally, You *et al*[8] have reported that the average size of malignant tumors is 3.5 cm compared to 2.5 in well-differentiated tumors ($P = 0.001$). In consideration for metastatic disease, Bruzoni *et al*[2] have reported a median size of 7.3 cm *vs* 4.7 cm in patients without metastatic disease ($P < 0.05$). Additionally, the majority of these lesions are found in the pancreatic head[4,6,9]. These dimensions are consistent with this case because our patient presented with a 5-cm mass in the head of the pancreas.

PNETs have features similar to small cell cancer of the lung, as well as neuroendocrine tumors at other sites. Immunohistochemistry can help to differentiate between these tumors. PNETs commonly have granules that contain neuron specific enolase (NSE), synaptophysin and chromogranin[4]. As such, these tumors commonly stain positive for NSE and synaptophysin, with poor expression of chromogranin, sometimes staining negative in carcinomas[11]. Lloyd has suggested that thyroid factor-1 distinguishes lung from pancreatic primary tumor, and that stains for CD45, CD20 and CD45RO can help to distinguish pancreatic tumors from lymphomas[3]. Despite being negative for synaptophysin, immunohistochemical staining of the breast and lung lesions was positive for NSE, which is consistent with a PNET.

Serum markers also can be used to detect disease and monitor its course. They are particularly helpful in monitoring disease progression, relapse and burden. Chromogranin A has been considered to be the most sensitive marker for PNETs[10]. In fact, it is elevated in 60%-100% of patients[9]. Although the exact initial level of chromogranin A is unavailable, it was reported to be elevated in our patient, as expected. Of note, after octreotide therapy, the serum chromogranin level normalized and staining of the breast and lung specimens was negative. These were

not unexpected findings because octreotide can affect the synthesis and release of chromogranin A in granules[20]. This effect on the granules could also explain the negative staining for synaptophysin. In addition to measuring these markers of PNETs, it is important to rule out other sites of primary disease. Markers such as CEA, CA 19-9, CA 125 and others should be measured.

The treatment of metastatic PNETs is under much debate with some studies recommending aggressive treatment, and others, observation. There are no published guidelines, and there is very little Level I evidence on a proper treatment plan for these tumors. Hence, treatment is approached on an individual basis with consideration of disease burden and comorbidity[2]. Treatment includes somatostatin analogs, interferon-α, site-directed radioablation, cytotoxic chemotherapy, and molecular targeted therapy. Somatostatin analogs, such as octreotide, have been shown to result in tumor stabilization and symptom relief in some patients[11]. Clancy *et al*[10] have indicated that analogs only rarely lead to tumor regression and that these drugs may lose efficacy over time. Octreotide is given two or three times per day for 2 wk; then the long-acting drug is dosed at 10, 20 or 30 mg monthly. Chemotherapy with streptozotocin and 5-FU or doxorubicin has been used as first-line treatment[11], with response rates varying between 39% and 69%[4,7]. However, in patients with more malignant disease, therapy with cisplatin and etoposide has shown a response in 41%-67% of patients with poorly differentiated PNETs[11,20] and thus is used as initial therapy in these patients. Despite metastatic disease, our patient had significant improvement with 5-FU in combination with carboplatin (which has similar pharmacology to cisplatin), etoposide and octreotide. As a result, she serves as a good example of the benefits of aggressive medical and surgical management. In continuation of therapy, given the history of small bilateral pulmonary nodules and microscopically positive breast lesion margins, she will also receive postoperative chemotherapy with carboplatin and gemcitabine in an attempt to increase survival in this patient with R0 resection of the primary tumor.

No clear prognostic factors have been determined. However, many researchers have presented a variety of factors that could be used to assess survival. Prognosis can be stratified based on criteria from the WHO, which takes into account stage- and grade-related factors: tumor size, distant metastasis, mitotic rate, necrosis, and patient age[20]. Similarly, an analysis using the National Cancer Database of 3851 patients with PNETs has concluded that age, tumor grade, and distant metastasis were the most significant predictors of survival[5]. A study of 137 patients described by Clancy *et al*[10] has confirmed age as a strong prognostic factor, as demonstrated by both univariate and multivariate survival analysis ($P < 0.0003$)[10]. Of interest, one article stated that age is not a significant prognostic factor if the patient is found to be medically fit for surgery[7]. The analysis done by Clancy *et al*[10] also showed that chromogranin A level > 500 ng/mL was associated with decreased survival from the date of evaluation, on univariate survival analysis ($P < 0.030$). Additionally, it was proposed that elevated alkaline phosphatase levels (> 127 U/L) could serve as a marker of prognosis, because they were associated with shorter survival by both univariate and multivariate survival analysis. Kaifi *et al*[12] have evaluated 63 patients to determine L1, a cell adhesion molecule, as a possible prognostic marker of poorly differentiated carcinoma. In this study, there was no difference between primary and metastatic specimens; also normal tissue did not stain positive, while 44% of poorly differentiated carcinoma specimens stained positive, as opposed to 1.9% in well-differentiated carcinomas. A study by Strosberg *et al*[21] has proposed that the mitotic rate and Ki-67 index (measured using MIB-1) could be related to tumor grade and thus could be used as prognostic factors. Using a Ki-67 index of 0%-2% as low grade, 2%-20% as intermediate grade, > 20% as high grade, there was an inverse relationship between Ki-67 index and mitotic rate with survival. This was supported by Hochwald *et al*[16] who have reported that MIB-1 index and necrosis show a difference in survival. The significance between functional and non-functional tumors is controversial because some studies have concluded no significance[2,6], whereas others have reported that non-functional tumors have decreased survival[10]. Additionally, extensive metastatic disease has been associated with a decrease in survival rates[2]. From a surgical standpoint, Solorzano *et al*[18] have concluded that the ability to resect the primary tumor and extent of metastatic disease are powerful predictors of outcome ($P < 0.0001$ for both variables). Given the variability of these factors, it would be difficult to determine prognosis in this relatively young asymptomatic patient with a high grade, metastatic, non-functioning malignancy that underwent R0 resection of the primary tumor, a high index of MIB-1, and elevated alkaline phosphatase. The previously mentioned study by Bilimoria *et al*[5] has formulated a prognostic score to be used to estimate 5-year survival. A score is determined by assigning points to each prognostic factor: age, grade and distant metastasis. Using this model, our patient had a prognostic score of 3, which was associated with a 5-year survival of 35.7%. However, this model does not account for the aggressive treatment that she received. Despite this aggressive treatment, it is important that our patient has long-term follow-up to monitor for further metastases, especially of the liver, and for disease recurrence.

From our literature review, there is a necessity for further investigations to understand fully the spectrum of gastroenteropancreatic neuroendocrine tumors, especially with regard to the determination of prognosis. Our case supports the proposed utility and effectiveness of the various imaging modalities. It also provides evidence for the benefit of aggressive medical and surgical management, as well as the response of poorly differentiated PNETs to combination treatment. Currently, the patient is doing well and she will be routinely followed to monitor her disease course.

## APPENDIX A

Treatment was initiated with three cycles of 5-FU; the first dose being 360 mg/d × 3 d followed by 360 mg/d × 5 d, and finally, 360 mg/d × 4 d, each 1 wk apart. One month after completing 5-FU treatment, the patient received three cycles of carboplatin and etoposide; the first cycle was 900 mg/m$^2$ of carboplatin and etoposide at 160 mg/m$^2$ per day × 3 d. The remaining two cycles were completed 4 wk and 7 wk later with the regimen reduced to 720 mg/m$^2$ of carboplatin and 130 mg/m$^2$ per day × 3 d of etoposide. Filgrastim 273 μg every 3 d was started after the first round of carboplatin and etoposide for a total of four doses. At the end of both the second and third rounds of chemotherapy, a 6-mg dose of pegfilgrastim was received. Finally, 3 wk after completing the first round of carboplatin and etoposide, darbepoetin α was started with a total of three doses received; each 500 μg was received at 3-wk intervals, with the last dose being received at the completion of therapy.

## REFERENCES


1 **Tonnhofer U**, Balassy C, Reck CA, Koller A, Horcher E. Neuroendocrine tumor of the common hepatic duct, mimicking a choledochal cyst in a 6-year-old child. *J Pediatr Surg* 2009; **44**: E23-E25
2 **Bruzoni M**, Parikh P, Celis R, Are C, Ly QP, Meza JL, Sasson AR. Management of the primary tumor in patients with metastatic pancreatic neuroendocrine tumor: a contemporary single-institution review. *Am J Surg* 2009; **197**: 376-381
3 **Lloyd RV**. Endocrine pathology: differential diagnosis and molecular advances. New Jersey: Hartman Press Inc., 2004: 325
4 **Abood GJ**, Go A, Malhotra D, Shoup M. The surgical and systemic management of neuroendocrine tumors of the pancreas. *Surg Clin North Am* 2009; **89**: 249-266, x
5 **Bilimoria KY**, Talamonti MS, Tomlinson JS, Stewart AK, Winchester DP, Ko CY, Bentrem DJ. Prognostic score predicting survival after resection of pancreatic neuroendocrine tumors: analysis of 3851 patients. *Ann Surg* 2008; **247**: 490-500
6 **O'Grady HL**, Conlon KC. Pancreatic neuroendocrine tumours. *Eur J Surg Oncol* 2008; **34**: 324-332
7 **Hodul PJ**, Strosberg JR, Kvols LK. Aggressive surgical resection in the management of pancreatic neuroendocrine tumors: when is it indicated? *Cancer Control* 2008; **15**: 314-321
8 **You DD**, Lee HG, Paik KY, Heo JS, Choi SH, Choi DW. The outcomes after surgical resection in pancreatic endocrine tumors: an institutional experience. *Eur J Surg Oncol* 2009; **35**: 728-733
9 **Mullan MH**, Gauger PG, Thompson NW. Endocrine tumours of the pancreas: review and recent advances. *ANZ J Surg* 2001; **71**: 475-482
10 **Clancy TE**, Sengupta TP, Paulus J, Ahmed F, Duh MS, Kulke MH. Alkaline phosphatase predicts survival in patients with metastatic neuroendocrine tumors. *Dig Dis Sci* 2006; **51**: 877-884
11 **Granberg D**, Öberg K. Neuroendocrine tumours. *Update Cancer Ther* 2006; **1**: 75-84
12 **Kaifi JT**, Zinnkann U, Yekebas EF, Schurr PG, Reichelt U, Wachowiak R, Fiegel HC, Petri S, Schachner M, Izbicki JR. L1 is a potential marker for poorly-differentiated pancreatic neuroendocrine carcinoma. *World J Gastroenterol* 2006; **12**: 94-98
13 **Kouvaraki MA**, Solorzano CC, Shapiro SE, Yao JC, Perrier ND, Lee JE, Evans DB. Surgical treatment of non-functioning pancreatic islet cell tumors. *J Surg Oncol* 2005; **89**: 170-185
14 **Thompson GB**, van Heerden JA, Grant CS, Carney JA, Ilstrup DM. Islet cell carcinomas of the pancreas: a twenty-year experience. *Surgery* 1988; **104**: 1011-1017
15 **Solcia E**, Kloppel G, Sobin LH. Histological typing of endocrine tumours. In: WHO international histological classification of tumours. Berlin: Springer, 2000
16 **Hochwald SN**, Zee S, Conlon KC, Colleoni R, Louie O, Brennan MF, Klimstra DS. Prognostic factors in pancreatic endocrine neoplasms: an analysis of 136 cases with a proposal for low-grade and intermediate-grade groups. *J Clin Oncol* 2002; **20**: 2633-2642
17 **Unger P**. Pathology of Pancreatic Endocrine Neoplasia. In: Schwartz AE, Pertsemlidis D, Gagner M, editors. Endocrine surgery. New York: Marcel Dekker Inc., 2004: 500-520
18 **Solorzano CC**, Lee JE, Pisters PW, Vauthey JN, Ayers GD, Jean ME, Gagel RF, Ajani JA, Wolff RA, Evans DB. Nonfunctioning islet cell carcinoma of the pancreas: survival results in a contemporary series of 163 patients. *Surgery* 2001; **130**: 1078-1085
19 **Gomez-Rivera F**, Stewart AE, Arnoletti JP, Vickers S, Bland KI, Heslin MJ. Surgical treatment of pancreatic endocrine neoplasms. *Am J Surg* 2007; **193**: 460-465
20 **Kulke M**. Management of metastatic gastroenteropancreatic neuroendocrine tumors. Waltham, MA: UpToDate, 2009
21 **Strosberg J**, Nasir A, Coppola D, Wick M, Kvols L. Correlation between grade and prognosis in metastatic gastroenteropancreatic neuroendocrine tumors. *Hum Pathol* 2009; **40**: 1262-1268


**S- Editor** Cheng JX **L- Editor** Kerr C **E- Editor** Zheng XM

World Journal of Radiology

Online Submissions: http://www.wjgnet.com/1949-8470office
wjr@wjgnet.com
doi:10.4329/wjr.v3.i1.38

*World J Radiol* 2011 January 28; 3(1): 38-40
ISSN 1949-8470 (online)
© 2011 Baishideng. All rights reserved.

CASE REPORT

# Gallstone in jejunal limb with jejunocolonic fistula 10 years after Roux-en-Y choledochojejunostomy

Tao Suo, Lu-Jun Song, Sai-Xiong Tong

Tao Suo, Lu-Jun Song, Sai-Xiong Tong, Department of General Surgery, Zhongshan Hospital, Fudan University, General Surgery Institute of Fudan University, Shanghai 200032, China
Author contributions: Tong SX diagnosed the case; Song LJ and Tong SX performed the operation; Suo T collected the data and carried out the follow-up; Suo T wrote the paper; all authors approved the final manuscript.
Correspondence to: Sai-Xiong Tong, MD, Department of General Surgery, Zhongshan Hospital, Fudan University, General Surgery Institute of Fudan University, 180 Fenglin Road, Xuhui District, Shanghai 200032, China. tong.saixiong@live.cn
Telephone: +86-21-64041990 Fax: +86-21-64038472
Received: November 30, 2010 Revised: December 20, 2010
Accepted: December 27, 2010
Published online: January 28, 2011

**Key words:** Gallstone; Roux-en-Y choledochojejunostomy; Jejunocolonic fistula

**Peer reviewer:** Beat Schnüriger, MD, University of Southern California, Keck School of Medicine, Department of Surgery, Division of Acute Care Surgery, (Trauma, Emergency Surgery and Surgical Critical Care), 1200 North State Street, Inpatient Tower (C), 5th Floor, Room C5L100, Los Angeles, CA 90033-4525, United States

Suo T, Song LJ, Tong SX. Gallstone in jejunal limb with jejunocolonic fistula 10 years after Roux-en-Y choledochojejunostomy. *World J Radiol* 2011; 3(1): 38-40 Available from: URL: http://www.wjgnet.com/1949-8470/full/v3/i1/38.htm DOI: http://dx.doi.org/10.4329/wjr.v3.i1.38

## Abstract

Roux-en-Y choledochojejunostomy is a common biliary reconstruction procedure. The collection of gallstones in the jejunal limb is a rare complication. Here we present a case of a 61-year-old Chinese female who received Roux-en-Y choledochojejunostomy 10 years ago. Diagnosis of recurrent bile duct stones accompanying infection was made before operation. She also had an abdominal mass which was possibly an intussuscepted colon or a huge fecolith. At laparotomy, an oval stone (5 cm in diameter) and 3 smaller multifaceted stones (2 cm in diameter) were found in the jejunal limb. A fistula between this jejunum and colon was also found. Although the typical manifestations of diarrhea were present, the diagnosis of a biliary colonic fistula was missed before operation. Partial colectomy was performed with the fistulous opening repaired. A T-tube was left in the jejunal limb and the mesocolon aperture was enlarged and revised. Her postoperative convalescence was uneventful. We report this case hoping to sharpen our diagnostic acumen.

© 2011 Baishideng. All rights reserved.

## INTRODUCTION

Roux-en-Y choledochojejunostomy is common procedure for biliary reconstruction. This procedure has early and late complications although it is effective and sometimes the only alternation[1,2]. The collection of gallstones in the jejunal limb is a rare complication[3]. Biliary colonic fistula is also one of rare complications following gallstone disease[4]. A fistula between reconstructed biliary tract and colon is hard to be recognized beforehand. Although diarrhea and infection may be claimed, they are typical but non-specific clinical manifestations.

Here we present a case of recurrent bile duct stones with infection and an abdominal mass in a 61-year-old female 10 years after Roux-en-Y choledochojejunostomy. A preoperatively missing biliary colonic fistula was found during operation.

## CASE REPORT

A 61-year-old female complained of abdominal pain and unrelenting fever for 2 wk. She underwent cholecystectomy 10 years ago. Other details were not available. She had


**Figure 1 Computed tomography showing air (arrows) and stones (white arrows) in distended bile ducts.**

a mild vague right abdominal discomfort on and off after operation. About 2 years ago, her discomfort increased in intensity and turned into pain and became more frequent. Chills and high fever accompanied the episodes and she also developed chronic diarrhea, 6-8 motions a day, with scanty stools.

On examination, she appeared emaciated, pale and malnourished. Her temperature was 39℃, pulse rate 95/min, blood pressure 101/69 mmHg, and respiratory rate 18/min. She had no jaundice and the right upper rectus incision healed well. There was fullness of the right upper abdomen. A mass with vague margins was palpable with no significant muscle spasm. Her white blood cell count was 3100 per $mm^3$ with 68.9% neutrophils, her hemoglobin and hematocrit values were 10.8 g/dL and 33.2%, respectively. Serum chemistry studies demonstrated that her total bilirubin was 21.1 μmol/L (normal range = 3.4-21.1 μmol/L), direct bilirubin 13.9 μmol/L (normal range < 6.8 μmol/L), alkaline phosphatase 335 U/L (normal range = 42-28 U/L), AST 71 U/L (normal range < 75 U/L), ALT 58 U/L (normal range < 75 U/L), albumin 28 g/L (normal range = 35-52 g/L), and prealbumin 0.17 g/L (normal range = 0.25-0.4 g/L). Imaging studies showed air (black arrows) and stones (white arrows) in the diffusely distended bile passages (Figure 1) and a mass or filling defect in the intestine (white circle) (Figure 2A and B).

A diagnosis of recurrent bile duct stones with infection was made. The abdominal mass was possibly an intussuscepted colon or a huge fecalith. She was managed conservatively and prepared for surgery.

At laparotomy, a Roux-en-Y choledochojejunostomy was found. The jejunal limb was markedly distended and intimately adhered to the hepatic flexure of the colon. A mass (5 cm in diameter) could be palpated in the jejunal limb. The ascending and transverse colons were mobilized with no tumor mass found. The jejunal limb was opened with an oval stone (5 cm in diameter) and 3 smaller multifaceted stones (2 cm in diameter) removed. The big stone was light yellow in color, stratified and loose in texture, with a 1.2 cm hard dark yellow kernel. The multifaceted stones were brown and hard, typical of mixed stones.

The hepatic ducts were patent with no stones observed during exploration with a choledochoscope and the bilioenteric anastomosis was 1.5 cm long. However, turbid yellowish fluid continuously oozed from the posterior wall of the jejunal limb. A fistula between the jejunum and colon was found with an opening about 2 cm in diameter. The adjacent bowel wall was not thickened. A frozen section biopsy of the colon mucosa showed only chronic inflammation.

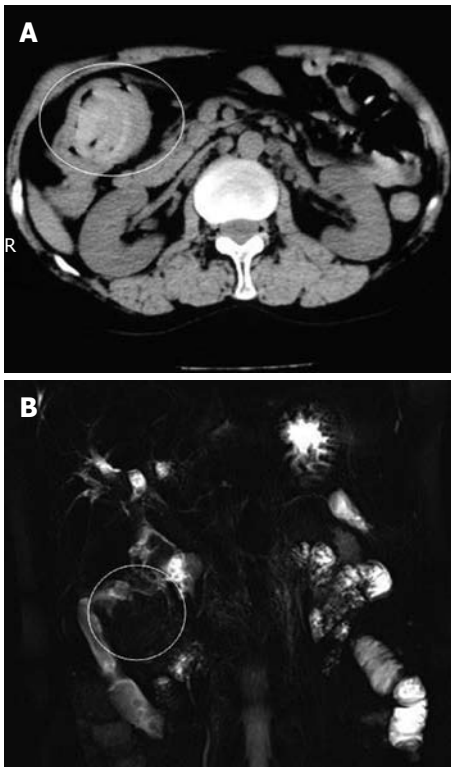


**Figure 2 A mass or filling defect in the intestine (white circle).** A: Computed tompograph image; B: Magnetic resonance image.

The jejunal limb was 40 cm in length and compressed by a tight mesocolon aperture. A partial colectomy was performed with the fistulous opening repaired and reinforced using a piece of colon wall. A T-tube was left in the jejunal limb with the mesocolon aperture enlarged and revised. It is a pity that we did not take photos during the operation.

Her postoperative convalescence was uneventful except for a wound infection. Her diarrhea subsided and her general condition improved. A T-tube cholangiogram showed a patent bile passage with normal jejunal emptying functions 2 wk after operation. The patient took 5 tablets of Dan-Ning-Pian (traditional Chinese medicine) 3 times per day to prevent recurrence of the stone.

## DISCUSSION

The significance of this report is the preoperative diagnostic challenge for gallstone in jejunal lim. The precise location of a huge stone detected on imaging studies before operation cannot be pin-pointed anatomically. Most observers made a diagnosis of a mass or filling defect in

the colon. Due to the stratified structure of the mass, an intussusception of the colon cannot be excluded merely on unenhanced CT scanning. As intussusception or stercolith obstruction cannot be ruled out, surgery is usually performed.

Without any question, recurrent stones and infection were present in this case. Air in the biliary passage is an expected sequel of a bilioenteric anastomosis. However, in this case, a previous bilioenteric procedure was not known exactly. A huge stone in the jejunal limb was a surprise to all. To our knowledge, only 3 cases have been reported[3-5]. Although the typical manifestations of diarrhea and infection were present in our case, the diagnosis of a biliary colonic fistula was missed before operation as previously described[6]. It was only found on careful examination at operation. On the other hand, since the patient had not any evidence of colon obstruction, a diagnosis of possible obstruction due to intussusception or stercolith was completely groundless.

Roux-en-Y choledochojejunostomy is a common and effective procedure for biliary reconstruction. However, it is not without early and late complications. Reoperation may be necessary because of anastomotic stricture, calculi recurrence, biliary tract infection, or even malignant change[2]. Even though anastomotic stricture is relatively common after a bilioenteric procedure, this patient had not any stricture 10 years after Roux-en-Y choledochojejunostomy. Although collection of stones in the jejunal limb has been reported, to our knowledge, it is uncommon[3-5]. Such collection may be due to delayed emptying of the jejunal limb, because of motility dysfunction or mechanical obstruction because of torsion or kinking or compression of the limb by a tight mesocolon aperture. Poor emptying of the jejunal limb might have played an important role and a tight mesocolon aperture was the culprit in this case. Stasis caused the growth of the stone. Together with repeated infection, it finally led to formation of the jejunocolonic fistula.

Although a strictured anastomosis is the most frequent indication for reoperation after a Roux-en-Y bilioenteric procedure, one should also be on the alert for other conditions, such as motility dysfunction or inadequate patency as a cause for the delayed emptying of the jejunal limb. We report this case hoping to sharpen our diagnostic acumen.

## ACKNOWLEDGMENTS

The authors thank Professor Zhao-Guang Wu and Professor Roland Andersson for their advice and assistance in preparation of the manuscript.

## REFERENCES

1 **Röthlin MA**, Löpfe M, Schlumpf R, Largiadèr F. Long-term results of hepaticojejunostomy for benign lesions of the bile ducts. *Am J Surg* 1998; **175**: 22-26
2 **Li Z**, Cui N, Chen L. Treatment experience of subsequent complications after Roux-en-Y biliojejunostomy. *Eur Surg Res* 2009; **43**: 34-38
3 **Ajiki T**, Suzuki Y, Okazaki T, Fujino Y, Yoshikawa T, Sawa H, Hirata K, Kuroda Y. A large stone detected in Roux-en-Y jejunal limb 20 years after excision of congenital choledochal cyst. *Surgery* 2006; **139**: 129-130
4 **Wada N**, Seki M, Saikawa Y, Satoh M, Toizumi A, Tamura Y, Kageyama T, Otani Y, Kubota T, Kumai K, Kitajima M. Jejunal limb obstruction caused by a cholesterol stone 15 years after a total gastrectomy and 20 years after a cholecystectomy: report of a case. *Surg Today* 2000; **30**: 181-184
5 **De Moor V**, El Nakadi I, Jeanmart J, Gelin M, Donckier V. Cholangitis caused by Roux-en-Y hepaticojejunostomy obstruction by a biliary stone after liver transplantation. *Transplantation* 2003; **75**: 416-418
6 **Costi R**, Randone B, Violi V, Scatton O, Sarli L, Soubrane O, Dousset B, Montariol T. Cholecystocolonic fistula: facts and myths. A review of the 231 published cases. *J Hepatobiliary Pancreat Surg* 2009; **16**: 8-18

**S- Editor** Cheng JX **L- Editor** Wang XL **E- Editor** Zheng XM

World Journal of Radiology

Online Submissions: http://www.wjgnet.com/1949-8470office
wjr@wjgnet.com
www.wjgnet.com

*World J Radiol* 2011 January 28; 3(1): I
ISSN 1949-8470 (online)
© 2011 Baishideng. All rights reserved.



# Acknowledgments to reviewers of *World Journal of Radiology*

Many reviewers have contributed their expertise and time to the peer review, a critical process to ensure the quality of *World Journal of Radiology*. The editors and authors of the articles submitted to the journal are grateful to the following reviewers for evaluating the articles (including those published in this issue and those rejected for this issue) during the last editing time period.

**Tommaso Bartalena, MD, PhD,** Radiology, Poliambulatorio Privato Zappi Bartalena, via Cogne 27, Imola 40026, Italy

**Rivka R Colen, MD,** Department of Radiology, Brigham and Womens Hospital, 75 Francis St, Boston, MA 02115, United States

**Ragab Hani Donkol, Professor,** Radiology Department, Aseer Central Hospital, 34 Abha, Saudi Arabia

**Francesco Lassandro, MD,** Department of Radiology, Monaldi Hospital, via Leonardo Bianchi, Napoli, 80129, Italy

**Edson Marchiori, MD, PhD,** Full Professor of Radiology, Department of Radiology, Fluminense Federal University, Rua Thomaz Cameron, 438, Valparaiso, CEP 25685, 120, Petrópolis, Rio de Janeiro, Brazil

**Yasunori Minami, MD, PhD, Assistant Professor,** Division of Gastroenterology and Hepatology, Department of Internal Medicine, Kinki University School of Medicine, 377-2 Ohno-higashi, Osaka-sayama, Osaka, 589-8511, Japan

**Ian C Roberts-Thomson, Professor,** Department of Gastroenterology and Hepatology, The Queen Elizabeth Hospital, 28 Woodville Road, Woodville South, 5011, Australia

**Ioannis Valais, PhD,** Department of Medical Instrument Technology , Technological Educational Institution of Athens, Ag Spyridonos and Dimitsanis, Egaleo, Athens, 12210, Greece

**Edwin JR van Beek, MD, PhD, Med, FRCR, SINAPSE, Chair** of Clinical Radiology, CO.19, Clinical Research Imaging Centre, Queen's Medical Research Institute, University of Edinburgh, 47 Little France Crescent, Edinburgh EH16 4TJ, United Kingdom

**Xiao-Ming Zhang, MD, Professor,** Department of Radiology, Affiliated Hospital of North Sichuan Medical College, Wenhua Road 63, Nanchong 637000, Sichuan Province, China

WJR World Journal of Radiology

Online Submissions: http://www.wjgnet.com/1949-8470office
wjr@wjgnet.com
www.wjgnet.com

*World J Radiol* 2011 January 28; 3(1): I
ISSN 1949-8470 (online)
© 2011 Baishideng. All rights reserved.

# Meetings

## Events Calendar 2011

January 23-27
Radiology at Snowbird
San Diego, Mexico

January 24-28
Neuro/ENT at the Beach
Palm Beach, FL, United States

January 28-29
MIAD 2011 - 2nd International Workshop on Medical Image Analysis and Description for Diagnosis System
Rome, Italy

February 5-6
Washington Neuroradiology Review
Arlington, VA, United States

February 12-17
MI11 - SPIE Medical Imaging 2011
Lake Buena Vista, FL, United States

February 17-18
2nd National Conference Diagnostic and Interventional Radiology 2011
London, United Kingdom

Februrary 17-18
VII National Neuroradiology Course
Lleida, Spain

February 18
Radiology in child protection
Nottingham, United Kingdom

Februrary 19-22
COMPREHENSIVE REVIEW OF MUSCULOSKELETAL MRI
Lake Buena Vista, FL, United States

March 2-5
2011 Abdominal Radiology Course
Carlsbad, CA, United States

March 3-7
European Congress of Radiology Meeting ECR 2011
Vienna, Austria

March 6-9
World Congress Thoracic Imaging - IV
Bonita Springs, FL, United States

March 14-18
9th Annual NYU Radiology Alpine Imaging Symposium at Beaver Creek
Beaver Creek, CO, United States

March 20-25
Abdominal Radiology Course 2011
Carlsbad, CA, United States

March 26-31
2011 SIR Annual Meeting
Chicago, IL, United States

March 28-April 1
University of Utah Neuroradiology 2nd Intensive Interactive Brain & Spine Imaging Conference
Salt Lake City, UT, United States

April 3-8
1st Annual Ottawa Radiology Resident Review
Ottawa, Canada

April 3-8
43rd International Diagnostic Course Davos on Diagnostic Imaging and Interventional Techniques
Davos, Switzerland

April 6-9
Image-Based Neurodiagnosis: Intensive Clinical and Radiologic Review, CAQ Preparation
Cincinnati, OH, United States

April 28-May 1
74th Annual Scientific Meeting of the Canadian Association of Radiologists CAR
Montreal, Canada

May 5-8
EMBL Conference-Sixth International Congress on Electron Tomography
Heidelberg, Germany

May 10-13
27th Iranian Congress of Radiology
Tehran, Iran

May 14-21
Radiology in Marrakech
Marrakech, Morocco

May 21-24
European Society of Gastrointestinal and Abdominal Radiology 2011 Annual Meeting
Venice, Italy

May 23-25
Sports Medicine Imaging State of the Art: A Collaborative Course for Radiologists and Sports Medicine Specialists
New York, NY, United States

May 24-26
Russian Congress of Radiology
Moscow, Russia

May 28-31
International Congress of Pediatric Radiology (IPR)
London, United Kingdom

June 4-8
58th Annual Meeting of the Society of Nuclear Medicine
San Antonio, TX, United States

June 6-8
UKRC 2011 - UK Radiological Congress
Manchester, United Kingdom

June 8-11
CIRA 2011 - Canadian Internventinal Radiology Association Meeting
Montreal, QC, Canada

June 9-10
8th ESGAR Liver Imaging Workshop
Dublin, Ireland

June 17-19
ASCI 2011 - 5th Congress of Asian Society of Cardiovascular Imaging
Hong Kong, China

June 22-25
CARS 2011 - Computer Assisted Radiology and Surgery - 25th International Congress and Exhibition
Berlin, Germany

June 27-July 1
NYU Summer Radiology Symposium at The Sagamore
Lake George, NY, United States

July 18-22
Clinical Case-Based Radiology Update in Iceland
Reykjavik, Iceland

August 1-5
NYU Clinical Imaging Symposium in Santa Fe
Santa Fe, NM, United States

September 22-25
European Society of Neuroradiology (ESNR) XXXV Congress and 19th Advanced Course
Antwerp, Belgium

October 12-14
International Conference Vipimage 2011 - Computational Vision and Medical Image Processing
Algarve, Portugal

October 15-16
Essentials of Emergency and Trauma Radiology
Ottawa, Canada

October 23-29
2011 IEEE NSS - 2011 IEEE Nuclear Science Symposium and Medical Imaging Conference
Valencia, Spain

October 25-28
NYU Radiology in Scottsdale - Fall Radiology Symposium in Scottsdale
Scottsdale, AZ, United States

October 28-30
Fourth National Congress of Professionals of Radiological Techniques
Florianópolis, Brazil

October 28-30
Multi-Modality Gynecological & Obstetric Imaging
Ottawa, Canada

November 3-4
9th ESGAR Liver Imaging Workshop
Taormina, Italy

November 15-19
EANM 2011 - Annual Congress of the European Association of Nuclear Medicine
Birmingham, United Kingdom

November 22-29
NSS/MIC - Nuclear Science Symposium and Medical Imaging Conference 2011
Valencia, Spain

November 26-28
8th Asia Oceaninan Congress of Neuro-Radiology
Bangkok, Thailand

World Journal of Radiology

Online Submissions: http://www.wjgnet.com/1949-8470office
wjr@wjgnet.com
www.wjgnet.com

*World J Radiol* 2011 January 28; 3(1): I-V
ISSN 1949-8470 (online)
© 2011 Baishideng. All rights reserved.

# Instructions to authors

## GENERAL INFORMATION

*World Journal of Radiology* (*World J Radiol*, *WJR*, online ISSN 1949-8470, DOI: 10.4329), is a monthly, open-access (OA), peer-reviewed journal supported by an editorial board of 319 experts in Radiology from 40 countries.

The biggest advantage of the OA model is that it provides free, full-text articles in PDF and other formats for experts and the public without registration, which eliminates the obstacle that traditional journals possess and usually delays the speed of the propagation and communication of scientific research results. The open access model has been proven to be a true approach that may achieve the ultimate goal of the journals, i.e. the maximization of the value to the readers, authors and society.

### *Maximization of personal benefits*

The role of academic journals is to exhibit the scientific levels of a country, a university, a center, a department, and even a scientist, and build an important bridge for communication between scientists and the public. As we all know, the significance of the publication of scientific articles lies not only in disseminating and communicating innovative scientific achievements and academic views, as well as promoting the application of scientific achievements, but also in formally recognizing the "priority" and "copyright" of innovative achievements published, as well as evaluating research performance and academic levels. So, to realize these desired attributes of *WJR* and create a well-recognized journal, the following four types of personal benefits should be maximized. The maximization of personal benefits refers to the pursuit of the maximum personal benefits in a well-considered optimal manner without violation of the laws, ethical rules and the benefits of others. (1) Maximization of the benefits of editorial board members: The primary task of editorial board members is to give a peer review of an unpublished scientific article via online office system to evaluate its innovativeness, scientific and practical values and determine whether it should be published or not. During peer review, editorial board members can also obtain cutting-edge information in that field at first hand. As leaders in their field, they have priority to be invited to write articles and publish commentary articles. We will put peer reviewers' names and affiliations along with the article they reviewed in the journal to acknowledge their contribution; (2) Maximization of the benefits of authors: Since *WJR* is an open-access journal, readers around the world can immediately download and read, free of charge, high-quality, peer-reviewed articles from *WJR* official website, thereby realizing the goals and significance of the communication between authors and peers as well as public reading; (3) Maximization of the benefits of readers: Readers can read or use, free of charge, high-quality peer-reviewed articles without any limits, and cite the arguments, viewpoints, concepts, theories, methods, results, conclusion or facts and data of pertinent literature so as to validate the innovativeness, scientific and practical values of their own research achievements, thus ensuring that their articles have novel arguments or viewpoints, solid evidence and correct conclusion; and (4) Maximization of the benefits of employees: It is an iron law that a first-class journal is unable to exist without first-class editors, and only first-class editors can create a first-class academic journal. We insist on strengthening our team cultivation and construction so that every employee, in an open, fair and transparent environment, could contribute their wisdom to edit and publish high-quality articles, thereby realizing the maximization of the personal benefits of editorial board members, authors and readers, and yielding the greatest social and economic benefits.

### *Aims and scope*

The major task of *WJR* is to rapidly report the most recent improvement in the research of medical imaging and radiation therapy by the radiologists. *WJR* accepts papers on the following aspects related to radiology: Abdominal radiology, women health radiology, cardiovascular radiology, chest radiology, genitourinary radiology, neuroradiology, head and neck radiology, interventional radiology, musculoskeletal radiology, molecular imaging, pediatric radiology, experimental radiology, radiological technology, nuclear medicine, PACS and radiology informatics, and ultrasound. We also encourage papers that cover all other areas of radiology as well as basic research.

### *Columns*

The columns in the issues of *WJR* will include: (1) Editorial: To introduce and comment on major advances and developments in the field; (2) Frontier: To review representative achievements, comment on the state of current research, and propose directions for future research; (3) Topic Highlight: This column consists of three formats, including (A) 10 invited review articles on a hot topic, (B) a commentary on common issues of this hot topic, and (C) a commentary on the 10 individual articles; (4) Observation: To update the development of old and new questions, highlight unsolved problems, and provide strategies on how to solve the questions; (5) Guidelines for Basic Research: To provide guidelines for basic research; (6) Guidelines for Clinical Practice: To provide guidelines for clinical diagnosis and treatment; (7) Review: To review systemically progress and unresolved problems in the field, comment on the state of current research, and make suggestions for future work; (8) Original Articles: To report innovative and original findings in radiology; (9) Brief Articles: To briefly report the novel and innovative findings in radiology; (10) Case Report: To report a rare or typical case; (11) Letters to the Editor: To discuss and make reply to the contributions published in *WJR*, or to introduce and comment on a controversial issue of general interest; (12) Book Reviews: To introduce and comment on quality monographs of radiology; and (13) Guidelines: To introduce consensuses and guidelines reached by international and national academic authorities worldwide on the research in radiology.

### *Name of journal*

*World Journal of Radiology*

### *CSSN*

ISSN 1949-8470 (online)

### *Indexed and Abstracted in*

PubMed Central, PubMed.

### *Published by*

Baishideng Publishing Group Co., Limited

## SPECIAL STATEMENT

All articles published in this journal represent the viewpoints of the authors except where indicated otherwise.

### *Biostatistical editing*

Statisital review is performed after peer review. We invite an expert in Biomedical Statistics from to evaluate the statistical method used in the paper, including *t*-test (group or paired comparisons), chi-

squared test, Ridit, probit, logit, regression (linear, curvilinear, or stepwise), correlation, analysis of variance, analysis of covariance, *etc*. The reviewing points include: (1) Statistical methods should be described when they are used to verify the results; (2) Whether the statistical techniques are suitable or correct; (3) Only homogeneous data can be averaged. Standard deviations are preferred to standard errors. Give the number of observations and subjects (*n*). Losses in observations, such as drop-outs from the study should be reported; (4) Values such as ED50, LD50, IC50 should have their 95% confidence limits calculated and compared by weighted probit analysis (Bliss and Finney); and (5) The word 'significantly' should be replaced by its synonyms (if it indicates extent) or the *P* value (if it indicates statistical significance).

### *Conflict-of-interest statement*

In the interests of transparency and to help reviewers assess any potential bias, *WJR* requires authors of all papers to declare any competing commercial, personal, political, intellectual, or religious interests in relation to the submitted work. Referees are also asked to indicate any potential conflict they might have reviewing a particular paper. Before submitting, authors are suggested to read "Uniform Requirements for Manuscripts Submitted to Biomedical Journals: Ethical Considerations in the Conduct and Reporting of Research: Conflicts of Interest" from International Committee of Medical Journal Editors (ICMJE), which is available at: http://www.icmje.org/ethical_4conflicts.html.

Sample wording: [Name of individual] has received fees for serving as a speaker, a consultant and an advisory board member for [names of organizations], and has received research funding from [names of organization]. [Name of individual] is an employee of [name of organization]. [Name of individual] owns stocks and shares in [name of organization]. [Name of individual] owns patent [patent identification and brief description].

### *Statement of informed consent*

Manuscripts should contain a statement to the effect that all human studies have been reviewed by the appropriate ethics committee or it should be stated clearly in the text that all persons gave their informed consent prior to their inclusion in the study. Details that might disclose the identity of the subjects under study should be omitted. Authors should also draw attention to the Code of Ethics of the World Medical Association (Declaration of Helsinki, 1964, as revised in 2004).

### *Statement of human and animal rights*

When reporting the results from experiments, authors should follow the highest standards and the trial should conform to Good Clinical Practice (for example, US Food and Drug Administration Good Clinical Practice in FDA-Regulated Clinical Trials; UK Medicines Research Council Guidelines for Good Clinical Practice in Clinical Trials) and/or the World Medical Association Declaration of Helsinki. Generally, we suggest authors follow the lead investigator's national standard. If doubt exists whether the research was conducted in accordance with the above standards, the authors must explain the rationale for their approach and demonstrate that the institutional review body explicitly approved the doubtful aspects of the study.

Before submitting, authors should make their study approved by the relevant research ethics committee or institutional review board. If human participants were involved, manuscripts must be accompanied by a statement that the experiments were undertaken with the understanding and appropriate informed consent of each. Any personal item or information will not be published without explicit consents from the involved patients. If experimental animals were used, the materials and methods (experimental procedures) section must clearly indicate that appropriate measures were taken to minimize pain or discomfort, and details of animal care should be provided.

## SUBMISSION OF MANUSCRIPTS

Manuscripts should be typed in 1.5 line spacing and 12 pt. Book Antiqua with ample margins. Number all pages consecutively, and start each of the following sections on a new page: Title Page, Abstract, Introduction, Materials and Methods, Results, Discussion, Acknowledgements, References, Tables, Figures, and Figure Legends. Neither the editors nor the publisher are responsible for the opinions expressed by contributors. Manuscripts formally accepted for publication become the permanent property of Baishideng Publishing Group Co., Limited, and may not be reproduced by any means, in whole or in part, without the written permission of both the authors and the publisher. We reserve the right to copy-edit and put onto our website accepted manuscripts. Authors should follow the relevant guidelines for the care and use of laboratory animals of their institution or national animal welfare committee. For the sake of transparency in regard to the performance and reporting of clinical trials, we endorse the policy of the ICMJE to refuse to publish papers on clinical trial results if the trial was not recorded in a publicly-accessible registry at its outset. The only register now available, to our knowledge, is http://www.clinicaltrials.gov sponsored by the United States National Library of Medicine and we encourage all potential contributors to register with it. However, in the case that other registers become available you will be duly notified. A letter of recommendation from each author's organization should be provided with the contributed article to ensure the privacy and secrecy of research is protected.

Authors should retain one copy of the text, tables, photographs and illustrations because rejected manuscripts will not be returned to the author(s) and the editors will not be responsible for loss or damage to photographs and illustrations sustained during mailing.

### *Online submissions*

Manuscripts should be submitted through the Online Submission System at: http://www.wjgnet.com/1949-8470office. Authors are highly recommended to consult the ONLINE INSTRUCTIONS TO AUTHORS (http://www.wjgnet.com/1949-8470/g_info_20100316162358.htm) before attempting to submit online. For assistance, authors encountering problems with the Online Submission System may send an email describing the problem to wjr@wjgnet.com, or by telephone: +86-10-85381892. If you submit your manuscript online, do not make a postal contribution. Repeated online submission for the same manuscript is strictly prohibited.

## MANUSCRIPT PREPARATION

All contributions should be written in English. All articles must be submitted using word-processing software. All submissions must be typed in 1.5 line spacing and 12 pt. Book Antiqua with ample margins. Style should conform to our house format. Required information for each of the manuscript sections is as follows:

### *Title page*

**Title:** Title should be less than 12 words.

**Running title:** A short running title of less than 6 words should be provided.

**Authorship:** Authorship credit should be in accordance with the standard proposed by International Committee of Medical Journal Editors, based on (1) substantial contributions to conception and design, acquisition of data, or analysis and interpretation of data; (2) drafting the article or revising it critically for important intellectual content; and (3) final approval of the version to be published. Authors should meet conditions 1, 2, and 3.

**Institution:** Author names should be given first, then the complete name of institution, city, province and postcode. For example, Xu-Chen Zhang, Li-Xin Mei, Department of Pathology, Chengde Medical College, Chengde 067000, Hebei Province, China. One author may be represented from two institutions, for example, George Sgourakis, Department of General, Visceral, and Transplantation Surgery, Essen 45122, Germany; George Sgourakis, 2nd Surgical

Department, Korgialenio-Benakio Red Cross Hospital, Athens 15451, Greece

**Author contributions:** The format of this section should be: Author contributions: Wang CL and Liang L contributed equally to this work; Wang CL, Liang L, Fu JF, Zou CC, Hong F and Wu XM designed the research; Wang CL, Zou CC, Hong F and Wu XM performed the research; Xue JZ and Lu JR contributed new reagents/analytic tools; Wang CL, Liang L and Fu JF analyzed the data; and Wang CL, Liang L and Fu JF wrote the paper.

**Supportive foundations:** The complete name and number of supportive foundations should be provided, e.g., Supported by National Natural Science Foundation of China, No. 30224801

**Correspondence to:** Only one corresponding address should be provided. Author names should be given first, then author title, affiliation, the complete name of institution, city, postcode, province, country, and email. All the letters in the email should be in lower case. A space interval should be inserted between country name and email address. For example, Montgomery Bissell, MD, Professor of Medicine, Chief, Liver Center, Gastroenterology Division, University of California, Box 0538, San Francisco, CA 94143, United States. montgomery.bissell@ucsf.edu

**Telephone and fax:** Telephone and fax should consist of +, country number, district number and telephone or fax number, e.g., Telephone: +86-10-85381892 Fax: +86-10-85381893

**Peer reviewers:** All articles received are subject to peer review. Normally, three experts are invited for each article. Decision for acceptance is made only when at least two experts recommend an article for publication. Reviewers for accepted manuscripts are acknowledged in each manuscript, and reviewers of articles which were not accepted will be acknowledged at the end of each issue. To ensure the quality of the articles published in *WJR*, reviewers of accepted manuscripts will be announced by publishing the name, title/position and institution of the reviewer in the footnote accompanying the printed article. For example, reviewers: Professor Jing-Yuan Fang, Shanghai Institute of Digestive Disease, Shanghai, Affiliated Renji Hospital, Medical Faculty, Shanghai Jiaotong University, Shanghai, China; Professor Xin-Wei Han, Department of Radiology, The First Affiliated Hospital, Zhengzhou University, Zhengzhou, Henan Province, China; and Professor Anren Kuang, Department of Nuclear Medicine, Huaxi Hospital, Sichuan University, Chengdu, Sichuan Province, China.

### *Abstract*

There are unstructured abstracts (no more than 256 words) and structured abstracts (no more than 480). The specific requirements for structured abstracts are as follows:

An informative, structured abstracts of no more than 480 words should accompany each manuscript. Abstracts for original contributions should be structured into the following sections. AIM (no more than 20 words): Only the purpose should be included. Please write the aim as the form of "To investigate/study/…; MATERIALS AND METHODS (no more than 140 words); RESULTS (no more than 294 words): You should present *P* values where appropriate and must provide relevant data to illustrate how they were obtained, e.g. 6.92 ± 3.86 *vs* 3.61 ± 1.67, $P < 0.001$; CONCLUSION (no more than 26 words).

### *Key words*

Please list 5-10 key words, selected mainly from *Index Medicus*, which reflect the content of the study.

### *Text*

For articles of these sections, original articles and brief articles, the main text should be structured into the following sections: INTRODUCTION, MATERIALS AND METHODS, RESULTS and DISCUSSION, and should include appropriate Figures and Tables. Data should be presented in the main text or in Figures and Tables, but not in both. The main text format of these sections, editorial, topic highlight, case report, letters to the editors, can be found at: http://www.wjgnet.com/1949-8470/g_info_20100313183720.htm.

### *Illustrations*

Figures should be numbered as 1, 2, 3, *etc.*, and mentioned clearly in the main text. Provide a brief title for each figure on a separate page. Detailed legends should not be provided under the figures. This part should be added into the text where the figures are applicable. Figures should be either Photoshop or Illustrator files (in tiff, eps, jpeg formats) at high-resolution. Examples can be found at: http://www.wjgnet.com/1007-9327/13/4520.pdf; http://www.wjgnet.com/1007-9327/13/4554.pdf; http://www.wjgnet.com/1007-9327/13/4891.pdf; http://www.wjgnet.com/1007-9327/13/4986.pdf; http://www.wjgnet.com/1007-9327/13/4498.pdf. Keeping all elements compiled is necessary in line-art image. Scale bars should be used rather than magnification factors, with the length of the bar defined in the legend rather than on the bar itself. File names should identify the figure and panel. Avoid layering type directly over shaded or textured areas. Please use uniform legends for the same subjects. For example: Figure 1 Pathological changes in atrophic gastritis after treatment. A: ...; B: ...; C: ...; D: ...; E: ...; F: ...; G: …*etc.* It is our principle to publish high resolution-figures for the printed and E-versions.

### *Tables*

Three-line tables should be numbered 1, 2, 3, *etc.*, and mentioned clearly in the main text. Provide a brief title for each table. Detailed legends should not be included under tables, but rather added into the text where applicable. The information should complement, but not duplicate the text. Use one horizontal line under the title, a second under column heads, and a third below the Table, above any footnotes. Vertical and italic lines should be omitted.

### *Notes in tables and illustrations*

Data that are not statistically significant should not be noted. $^{a}P < 0.05$, $^{b}P < 0.01$ should be noted ($P > 0.05$ should not be noted). If there are other series of *P* values, $^{c}P < 0.05$ and $^{d}P < 0.01$ are used. A third series of *P* values can be expressed as $^{e}P < 0.05$ and $^{f}P < 0.01$. Other notes in tables or under illustrations should be expressed as $^{1}$F, $^{2}$F, $^{3}$F; or sometimes as other symbols with a superscript (Arabic numerals) in the upper left corner. In a multi-curve illustration, each curve should be labeled with ●, ○, ■, □, ▲, △, *etc.*, in a certain sequence.

### *Acknowledgments*

Brief acknowledgments of persons who have made genuine contributions to the manuscript and who endorse the data and conclusions should be included. Authors are responsible for obtaining written permission to use any copyrighted text and/or illustrations.

## REFERENCES

### *Coding system*

The author should number the references in Arabic numerals according to the citation order in the text. Put reference numbers in square brackets in superscript at the end of citation content or after the cited author's name. For citation content which is part of the narration, the coding number and square brackets should be typeset normally. For example, "Crohn's disease (CD) is associated with increased intestinal permeability[1,2]". If references are cited directly in the text, they should be put together within the text, for example, "From references[19,22-24], we know that..."

When the authors write the references, please ensure that the order in text is the same as in the references section, and also ensure the spelling accuracy of the first author's name. Do not list the same citation twice.

### *PMID and DOI*

Pleased provide PubMed citation numbers to the reference list, e.g. PMID and DOI, which can be found at http://www.ncbi.nlm.nih.gov/sites/entrez?db=pubmed and http://www.crossref.org/SimpleTextQuery/, respectively. The numbers will be used in E-version of this journal.

### *Style for journal references*

Authors: the name of the first author should be typed in bold-faced letters. The family name of all authors should be typed with the initial letter capitalized, followed by their abbreviated first and middle initials. (For example, Lian-Sheng Ma is abbreviated as Ma LS, Bo-Rong Pan as Pan BR). The title of the cited article and italicized journal title (journal title should be in its abbreviated form as shown in PubMed), publication date, volume number (in black), start page, and end page [PMID: 11819634 DOI: 10.3748/wjg.13.5396].

### *Style for book references*

Authors: the name of the first author should be typed in bold-faced letters. The surname of all authors should be typed with the initial letter capitalized, followed by their abbreviated middle and first initials. (For example, Lian-Sheng Ma is abbreviated as Ma LS, Bo-Rong Pan as Pan BR) Book title. Publication number. Publication place: Publication press, Year: start page and end page.

### *Format*

**Journals**

*English journal article (list all authors and include the PMID where applicable)*

1 **Jung EM**, Clevert DA, Schreyer AG, Schmitt S, Rennert J, Kubale R, Feuerbach S, Jung F. Evaluation of quantitative contrast harmonic imaging to assess malignancy of liver tumors: A prospective controlled two-center study. *World J Gastroenterol* 2007; **13**: 6356-6364 [PMID: 18081224 DOI: 10.3748/wjg.13.6356]

*Chinese journal article (list all authors and include the PMID where applicable)*

2 **Lin GZ**, Wang XZ, Wang P, Lin J, Yang FD. Immunologic effect of Jianpi Yishen decoction in treatment of Pixu-diarrhoea. *Shijie Huaren Xiaohua Zazhi* 1999; **7**: 285-287

*In press*

3 **Tian D**, Araki H, Stahl E, Bergelson J, Kreitman M. Signature of balancing selection in Arabidopsis. *Proc Natl Acad Sci USA* 2006; In press

*Organization as author*

4 **Diabetes Prevention Program Research Group**. Hypertension, insulin, and proinsulin in participants with impaired glucose tolerance. *Hypertension* 2002; **40**: 679-686 [PMID: 12411462 PMCID:2516377 DOI:10.1161/01.HYP.0000035706.28494.09]

*Both personal authors and an organization as author*

5 **Vallancien G**, Emberton M, Harving N, van Moorselaar RJ; Alf-One Study Group. Sexual dysfunction in 1, 274 European men suffering from lower urinary tract symptoms. *J Urol* 2003; **169**: 2257-2261 [PMID: 12771764 DOI:10.1097/01.ju.0000067940.76090.73]

*No author given*

6 21st century heart solution may have a sting in the tail. *BMJ* 2002; **325**: 184 [PMID: 12142303 DOI:10.1136/bmj.325.7357.184]

*Volume with supplement*

7 **Geraud G**, Spierings EL, Keywood C. Tolerability and safety of frovatriptan with short- and long-term use for treatment of migraine and in comparison with sumatriptan. *Headache* 2002; **42** Suppl 2: S93-99 [PMID: 12028325 DOI:10.1046/j.1526-4610.42.s2.7.x]

*Issue with no volume*

8 **Banit DM**, Kaufer H, Hartford JM. Intraoperative frozen section analysis in revision total joint arthroplasty. *Clin Orthop Relat Res* 2002; (**401**): 230-238 [PMID: 12151900 DOI:10.1097/00003086-200208000-00026]

*No volume or issue*

9 Outreach: Bringing HIV-positive individuals into care. *HRSA Careaction* 2002; 1-6 [PMID: 12154804]

**Books**

*Personal author(s)*

10 **Sherlock S**, Dooley J. Diseases of the liver and billiary system. 9th ed. Oxford: Blackwell Sci Pub, 1993: 258-296

*Chapter in a book (list all authors)*

11 **Lam SK**. Academic investigator's perspectives of medical treatment for peptic ulcer. In: Swabb EA, Azabo S. Ulcer disease: investigation and basis for therapy. New York: Marcel Dekker, 1991: 431-450

*Author(s) and editor(s)*

12 **Breedlove GK**, Schorfheide AM. Adolescent pregnancy. 2nd ed. Wieczorek RR, editor. White Plains (NY): March of Dimes Education Services, 2001: 20-34

*Conference proceedings*

13 **Harnden P**, Joffe JK, Jones WG, editors. Germ cell tumours V. Proceedings of the 5th Germ cell tumours Conference; 2001 Sep 13-15; Leeds, UK. New York: Springer, 2002: 30-56

*Conference paper*

14 **Christensen S**, Oppacher F. An analysis of Koza's computational effort statistic for genetic programming. In: Foster JA, Lutton E, Miller J, Ryan C, Tettamanzi AG, editors. Genetic programming. EuroGP 2002: Proceedings of the 5th European Conference on Genetic Programming; 2002 Apr 3-5; Kinsdale, Ireland. Berlin: Springer, 2002: 182-191

**Electronic journal** (list all authors)

15 Morse SS. Factors in the emergence of infectious diseases. Emerg Infect Dis serial online, 1995-01-03, cited 1996-06-05; 1(1): 24 screens. Available from: URL: http://www.cdc.gov/ncidod/eid/index.htm

**Patent** (list all authors)

16 **Pagedas AC**, inventor; Ancel Surgical R&D Inc., assignee. Flexible endoscopic grasping and cutting device and positioning tool assembly. United States patent US 20020103498. 2002 Aug 1

### *Statistical data*

Write as mean ± SD or mean ± SE.

### *Statistical expression*

Express *t* test as *t* (in italics), *F* test as *F* (in italics), chi square test as $\chi^2$ (in Greek), related coefficient as *r* (in italics), degree of freedom as υ (in Greek), sample number as *n* (in italics), and probability as *P* (in italics).

### *Units*

Use SI units. For example: body mass, m (B) = 78 kg; blood pressure, p (B) = 16.2/12.3 kPa; incubation time, t (incubation) = 96 h, blood glucose concentration, c (glucose) 6.4 ± 2.1 mmol/L; blood CEA mass concentration, p (CEA) = 8.6 24.5 μg/L; $CO_2$ volume fraction, 50 mL/L $CO_2$, not 5% $CO_2$; likewise for 40 g/L formaldehyde, not 10% formalin; and mass fraction, 8 ng/g, *etc.* Arabic numerals such as 23, 243, 641 should be read 23 243 641.

The format for how to accurately write common units and quantums can be found at: http://www.wjgnet.com/1949-8470/g_info_20100313185816.htm.

### *Abbreviations*

Standard abbreviations should be defined in the abstract and on first mention in the text. In general, terms should not be abbreviated unless they are used repeatedly and the abbreviation is helpful to the reader. Permissible abbreviations are listed in Units, Symbols and Abbreviations: A Guide for Biological and Medical Editors and Authors (Ed. Baron DN, 1988) published by The Royal Society of Medicine, London. Certain commonly used abbreviations, such as DNA, RNA, HIV, LD50, PCR, HBV, ECG, WBC, RBC, CT, ESR, CSF, IgG, ELISA, PBS, ATP, EDTA, mAb, can be used directly without further explanation.

***Italics***
Quantities: *t* time or temperature, *c* concentration, *A* area, *l* length, *m* mass, *V* volume.
Genotypes: *gyrA*, *arg* 1, *c myc*, *c fos*, *etc.*
Restriction enzymes: *Eco*RI, *Hin*dI, *Bam*HI, *Kbo* I, *Kpn* I, *etc.*
Biology: *H. pylori*, *E coli*, *etc.*

***Examples for paper writing***
**Editorial:** http://www.wjgnet.com/1949-8470/g_info_20100313182341.htm

**Frontier:** http://www.wjgnet.com/1949-8470/g_info_20100313182448.htm

**Topic highlight:** http://www.wjgnet.com/1949-8470/g_info_20100313182639.htm

**Observation:** http://www.wjgnet.com/1949-8470/g_info_20100313182834.htm

**Guidelines for basic research:** http://www.wjgnet.com/1949-8470/g_info_20100313183057.htm

**Guidelines for clinical practice:** http://www.wjgnet.com/1949-8470/g_info_20100313183238.htm

**Review:** http://www.wjgnet.com/1949-8470/g_info_20100313183433.htm

**Original articles:** http://www.wjgnet.com/1949-8470/g_info_20100313183720.htm

**Brief articles:** http://www.wjgnet.com/1949-8470/g_info_20100313184005.htm

**Case report:** http://www.wjgnet.com/1949-8470/g_info_20100313184149.htm

**Letters to the editor:** http://www.wjgnet.com/1949-8470/g_info_20100313184410.htm

**Book reviews:** http://www.wjgnet.com/1949-8470/g_info_20100313184803.htm

**Guidelines:** http://www.wjgnet.com/1949-8470/g_info_20100313185047.htm

## SUBMISSION OF THE REVISED MANUSCRIPTS AFTER ACCEPTED

Please revise your article according to the revision policies of *WJR*. The revised version including manuscript and high-resolution image figures (if any) should be re-submitted or uploaded online. The author should send copyright transfer letter, and responses to the reviewers and science news to us *via* email.

## Editorial Office

***World Journal of Radiology***
Editorial Department: Room 903, Building D,
Ocean International Center,
No. 62 Dongsihuan Zhonglu,
Chaoyang District, Beijing 100025, China
E-mail: wjr@wjgnet.com
http://www.wjgnet.com
Telephone: +86-10-85381892
Fax: +86-10-85381893

***Language evaluation***
The language of a manuscript will be graded before it is sent for revision. (1) Grade A: priority publishing; (2) Grade B: minor language polishing; (3) Grade C: a great deal of language polishing needed; and (4) Grade D: rejected. Revised articles should reach Grade A or B.

***Copyright assignment form***
Please download a Copyright assignment form from http://www.wjgnet.com/1949-8470/g_info_20100313185522.htm.

***Responses to reviewers***
Please revise your article according to the comments/suggestions provided by the reviewers. The format for responses to the reviewers' comments can be found at: http://www.wjgnet.com/1949-8470/g_info_20100313185358.htm.

***Proof of financial support***
For paper supported by a foundation, authors should provide a copy of the document and serial number of the foundation.

***Links to documents related to the manuscript***
*WJR* will be initiating a platform to promote dynamic interactions between the editors, peer reviewers, readers and authors. After a manuscript is published online, links to the PDF version of the submitted manuscript, the peer-reviewers' report and the revised manuscript will be put on-line. Readers can make comments on the peer reviewer's report, authors' responses to peer reviewers, and the revised manuscript. We hope that authors will benefit from this feedback and be able to revise the manuscript accordingly in a timely manner.

***Science news releases***
Authors of accepted manuscripts are suggested to write a science news item to promote their articles. The news will be released rapidly at EurekAlert/AAAS (http://www.eurekalert.org). The title for news items should be less than 90 characters; the summary should be less than 75 words; and main body less than 500 words. Science news items should be lawful, ethical, and strictly based on your original content with an attractive title and interesting pictures.

***Publication fee***
Authors of accepted articles must pay a publication fee.
EDITORIAL, TOPIC HIGHLIGHTS, BOOK REVIEWS and LETTERS TO THE EDITOR are published free of charge.